学位論文

Effect of Low-Metallicity on Molecular-Cloud Chemical Composition: the Case of Local Dwarf Galaxies

(近傍矮小銀河で探る星間分子雲の化学組成への低重元素量の影響)

平成 28 年 12 月博士（理学）申請

東京大学大学院理学系研究科

物理学専攻

西村 優里

Abstract

The Local Group of galaxies around our Galaxy involves more than 50 galaxies, most of which are low-metallicity dwarf ones. In such a low-metallicity galaxy, chemical compositions of molecular clouds are considered to be different from those in our Galaxy both quantitatively and qualitatively, due to a small amount of dust grains and stronger UV radiation field. To characterize the molecular-cloud scale chemical composition in low-metallicity galaxies, we have conducted spectral line surveys in the millimeter-wave region toward nearby dwarf galaxies, the Large Magellanic Cloud, IC10, and NGC6822, whose metallicity is $1/2 - 1/3$ of the Solar neighborhood. We have detected the rotational spectral lines of CCH, HCN, HCO^+, HNC, CS, and SO in addition to ^{12}CO and ^{13}CO (with exceptions of the HNC and SO lines in NGC6822 due to the insufficient sensitivity), while the CH_3OH lines have not been detected in any sources. The spectral intensity patterns of these dwarf galaxies are found to be essentially similar to one another regardless of different star-formation activities. Hence, the spectral pattern likely reflects characteristic chemical composition of molecular clouds in the low-metallicity dwarf galaxies without significant influence of star-formation activities.

We compare the chemical compositions of these dwarf galaxies with those of our Galaxy and the spiral galaxy M51, both of which have Solar-metallicity. We find the deficiency of the HCN/HCO^+ and HNC/HCO^+ ratios in the dwarf galaxies, which would reflect a lower elemental abundance ratio of N/O by a factor of $2 - 7$. Furthermore, we find a high CCH/HCO^+ ratio in the dwarf galaxies.

In the dwarf galaxies, the visual extinction for a given column density of H_2 molecules becomes lower owing to the lower abundance of dust grain. This effect extends photodissociation regions (PDRs) in cloud peripheries. Since CCH is efficiently produced in PDRs, the high CCH abundance recognized in these three galaxies likely reflects the low-metallicity condition. Moreover, non-detection of CH_3OH can also be explained in this picture. CH_3OH is produced on dust grains by hydrogenation of the adsorbed CO molecule. Extension of PDRs in cloud peripheries would raise the temperature there, which decreases CH_3OH formation due to a fall of sticking probability of the hydrogen atom. Hence, CH_3OH would be less abundant in the dwarf galaxies. Thus, we have established the characteristics of molecular-cloud-scale chemical composition in dwarf galaxies for the first time, and have interpreted

it in terms of the low-metallicity condition.

In addition to the study of dwarf galaxies, we have conducted a molecular-cloud-scale observation toward the Galactic star-forming molecular cloud, W3(OH), and have revealed that the spectral intensity pattern averaged over a molecular cloud mostly reflects less dense parts extended over the molecular cloud rather than dense cores and star-forming regions. We have also conducted chemical model calculations and constrained physical conditions responsible for such a molecular-cloud-scale chemical composition. This result indicates that local star-formation activities are smeared out in the molecular-cloud-scale chemical composition, and justifies that the chemical composition observed in the dwarf galaxies mainly reflects the nature of the galaxy itself or the galactic scale phenomena.

Above all, the chemical compositions under the low-metallicity condition has successfully characterized for the first time. The results obtained in this thesis will constitute a fundamental base not only for understanding physical and chemical conditions of dwarf galaxies, but also for applying chemical diagnostics to high-redshift galaxies.

Contents

Chapter 1

Introduction

1.1 The Low Metallicity Environments

1.1.1 Chemical Evolution of the Universe

In astrophysics, "chemical evolution" refers to two different concepts according to the context; (1) enrichment of heavy elements or metals (C, N, O, and heavier nuclei) by stellar nucleosynthesis and supernovae and (2) evolution of molecular composition in molecular clouds along star formation processes. In studies of galaxies or galactic scale phenomena, "chemical evolution" is usually used in terms of the first concept. The nucleosynthesis history is a very important issue in astrophysics. Namely, how stars and galaxies have been formed and how heavy elements have been synthesized during the history of the Universe, deeply affect to most of the astrophysical processes in galaxies and galactic scale phenomena.

On the other hand, it is now known that molecular clouds, birth place of stars, harbor rich organic molecules and at least a part of these molecules are delivered to a planetary system through star-formation process (Herbst & Van Dishoeck, 2009; Sakai & Yamamoto, 2013). In the early evolutionary stage of the Universe when heavy elements are still deficient, how should the molecular evolution, that is the second concept of "chemical evolution", be different from that in the metal-rich condition occurring in the Solar neighborhood? This is another very interesting and important problem in astrophysics, which is related to understandings of the origin of ourselves and its rarity value in the Universe. In addition, there is another important aspect for understanding molecular composition and its evolution in high-redshift galaxies. Molecular composition (hereafter referred to as chemical composition) can often provide us with novel information on peculiar physical conditions and evolutionary stages of galaxies, as revealed in the nearby galaxies. For instance, it is known that the AGN activities and starbursts significantly affects the chemical composition, and conversely, chemical

diagnostics helps us to find and understand these phenomena deeply embedded in molecular gas and dust in the central part of galaxies (Lepp & Dalgarno, 1996; Kohno et al., 2001; Meijerink et al., 2007). Extending this powerful diagnostic tool to high-redshift galaxies will significantly contribute to thorough understandings of the evolution of galaxies.

However, it is very hard to observe molecules in high-redshift galaxies in general. Since molecular signals from high-redshift galaxies are faint in any wavelength, observations of not only the brightest molecules (CO) but also various molecules to characterize the chemical composition are apparently challenging. Thanks to the recent advances in observation technologies in radio astronomy, such an observation is now becoming barely possible for some cases, but such efforts are still very limited in practice. An exception is radio absorption studies of distant galaxies against bright continuum emission of gravitationally lensed quasars (Wiklind & Combes, 1996; Muller et al., 2011; Wallström et al., 2016). However, a specific line-of-sight of the absorbing galaxy is seen, and hence, it is difficult to disentangle the galactic-scale effect (including the effect of metallicity) and local effects on chemical composition.

1.1.2 Dwarf Galaxies

Under the above circumstances, one of the practical approach to understand the characteristic chemical composition in the low-metallicity condition of high-redshift galaxies is to observe nearby dwarf galaxies. Dwarf galaxies have not generally experienced many star formation activities during their life due to relatively small mass, and hence, they are still in the metal-poor conditions (Mateo, 1998). Alternatively, dwarf galaxies may not be able to maintain the metal rich gas for a long time because of their small mass. Moreover, dwarf galaxies are the most popular type of galaxies in numbers among galaxies in the Universe. In the Local Group, many dwarf galaxies are known to exist (Mateo, 1998). Their total distribution is still unknown, and extremely faint ones are still newly being discovered (e.g., Homma et al., 2016). Because of these reasons, dwarf galaxies are subject to important targets for various areas of astronomy and astrophysics. In this thesis, we focus on the low-metallicity characteristics of dwarf galaxies as a proxy of high-redshift galaxies.

One of representative nearby dwarf galaxies is the large Magellanic cloud (LMC). Its metallicity is $1/2 - 1/3$ of the Solar-neighborhood value (Westerlund, 1997). Since the LMC is the nearest external galaxy from the Milky Way galaxy, observational and theoretical studies on star formation, stellar evolution, galactic scale dynamics, interaction with other galaxies, and many others have extensively been reported so far. Its relatively low inclination angle ($i = 35^\circ$ van der Marel & Cioni, 2001) makes it even more favorable target for various kinds of observations. Molecular line observations in the

radio wavelength have been conducted to explore the molecular gas distribution and its relation to star formation (e.g., Fukui & Kawamura, 2010). Although they have mostly been carried out in the rotational spectral lines of CO, observations of other molecules have also been reported for a few active star-forming regions (e.g., Chin et al., 1997; Heikkilä et al., 1999; Wang et al., 2009). In this sense, the LMC is the best target for a systematic study of chemical compositions in the low metallicity condition. The small Magellanic cloud (SMC) is also an important target, whose metallicity is lower than that of the LMC (Westerlund, 1997). Although the distance to the SMC is similar to that to the LMC, its molecular line emission in the radio wavelength is generally faint except for the CO line emission because of its lower metallicity nature (Heikkilä et al., 1999).

In addition to the LMC and the SMC, there are many dwarf galaxies in the Local Group. Most of them are in the low-metallicity condition, whose metallicity is lower than that of the Solar neighborhood by a factor of $2 - 10$ (Mateo, 1998). Some examples are IC10, NGC6822, NGC55, and NGC185, all of which harbor rich gas content. They are more distant than the LMC, but observations of various molecular lines in the radio wavelength seem possible thanks to the recent advances in radio astronomy.

By use of these nearby dwarf galaxies, the chemical composition characteristic to the low-metallicity condition can be explored, which will be an important base to step forward to chemical diagnostics of high-redshift galaxies in the near future. This is the basic motivation of this thesis.

1.2 Astrochemistry

1.2.1 Star Formation in Molecular Clouds

Now, 180 or more kinds of molecules are known as interstellar molecules, which include simple diatomic molecules (CO, CS, etc.), fundamental molecules familiar to us (HCN, H_2CO, CH_3OH, etc.), molecular ions (HCO^+, N_2H^+, etc.), free radicals (CN, CCH, etc.) and complex organic molecules (CH_3CHO, $HCOOCH_3$, C_2H_5CN, etc.). Existence of molecular ions clearly indicates that interstellar molecular clouds are weakly ionized plasma, which is driven by cosmic-ray ionization and photoionization by the interstellar UV radiation. On the other hand, existence of complex organic molecules suggests that molecular evolution is occurring at low temperature (~ 10 K) in the low H_2 density condition ($\sim 10^4$ cm^{-3}) even before star and planet formation (Caselli & Ceccarelli, 2012).

The relative abundances of these molecules (chemical composition) are different from source to source, depending on its physical condition and the evolutionary stage. For instance, chemical composition is known to systematically change in the course of star formation (e.g., Suzuki et al., 1992;

Sakai & Yamamoto, 2013). Unsaturated organic molecules (carbon-chain molecules) appear in the early stages of gravitational contraction of a parent molecular cloud. In the later stage, these unsaturated organic molecules tend to be deficient because of adsorption onto dust grains and/or destruction through gas-phase reactions. On the other hand, nitrogen-bearing molecules such as NH_3 and N_2H^+ gradually become abundant in the late stage of the prestellar core phase. Deuterated species such as N_2D^+, DCN, and DNC also become abundant in the late stage (Hirota et al., 2001; Caselli et al., 2002; Parise et al., 2004). This is enhanced by depletion of CO onto dust grains in the late stage (Caselli et al., 1999, 2003), because CO is the main destructor of H_2D^+, a precursor of various deuterated species. After onset of star formation, i.e., the birth of a protostar, saturated organic molecules (CH_3OH, CH_3CHO, $HCOOCH_3$, C_2H_5CN) formed on dust grains appear in the gas phase (e.g., Cazaux et al., 2003). Hence, chemical composition systematically changes along the formation process of a protostar. This chemical effect can be used as a powerful tool for investigating evolutionary stage of a molecular cloud core before onset of star formation.

Chemical composition also depends on the physical situation. For instance, it is known that the SiO molecule can be used as a good indicator of shocks (Bachiller et al., 1990; Mikami et al., 1992; Bachiller & Pérez Gutiérrez, 1997). Silicon is usually heavily depleted, and Si containing molecules are very deficient in molecular clouds under usual conditions. However, strong shock can evaporate or sputter the SiO molecule from silicate grains, and the rotational emission of SiO can be observed in the shocked region. A famous example is the shocked molecular gas caused by an impact of molecular outflow from a protostar (Mikami et al., 1992). In addition to SiO, some other grain species such as CH_3OH and H_2CO can also be used as a shock tracer (Bachiller & Pérez Gutiérrez, 1997). Thus, the chemical composition can highlight a particular physical conditions in molecular clouds.

As described above, chemical diagnostics is recognized as a very useful method in studies of star and planet formation in molecular clouds. This trend will be more and more important in the near future, because ALMA (Atacama Large Millimeter/submillimeter Array; `http://alma.mtk.nao.ac.jp/`) will provide us with the distributions of various molecular species at an unprecedented angular resolution. Making a full use of the knowledges and the concepts obtained in the astrochemistry studies of Galactic sources for studies of external galaxies is also awaited.

1.2.2 Extragalactic Astrochemistry

Astrochemical studies of external galaxies have been conducted since 1980s, and about 1/3 kinds of interstellar molecules are detected. However, the targets are restricted to the nearby bright galaxies such as NGC253, M82, and NGC1068, and particularly to their nucleus region. This is because

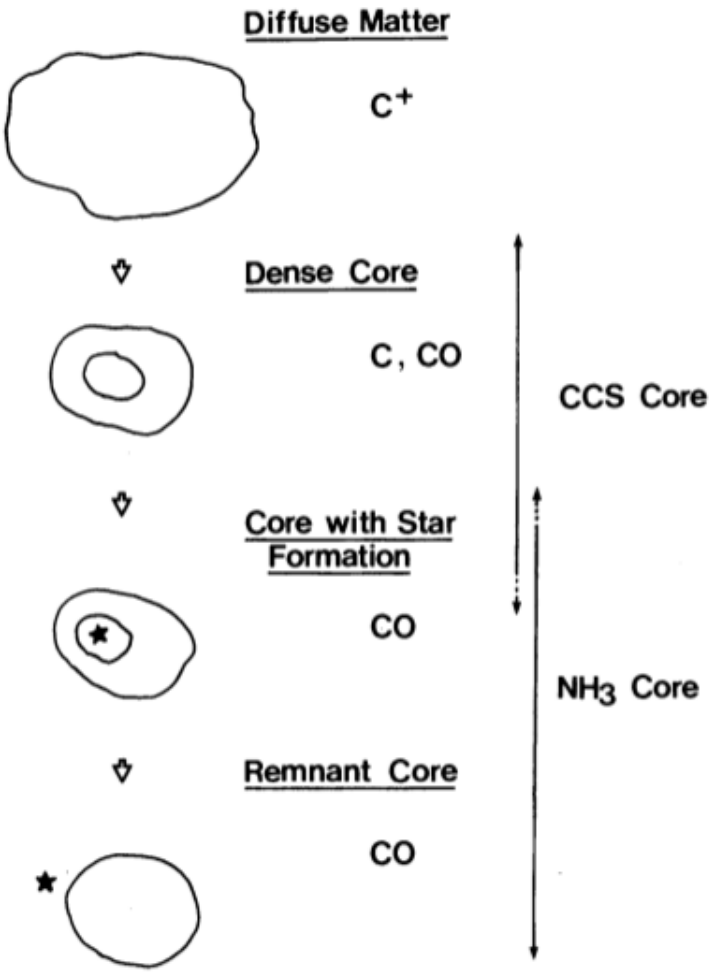

Figure 1.1 Schematic illustration of the chemical evolution of a contracting cloud taken from Suzuki et al. (1992). The major form of carbon changes from C^+ to C, and then from C to CO, as the cloud evolves.

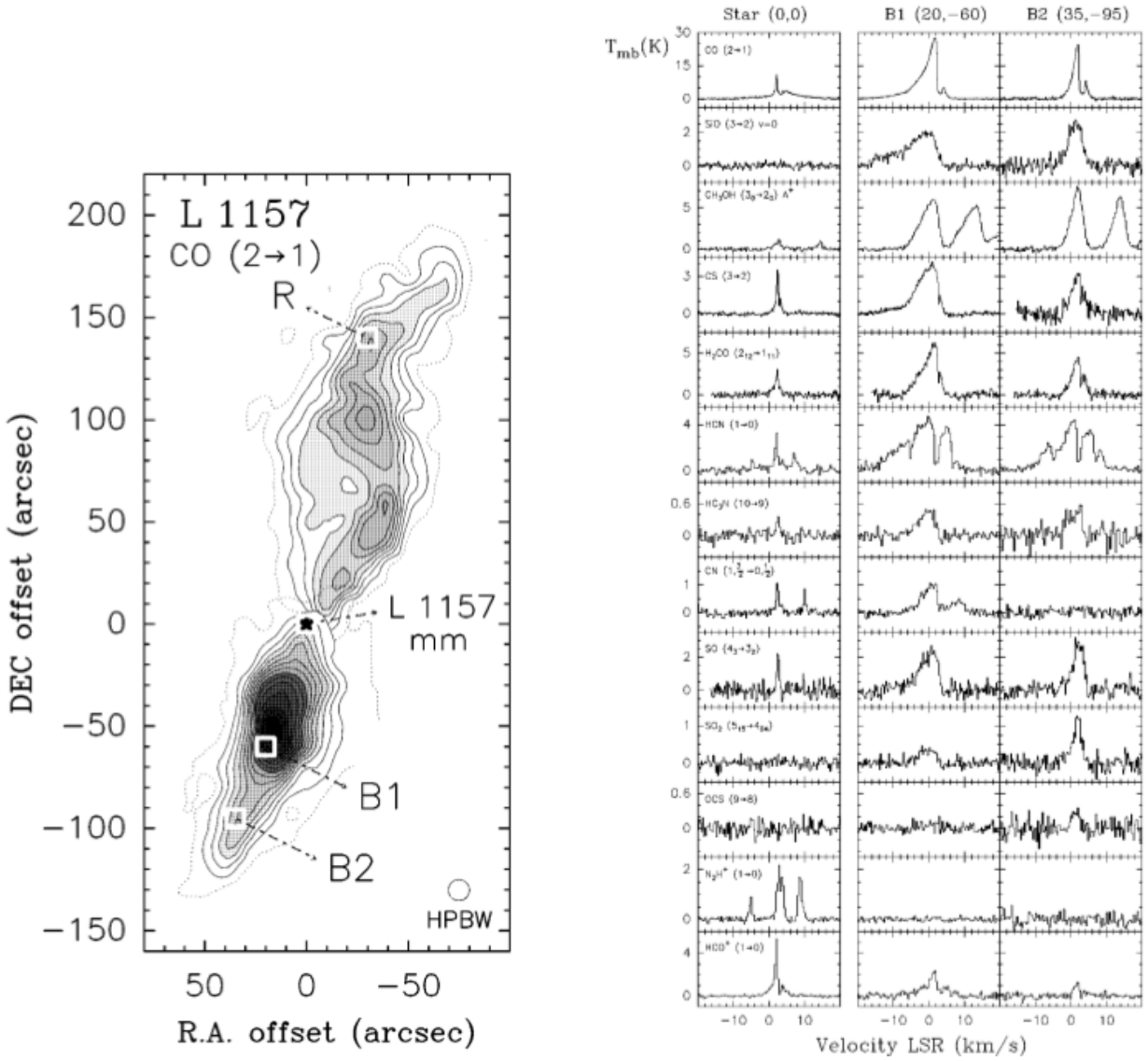

Figure 1.2 CO $J = 2 - 1$ emission map of L1157 (*left*) and molecular line profiles observed toward three positions Star, B1, and B2 in L1157 (*right*) taken from Bachiller & Pérez Gutiérrez (1997).

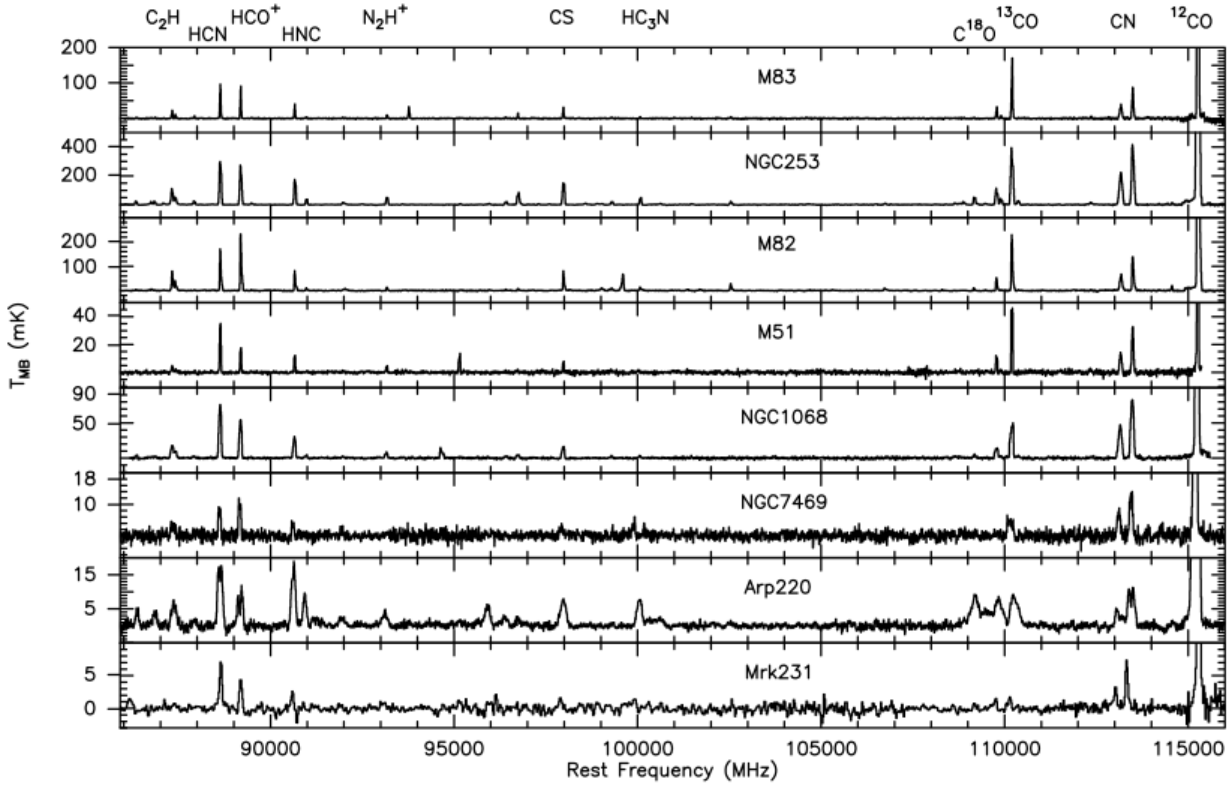

Figure 1.3 Spectra between 86 and 116 GHz observed toward starburst galaxies M83, NGC253, and M82, the galaxies hosting an AGN M51, NGC1068, and NGC7469, the ultra-luminous infrared galaxies Arp220 and Mrk231, taken from Aladro et al. (2015) Figure 1.

emission of various molecules is readily detected there (e.g., Martín et al., 2006; Aladro et al., 2011, 2013). For these sources, the spectral line survey observations have been conducted to characterize their chemical composition (Aladro et al., 2015, Figure 1.3). On the other hand, a survey of some fundamental molecular species such as HCN and HCO^+ has extensively been carried out for many external galaxies in order to quantify the amount of dense molecular gas directly related to current star formation activities. In these observations, the HCN/HCO^+ ratio is found to be systematically enhanced in the galaxies harboring the active galactic nucleus (AGN) (e.g., Lepp & Dalgarno, 1996; Kohno et al., 2001; Meijerink et al., 2007; Aladro et al., 2015). The effects of the X-ray from the AGN (X-ray dissociation region: XDR), high temperature chemistry caused by shocks, and cosmic-ray ionization have been considered as the origin of the high ratio. This is a representative example of the chemical diagnostics of external galaxies, and can be applied to the nuclei of high-redshift galaxies deeply embedded in dense molecular gas and dust for identification of their AGN activities. Such a direction will be more and more popular in the ALMA era.

1.2.3 Background of the Thesis

Compared to nearby active galaxies, chemical compositions of low-metallicity dwarf galaxies have been remained to be poorly understood, mainly because of faint molecular emission. However, the situation is recently changing. Rapid developments of receiver sensitivities and wideband backends have allowed us to study chemical compositions of dwarf galaxies with a reasonable observation time. Chemical compositions under the low-metallicity condition will be different from those in the normal metallicity condition both quantitatively and qualitatively. In the quantitative sense, the low-metallicity condition leads to the low fractional abundances of molecules relative to H_2. In particular, the abundances of particular elements (and isotopes) are much less abundant than the other elements, which will directly impact molecular abundances containing the particular elements. More importantly, the qualitative change is expected due to the low-metallicity condition through change in physical conditions. For instance, the lower abundance of dust grains will enhance the effect of photodissociation in peripheries of molecular clouds, which will cause substantial changes in chemical compositions. Understandings of such characteristic chemical compositions and their origins in dwarf galaxies will be an important base for exploring high-redshift galaxies.

1.3 Outline of the Thesis

In this thesis, the chemical composition of dwarf galaxies are studied by radio astronomical observations. It is organized as follows: In Section 2, the general description of radio telescopes and observation techniques are briefly summarized. In Section 3, we describe our study of the chemical composition of several nearby dwarf galaxies. Characteristic chemical composition of the low-metallicity dwarf galaxies are revealed by the spectral line survey of the Large Magellanic Cloud, IC10, and NGC6822. Through this study, we have also found that the spectral intensity pattern averaged over the molecular-cloud ($\sim$ 10 pc) scale is not affected by local star-formation activities. To examine the meaning of the molecular-cloud-scale chemical composition, we have conducted the large-scale mapping line survey observation toward the Galactic molecular cloud W3(OH), as described in Section 4. We have confirmed that the averaged spectrum reflects the chemical composition of the extended part of the molecular cloud rather than star-forming dense cores. In Section 5, we have investigated physical conditions which are responsible for the molecular-cloud-scale chemical compositions with the aid of chemical model calculations. Finally, Section 6 conclude this thesis with some future prospects.

Chapter 2

Observation Techniques of Radio Telescopes

2.1 Radio Telescopes

2.1.1 Antenna

In radio astronomy, a parabolic antenna is generally employed to collect faint radiation from a target source. A Cassegrain antenna which consists of a concave main parabolic reflector dish and a smaller convex secondary hyperbolic reflector suspended in front of the primary focus is usually used. In addition, a Gregorian antenna which employs a concave ellipsoidal reflector as the secondary reflector and a Nasmyth-Cassegrain antenna which is added a comparatively small tertiary flat mirror to the Cassegrain antenna are also used.

Radio telescopes are classified into two categories; a single-dish telescope and an interferometer consisting of a number of antennas. In the case of the single-dish observation, the angular resolution

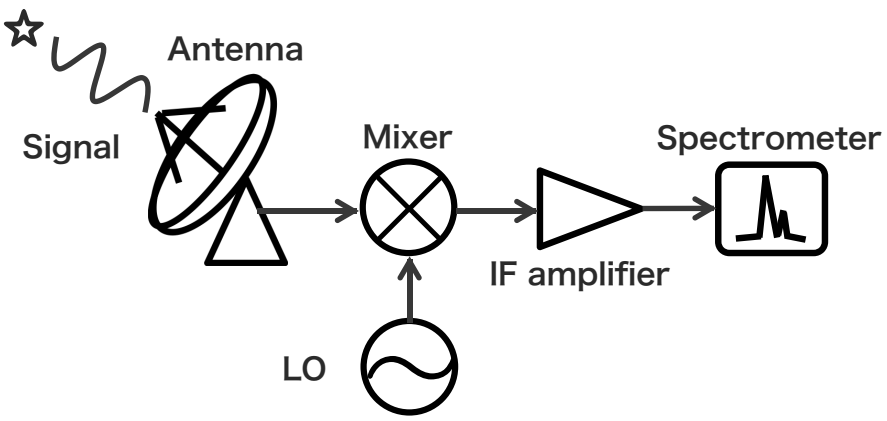

Figure 2.1 The block diagram of the observing system in radio astronomy.

θ is related to the diameter of main reflector D by the following equation:

$$\theta = \frac{\kappa\lambda}{D}. \tag{2.1}$$

Here, λ is a observation wavelength and κ is a constant depending on the illumination pattern on the main reflector. When the all surface of the main reflector is equally weighted, κ is 1.02, which provides the highest angular resolution. To eliminate the side lobes caused by the diffraction at the edge of the main reflector, κ is usually taken to be $1.2 - 1.5$ by less weighting the edge. In the case of the interferometric observation, resolution is also given by equation 2.1 approximately, where D is taken as the maximum projected baseline length.

For efficient focusing, the surface of accuracy of the main reflector is needed to be better than 1/20 of the observation wavelength. The gravitational deformation is sometimes a problem for a large aperture antenna. A homologous deformation technique is often used to realize a good surface accuracy for the whole elevation angle.

2.1.2 Front-end

Heterodyne Mixer

Electro-magnetic signals from a target source in space are generally faint so that the amplification is necessary to analyze them. At the wavelengths shorter than 3 mm (i.e., the frequency higher than 90 GHz), a low-noise amplifier is not readily available. Hence, heterodyne receivers are usually employed in millimeter- and submillimeter-wave observations.

For the heterodyne process, a non-linear mixer device, whose relation between the current I and the voltage V, is characterized as:

$$I = a_0 + a_1 V + a_2 V^2 + a_3 V^3 + \cdots, \tag{2.2}$$

is used. By the second-order term, the input millimeter-wave signal is down-converted to the lower frequency signal. Here, a signal from the antenna $V_s(t)$ is written as:

$$V_s(t) = V_{s0}\cos(\omega_s t + \phi_s), \tag{2.3}$$

while a signal from a local oscillator $V_l(t)$ is written as:

$$V_l(t) = V_{l0}\cos(\omega_l t + \phi_l). \tag{2.4}$$

Applying these two signals into the mixer, the mixer current is written as:

$$I = a_1(V_s(t) + V_l(t)) + a_2(V_s(t) + V_l(t))^2 + a_3(V_s(t) + V_l(t))^3 + \cdots. \tag{2.5}$$

The second term of this equation can be calculated as:

$$\begin{aligned}(V_s(t)+V_l(t))^2 &= \frac{1}{2}({V_{s0}}^2+{V_{l0}}^2)+\frac{1}{2}\cos 2(\omega_s t+\phi_s)+\frac{1}{2}\cos 2(\omega_l t+\phi_l)\\ &\quad +V_{s0}V_{l0}\cos[(\omega_s+\omega_l)t+(\phi_s+\phi_l)]\\ &\quad +V_{s0}V_{l0}\cos[(\omega_s-\omega_l)t+(\phi_s-\phi_l)]. \end{aligned} \tag{2.6}$$

The first term represents a direct-current component, and the second and third terms represent the second harmonics of the signals from the antenna and local oscillator, respectively. The forth and fifth terms are the sum and difference frequencies of the two input signals. By using an appropriate frequency filter, the difference frequency component can be extracted as the intermediate frequency (IF) signal. The IF frequency is usually taken around $4-12$ GHz.

As heterodyne mixers, superconducting devices are often employed in the radio telescopes because of its low noise and high conversion efficiency. An SIS (Superconductor-Insulator-Superconductor) mixer is one of the most frequently used mixers in the millimeter-wave region. It has a "sandwich" structure of two superconductors (Nb) separated by a very thin insulator layer (SiO_x), which is a kind of a Josephson junction. It is used as a mixer by using the non-linearity of tunneling current between the two superconductors. For the frequency higher than 1 THz, a superconducting HEB (Hot Electron Bolometer) mixer is also employed.

Intermediate-Frequency Amplifier

The intermediate frequency (IF) from the mixer is amplified before it is analyzed by a radio spectrometer. In the heterodyne system, The noise temperature expressed in terms of input $T_{\rm RX}$ is written as:

$$T_{\rm RX} = T_{\rm MIX} + T_{\rm IF}/G, \tag{2.7}$$

where $T_{\rm MIX}$ and $T_{\rm IF}$ represent noise temperatures of the mixer and the first-stage IF amplifier, respectively. G is a gain of heterodyne process and is generally lower than 1. Therefore, the noise level highly depends on the noise of the first amplifier. For the first amplification, HEMT (High Electron Mobility Transistor) cooled under 20 K is generally employed. Recently, the SIS mixer receiver achieves the noise temperature close to the quantum limit ($h\nu/k_B$).

2.1.3 Back-end System

The output of the front-end system is further amplified and frequency-convented for the spectral analysis by radio spectrometers. There are two important features for the radio spectrometers: high

frequency resolution and wide instantaneous bandwidth. Representative radio spectrometers are acoust-optical spectrometers (AOS) and digital autocorrelators. In the latter type, the bandwidth is determined by the sampling speed, while the frequency resolution is by the maximum delay time of autocorrelation. Thanks to the recent advantage in digital technologies, a large set of autocorrelators is now available a standard back-end, which realizes the high resolution and the wide instantaneous bandwidth at the same time. This feature is very useful for the spectral line survey observations in the present study.

2.2 Observation Techniques

In this section, observation models and calibration methods employed in this thesis are described. The calibration in the single-dish observation includes intensity calibration and pointing calibration. The former is described in Section 2.2.2. On the other hand, the pointing calibration is different from telescope to telescope, and hence, it is described in the observation section (Section 3.3 and 4.3).

2.2.1 Observation Modes

In radio astronomical observations with a single-dish telescope, "a switching technique' is usually employed to eliminate atmospheric effects as well as temporal variations of gain and frequency dependence of the receiver system. The position switching mode, the frequency switching mode, and the wobbler switching mode are generally used for a single-point observation. In addition, the on-the-fly mapping mode is used for mapping observations with a single-dish telescope. In this study, we used the position switching mode, the on-the-fly mapping mode, and the wobbler switching mode in the observations, depending on the purposes. Here, we briefly describe these three observation modes.

Position Switching Mode

In the position switching mode, the telescope is pointed alternatively toward the two celestial positions, the OFF position and the ON position, which are the emission free position and the target source position, respectively. The integration time of the OFF position and the ON position is generally taken to be the same. The OFF position is selected to be as spatially close to the ON position as possible to minimize the atmosphere variations. The spectrum is obtained by subtracting the spectrum of the OFF position from that of the ON position. The rms noise temperature[1] ΔT [K] is given as:

$$\Delta T = \frac{\sqrt{2}T_{\rm sys}}{\sqrt{Bt}}, \tag{2.8}$$

[1]In radioastronomy, the temperature scale is used for the intensity, by using the Rayleigh-Jeans law: $I(\nu, T) = \frac{2\nu^2}{c^2}kT$.

where $T_{\rm sys}$ [K], B [Hz], and t [sec] stand for the system noise temperature, the frequency resolution, and the integration time for the ON position, respectively.

On-The-Fly Mapping Mode

The on-the-fly mapping mode is similar to the position switching mode, but the antenna is scanned continuously across the source instead of pointing toward a single ON position. The digital back-ends are also running continuously during the antenna scan, and the data are dumped at a high rate (at least Nyquist frequency of scanning speed/beam size) to prevent beam smearing. Then, the data are resampled at celestial positions, and the intensity map is prepared. By using the on-the-fly mapping mode, the intensity map is obtained in a shorter observation time than the point-to-point observation with the position switching mode, because the overhead time for the antenna to move between the ON and OFF positions can be saved. The rms noise temperature ΔT [K] is given as:

$$\Delta T = \frac{T_{\rm sys}}{\eta_{\rm q}\sqrt{B}}\sqrt{\frac{1}{t_{\rm ON}} + \frac{1}{t_{\rm OFF}}}, \tag{2.9}$$

where $\eta_{\rm q}$, $T_{\rm sys}$ [K], B [Hz], $t_{\rm ON}$ [sec] and $t_{\rm OFF}$ [sec] are quantization efficiency of the digital back-end spectrometer, the system noise temperature, the frequency resolution, the integration times for the ON and OFF positions, respectively.

Wobbler Switching Mode

In the wobbler switching mode, the OFF and ON positions are switched by wobbling the secondary reflector at a rate of $0.1 - 1$ Hz. The observing efficiency is higher than that of the position switching mode, as the overhead time for moving the main reflector between the OFF and ON positions is not necessary. Furthermore, flat baselines are obtained for the most cases, because the wobbling frequency is high enough to eliminate the atmosphere variations. However, the throw angle of the wobbler is almost limited to a small angle, and hence, this mode is not suitable for spatially extended sources. The rms noise temperature is given by the same equation as equation (2.8).

2.2.2 Intensity Calibration

To calibrate the intensity scale of the observed signal without the effecta of gain variations of the telescope system and the atmospheric attenuation, the chopper-wheel method is usually used in the single-dish observation. When the telescope is pointed toward the ON position, the received power $V_{\rm ON}$ is written as:

$$V_{\rm ON} = \alpha[T_{\rm A}^{*}e^{-\tau} + T_{\rm atm}(1 - e^{-\tau}) + T_{\rm RX}], \tag{2.10}$$

where $T_{\rm A}^*$ represents the antenna temperature corrected for the atmospheric attenuation, τ the opacity of atmosphere, $T_{\rm atm}$ the temperature of atmosphere, $T_{\rm RX}$ the receiver noise temperature, and α the proportional constant specific to the telescope system. On the other hand, when the telescope is pointed toward the OFF position, the received power $V_{\rm OFF}$ is written as:

$$V_{\rm OFF} = \alpha[T_{\rm atm}(1 - e^{-\tau}) + T_{\rm RX}]. \tag{2.11}$$

To calibrate the absolute power, an absorber at the temperature of $T_{\rm abs}$ is inserted into the optical path in front of the receiver. Then, the received power $V_{\rm abs}$ is given as:

$$V_{\rm abs} = \alpha[T_{\rm abs} + T_{\rm RX}]. \tag{2.12}$$

Assuming that the temperatures of the atmosphere and the absorber are the same ($T_{\rm atm} = T_{\rm abs}$), we obtain the following relations:

$$V_{\rm ON} - V_{\rm OFF} = \alpha T_{\rm A}^* e^{-\tau} \tag{2.13}$$

$$V_{\rm abs} - V_{\rm OFF} = \alpha T_{\rm atm} e^{-\tau} \tag{2.14}$$

Then, the antenna temperature is obtained as:

$$T_{\rm A}^* = \frac{V_{\rm ON} - V_{\rm OFF}}{V_{\rm abs} - V_{\rm OFF}} \times T_{\rm abs}, \tag{2.15}$$

while the system noise temperature $T_{\rm sys}$ is derived as:

$$T_{\rm sys} = \frac{V_{\rm OFF}}{V_{\rm abs} - V_{\rm OFF}} \times T_{\rm abs}. \tag{2.16}$$

A typical accuracy of the intensity calibrated by the chopper-wheel method is about 20%. This is because, strictly speaking, the absorber temperature can be different from the atmospheric temperature. More accurate calibration is generally conducted by using two absorbers at different temperature: One is cooled by the liquid nitrogen, and the other is at the room temperature.

The antenna temperature $T_{\rm A}^*$ is not corrected by the main-beam efficiency $\eta_{\rm B}$ of the antenna. The main-beam temperature $T_{\rm MB}$ is obtained as:

$$T_{\rm MB} = \frac{T_{\rm A}^*}{\eta_{\rm B}}. \tag{2.17}$$

The main-beam efficiency is usually provided by the observatory through observations of the planets.

2.3 Telescopes Used for This Study

2.3.1 The Mopra 22 m Telescope

The Mopra 22 m telescope is a single-dish radio telescope located at the edge of the Warrumbungle Mountains near Coonabarabran, about 450 km north-west of Sydney. It is operated by Commonwealth

Scientific and Industrial Research Organization (CSIRO), Astronomy and Space Science division. The telescope is at a latitude and a longitude of (-31° $16'$ $4.1''$ S, 149° $5'$ $58.9''$ E) and an elevation of 860 m.

The Mopra telescope has a main reflector with a diameter of 22 m, which is the largest single dish in the southern hemisphere. It is equipped with three receivers for the 3 mm, 7 mm, and 12 mm bands. The receivers use Indium Phosphide High Electron Mobility Transistor (InP HEMT) Monolithic Microwave Integrated Circuits (MMICs) as front-end amplifiers. We employed the 3 mm band receiver for this study. A digital spectrometer MOPS (Mopra Spectrometer) is installed as the back-end. MOPS offers two configurations: Wideband Mode and Zoom Mode. In this study, we employed Wideband mode which simultaneously covers 8.3 GHz by using 4 sub-bands. Each sub-band is 2.2 GHz wide and 2 polarizations, each having 8096 spectral channels.

2.3.2 The Nobeyama 45 m Telescope

The Nobeyama 45 m telescope is located at Nobeyama in Nagano, Japan. It is operated by Nobeyama Radio Observatory (NRO), which is a branch of the National Astronomical Observatory of Japan. The telescope is at a latitude and a longitude of (35° $56'$ $40.9''$ N, 138° $28'$ $21.2''$ E) and an elevation of 1350 m. The main reflector has a diameter of 45 m, and employs the homologous deformation concept to realize a good surface accuracy for the whole elevation angle against gravitational deformation. This is one of the largest millimeter-wave telescopes in the world.

This telescope covers the frequency range from 20 GHz to 116 GHz with several receivers. In this study, we employed the two-side-band SIS receiver TZ for the $85-116$ GHz band and the HEMT receiver H40 for $42-43$ GHz band. The TZ receiver can observe two orthogonal polarization signals simultaneously. As a back-end, the digital correlator SAM45 (Spectral Analysis Machine for the 45 m telescope) is employed for spectroscopic observations. SAM45 can process up to 16 IFs simultaneously with 4096 spectral channels for each IF. The channel separation of $3.81-488.28$ kHz is available.

2.3.3 The IRAM 30 m Telescope

The IRAM 30 m telescope is located at the Pico Veleta near Granada, Spain. It is one of the two radio astronomy facilities operated by Institut de Radioastronomie Millimétruque (IRAM), which is founded by the French Centre National de la Recherche Scientifique, the German Max-Planck-Gesellschaft and the Spanish Instituto Geográfico Nacional. The telescope is at a latitude and a longitude of (3° $23'$ $55.51''$ W, 37° $4'$ $6.29''$ N) and an elevation of 2850 m.

The telescope is equipped with a series of heterodyne receivers and continuum cameras operating

Figure 2.2 (*left*) The Mopra 22 m telescope (Mopra Telescope online, accessed December 2016), (*middle*) The Nobeyama 45 m telescope (NRO NAOJ online, accessed December 2016), (*right*) The IRAM 30 m telescope (IRAM online, accessed December 2016).

at the 3, 2, 1, and 0.9 mm bands (80-350 GHz). We used the heterodyne receiver EMIR (Eight MIxer Receiver) at the 3 and 2 mm band in this study. EMIR can observe dual-polarization (Horizontal and Vertical) signal in each band. Several back-ends are available for spectroscopic observations and continuum observations. In this study, we employed Fast Fourier Transform Spectrometer (FTS) with EMIR wide mode, which covers 8×4 GHz bandwidth with 195 kHz resolution.

Chapter 3

Chemical Composition of Low-Metallicity Dwarf Galaxies

3.1 Basic Strategies of Observations

As mentioned in Chapter 1, chemical compositions of dwarf galaxies are of particular interest for their low metallicity. In order to extract intrinsic chemical nature of dwarf galaxies, source selections and frequency settings for observations are essential. Here, the basic strategies of observations are described.

The Large Magellanic Cloud (LMC) is the nearest dwarf galaxy, and is an obvious target. Although molecular line observations have been reported (e.g., Chin et al., 1997; Heikkilä et al., 1999; Wang et al., 2009; Paron et al., 2014), they are mostly toward very active star forming regions. Hence, it seems very difficult to disentangle the intrinsic chemical nature of the dwarf galaxy and the possible effect of star-formation activities only from these observations. Sensitive observations toward less active star-forming regions or even starless regions are required for our purpose. Because of this reason, molecular clouds with different star-formation activities are chosen in the LMC. From these observations, we can learn how the observed chemical composition is affected by local star-formation activities, and can extract the intrinsic chemical composition specific to the low-metallicity condition.

Dwarf galaxies other than the LMC have to be observed to establish the general chemical composition of the low-metallicity dwarf galaxies. Figure 3.1 shows the CO intensity as a function of the metallicity. In the Local Group, there are handful galaxies where the CO emission is detected. Among them, the CO bright galaxies, which are expected to harbor a large amount of gas, are promising target for chemical diagnostics. This is practically important, because we need to observe faint lines of less abundant molecules in chemical diagnostics. In this view, IC10 and NGC6822 are good targets. We

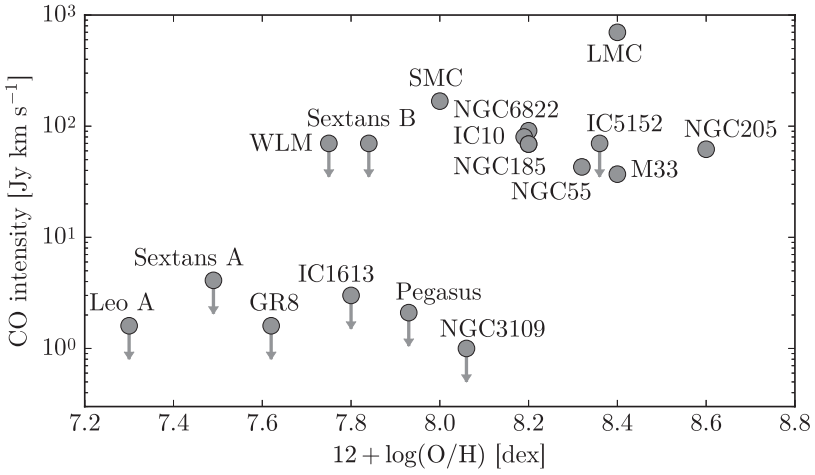

Figure 3.1 The CO integrated intensities of Local Group galaxies as a function of their oxygen abundance. The data are taken from the literature as: Onodera et al. (2012) for M33, Wang et al. (2009) for the LMC, Israel et al. (2003c) for the SMC, and Mateo (1998) for others. Note that, after Mateo (1998), the CO line has been detected for WLM by Elmegreen et al. (2013), tentatively for Sextans A by Shi et al. (2015), and for NGC3109 and IC5152 (Nishimura et al. unpublished).

also choose NGC55 and NGC185 for the second choice, both of which show the bright CO emission comparable to IC10 and NGC6822. However, we could not detect molecular lines except for CO for NGC55 and NGC185, as described later. Hence, we compare the chemical compositions of the three galaxies, the LMC, IC10, and NGC6822, in this study.

As for the frequency setting, the 3 mm band is chosen for the following reasons. First, there exist the fundamental rotational lines ($J = 1 - 0$) of several fundamental molecules such as HCO^+, HCN, HNC, CCH, N_2H^+, CN, and CO in this band. Some other important molecular lines of CS ($J = 2 - 1$) and CH_3OH ($J_K = 2_K - 1_K$) also fall in this band. These molecules are all important for characterizing the chemical composition. Second, these molecular lines can be excited subthermally even in the moderate H_2 density of $10^3 - 10^5$ cm^{-3} and the low gas kinetic temperature (10 K). Hence, these lines can trace a vast of molecular clouds of the target sources, which allow us to characterize the chemical nature averaged over the molecular-cloud scale. Third, sensitive large-aperture radio telescopes are available in this band. The Nobeyama 45 m telescope and IRAM 30 m telescope exist in the northern hemisphere, while the Mopra 22 m telescope is available in the southern hemisphere. In the 3 mm band, the linear resolution of these telescopes is about $10 - 100$ pc at the distance of the above target galaxies. Hence, we can resolve the scale of giant molecular clouds or their associations with these telescopes, and can reasonably define the physical character of the target source.

Table 3.1. Taget galaxies.

Galaxy	Distance[a] (Mpc)	$Z/Z_\odot$	$12+\log(\mathrm{O/H})$[a] (dex)	Observed position
LMC	0.05	$1/3-1/2$	8.4	(7 positions; see Table 3.3)
IC10	0.95	$1/5-1/3$	8.2	$\alpha_{\mathrm{J2000}}=00^h20^m27.9^s$, $\delta_{\mathrm{J2000}}=59^\circ17'01.0''$
NGC6822	0.49	$1/5-1/3$	8.1	$\alpha_{\mathrm{J2000}}=19^h44^m52.9^s$, $\delta_{\mathrm{J2000}}=-14^\circ43'12.7''$
NGC55	2.2	$1/5-1/3$	8.1	(4 positions; see Table 3.4)
NGC185	0.62	$1/5-1/3$	8.2	$\alpha_{\mathrm{J2000}}=00^h38^m56.6^s$, $\delta_{\mathrm{J2000}}=48^\circ20'19.0''$

Note. — Units of right ascension are hours, minutes, and seconds, and units of declination are degrees, arcminutes, and arcseconds.

[a]Mateo (1998).

In the single dish observations, we look at the chemical composition averaged over the molecular-cloud scale. Hence, the effect of individual star-forming regions is expected to be smeared out in the averaged chemical composition. This is particularly true in the 3 mm band observation, because molecular line emission in this band would be dominated by the extended molecular gas. Note that this is in contrast to molecular line emission in the submillimeter wave band which preferentially traces hot and dense parts of star-forming regions. In the 3 mm observation, we can investigate the intrinsic chemical nature specific to the low-metallicity condition without suffering from the star formation effects, as described in Chapter 4. Importance of such a molecular-cloud-scale chemical composition is now being recognized in studies of external galaxies (Watanabe et al., 2014).

The target sources are summarized in Table 3.1. All of them have $1/5-1/2$ Solar metallicity. The rest frequencies of the important molecular lines observed in this study are also tabulated in Table 3.2. In the following subsections, basic properties and previous studies of the target sources are described in detail.

3.2 Target Galaxies

3.2.1 The Large Magellanic Cloud

The Large Magellanic Cloud (LMC) is a well-known galaxy, which is one of the nearest galaxies located at $d=49.97\pm1.11$ kpc (Pietrzyński et al., 2013). Morphologically, the LMC has been categorized as an irregular galaxy (Irr) by the Hubble sequence type, but now, it is often recognized as a barred spiral galaxy (SBm). The metallicity in the LMC is known to be lower than in the Solar neighborhood by a factor 2 or more (Westerlund, 1997). The oxygen abundance $12+\log(\mathrm{O/H})$ in the LMC is about 8.4,

Table 3.2. The rest frequencies of the important molecular lines in our study.

Species	Transition	Frequency [GHz]
c-C_3H_2	$2_{12} - 1_{01}$	85.338893
CCH	$N = 1 - 0$, $J = 5/2 - 3/2$, $F = 1 - 1$	87.284105
CCH	$N = 1 - 0$, $J = 5/2 - 3/2$, $F = 2 - 1$	87.316898
CCH	$N = 1 - 0$, $J = 5/2 - 3/2$, $F = 1 - 0$	87.328585
CCH	$N = 1 - 0$, $J = 3/2 - 3/2$, $F = 1 - 1$	87.401989
CCH	$N = 1 - 0$, $J = 3/2 - 3/2$, $F = 0 - 1$	87.407165
CCH	$N = 1 - 0$, $J = 3/2 - 3/2$, $F = 1 - 0$	87.446470
HCN	$1 - 0$	88.631602
HCO^+	$1 - 0$	89.188396
HNC	$1 - 0$	90.663568
N_2H^+	$1 - 0$	93.173700
CH_3OH	$2_0 - 1_0$, A^+	96.741371
CS	$2 - 1$	97.980953
SO	$N_J = 2_3 - 1_2$	99.299870
$C^{18}O$	$1 - 0$	109.782173
^{13}CO	$1 - 0$	110.201354
CN	$N = 1 - 0$, $J = 3/2 - 1/2$	113.490970
^{12}CO	$1 - 0$	115.271202

which is lower than the Solar-metallicity by a factor of $2-3$ (Dufour et al., 1982). In particular, Dufour et al. (1982) reported that the C/H and N/H ratios are lower than those in the Solar neighborhood by a factor of 6 and 10, respectively. These differences of the elemental abundances should significantly affect physical and chemical processes in molecular clouds.

In infrared images of the LMC, the stellar bar and the giant H II region 30 Doradus are prominent. However, molecular clouds are known to be distributed more widely by the CO survey observation in the millimeter-wave region (Fukui & Kawamura (2010) and references therein). Extensive studies have been carried out on molecular-cloud evolution and star formation at a galactic scale. In contrast to Galactic molecular clouds, individual distances to molecular clouds in the LMC are almost the same, which guarantees a constant spatial resolution and thus provides an excellent opportunity for statistical studies of molecular clouds. Taking advantage of this point, an evolutionary time scale of giant molecular clouds in the LMC has been investigated statistically.

So far, chemical compositions of molecular clouds in the LMC were mainly studied toward high-mass star-forming regions containing well-developed H II regions, such as N113 (Wang et al., 2009) and N159 (Heikkilä et al., 1999). Bright molecular emission lines were observed in these sources, and abundances of various molecules derived from such observations are compared with those in high-mass star forming regions in our Galaxy, such as Orion KL and Sgr B2 (Chin et al., 1997; Heikkilä et al., 1999; Wang et al., 2009; Paron et al., 2014). However, the above sources in the LMC involve a cluster of high-mass stars and have a very complex physical structure, and such features prevent us from understanding intrinsic chemical nature of molecular clouds specific to the LMC. For this purpose, we need to observe relatively quiescent molecular clouds without strong influence of cluster formation. Such an effort reported so far is the chemical study of the high-mass star-forming cloud, N44C, toward which several molecules other than CO and their isotopologues are detected (Chin et al., 1997). However, we still need to observe more sources systematically in order to examine the effect of star-formation activities on chemistry and to extract the intrinsic chemical nature.

For the spectral line survey, we first selected candidate sources having different star-formation activities. We selected 16 sources on the basis of the CO map data (MAGMA; Wong et al. (2011)), which are not associated with infrared sources ("starless clouds"). Non-detection of the point sources at 8 μm and 24 μm with *Spitzer* or *AKARI* generally means the absence of high-mass young stellar objects except for very infant ones (Whitney et al., 2008; Gruendl & Chu, 2009; Kato et al., 2012). These "starless" sources are referred to hereafter as Category A sources. We also selected 17 high-mass star forming clouds which are associated with high-mass YSOs observed with *Spitzer* or *AKARI*, but not embedded in prominent H II regions (referred to hereafter Category B sources) (Gruendl & Chu,

2009; Seale et al., 2009; Shimonishi et al., 2010, 2013).

We then observed these candidate sources in the ^{13}CO ($J = 1 - 0$), HCO$^+$ ($J = 1 - 0$), and HCN ($J = 1 - 0$) lines with the Mopra 22 m telescope. As a result, we found the bright sources in the HCO$^+$ and HCN line for each category; CO Peak 1 and NQC2 for Category A and N79, N44C, and N11B for Category B. All of the target regions are associated with relatively strong ^{12}CO ($J = 1 - 0$) emission. Based on the MAGMA CO map of the LMC, a typical CO integrated intensity of the regions such as N159W, N113, and N44BC, in which multiple molecular emission lines were detected by the SEST 15 m telescope, is $16 - 61$ K km s^{-1}. The typical CO integrated intensity of our target sources is $10 - 34$ K km s^{-1}, which is almost comparable to those of the above well-studied sources. Hence, the selected sources are likely molecular rich.

In addition, we included the two active star forming regions with extended H II regions, N113 and N159W (referred to hereafter Category C sources), as references, in our source list. In total, we selected 7 sources for this study, as summarized in Table 3.3. The positions of each cloud is shown in Figure 3.2. The clouds are distributed over the entire galaxy. CO Peak 1 and N159W are located near 30 Doradus, which is the brightest H II region in the LMC, whereas the other clouds are located different parts of the LMC, as described later. Figures 3.3 and 3.4 show the MAGMA CO ($J = 1 - 0$) maps and the 24 μm images by *Spitzer* MIPS of the target sources. A brief description of each source is given below, where the cloud name is based on Henize (1956), if available.

Category A

CO Peak 1 is located at the eastern part of the LMC. It does not host any infrared sources, as shown in Figure 3.3, suggesting that high-mass star formation has not yet started in this cloud. Strong CO ($J = 1 - 0$) emission (31.1 K km s^{-1}) is detected in the MAGMA observations. Deep molecular line observations are carried out for the first time in this study.

NQC2 is a quiescent molecular cloud located at the central part of the LMC. This source was recognized in the *Herschel* PACS map of the LMC, and was confirmed to have fairly strong emission of HCO$^+$ during the above survey (Shimonishi et al., 2016). It also shows a bright CO emission in the MAGMA observations, while it does not harbor 24 μm point sources (Figure 3.3). No molecular line observations have been reported for this source except for that of CO.

Category B

N79 is an H II region located in the western part of the LMC. In this study, we observed a relatively quiescent cloud not directly associated with the H II region. It harbors an embedded high-mass YSO

which shows ice absorption bands (Seale et al., 2009).

N44C is a molecular cloud located in the central part of the LMC. N44C hosts an embedded high-mass YSO named ST2, whose luminosity is estimated to be $\sim 2 \times 10^5 L_\odot$ (Shimonishi et al., 2010). Although a few faint YSOs are present within the observed beam, the total mid-infrared flux toward the N44C region is dominated by the single high-mass YSO, as shown in Figure 3.3. Hence, we selected N44C as a Category B source. Detection of the ice absorption bands in the infrared spectrum of this central YSO (Shimonishi et al., 2010) suggests that the N44C cloud is still in the very early stage of star formation. Note that molecular line observations are observed toward N44BC by Chin et al. (1997), which is separated by $1'$ from our observed position and is not associated with high-mass YSOs. In N44BC, the lines of eight species including HCO^+, HCN, HNC, CCH, CS, and SO are detected in the 3 mm band with the SEST 15 m telescope. Hence, we can compare our result toward N44C with theirs to examine the effect of star formation on the chemical composition.

N11B is a member of N11 complex, the second largest H II region after the 30 Doradus region (Israel et al., 2003b). We observed the position not directly associated with the extended H II region. It involves a relatively evolved YSO, which shows emission lines due to polycyclic aromatic hydrocarbon (PAH) and ionized gas (Seale et al., 2009). Barbá et al. (2003) also reported several embedded YSOs. It is also reported that the CH_3OH maser is associated with this YSO (Ellingsen et al., 2010). Furthermore, a variety of far-infrared emission lines from ionized gas are detected toward our observing position by *Herschel* (Lebouteiller et al., 2012). The above characteristics suggest that the N11B region is relatively evolved in comparison with the other two target sources in this category.

Category C

N113 is an active cluster-forming site located in the central port of the LMC, which is separated from the 30 Doradus region by about 2°. It is associated with prominent H II regions (NGC1874, NGC 1876, and NGC1877) (Bica et al., 1992). This is a well studied source in astrochemistry; several molecular-line studies have been reported (*e.g.* Chin et al., 1997; Wang et al., 2009; Paron et al., 2014).

N159W is one of active cluster-forming regions associated with the H II region LH105 (Lucke & Hodge, 1970). This source has extensively been studied as a prominent on-going star forming region by observations in various wavelength regions (*e.g.* Mizuno et al., 2010; Ott et al., 2010). Molecular line observations are also reported by Johansson et al. (1994); Heikkilä et al. (1999).

Table 3.3. Observed positions in the LMC and their physical properties.

Source Name	$\alpha_{J2000.0}$ (^{h} ^{m} ^{s})	$\delta_{J2000.0}$ ($^\circ$ $'$ $''$)	V_{LSR} (km s^{-1})	^{12}CO (MAGMA[a]) (K km s^{-1})	^{12}CO (this study) (K km s^{-1})	8 μm flux[b] (mJy arcsec^{-2})	24 μm flux[c] (mJy arcsec^{-2})	YSO	H II region	Category
CO Peak 1 ..	05 44 25.3	−69 26 25.9	229	31.1	31.30	26.8	11.7	no	no	A
NQC2	05 19 27.1	−69 08 48.9	266	14.4	13.90	89.0	58.6	no	no	A
N79	04 51 53.1	−69 23 25.3	232	17.6	16.80	946.8	4785.7	yes	no	B
N44C	05 22 11.6	−67 58 26.0	282	21.2	25.58	387.3	2184.0	yes	no	B
N11B	04 56 48.1	−66 24 24.2	285	9.5	18.74	332.5	1341.3	yes	no	B
N113	05 13 18.2	−69 22 35.0	235	30.1	46.96	626.1	2883.8	yes	yes	C
N159W	05 39 36.0	−69 45 35.0	238	34.4	53.4	720.6	2647.5	yes	yes	C

Note. — Units of right ascension are hours, minutes, and seconds, and units of declination are degrees, arcminutes, and arcseconds. V_{LSR} of ^{13}CO are given.

[a]Wong et al. (2011).

[b]*Spitzer* IRAC (Meixner et al., 2006).

[c]*Spitzer* MIPS (Meixner et al., 2006).

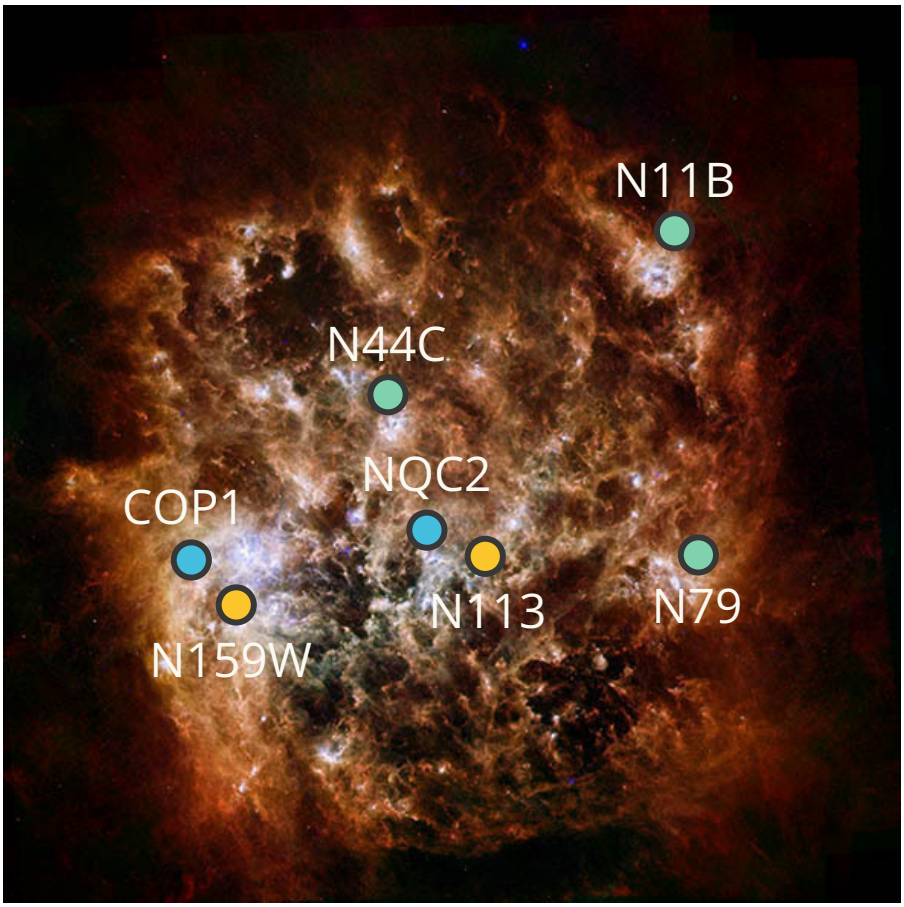

Figure 3.2 The positions of the observed molecular clouds in the LMC. A color image represents the composite image of infrared observations. R: 250 μm (*Herschel*/SPIRE), G: 100, 160 μm (*Herschel*/PACS), B: 24, 74 μm (*Spitzer*/MIPS).

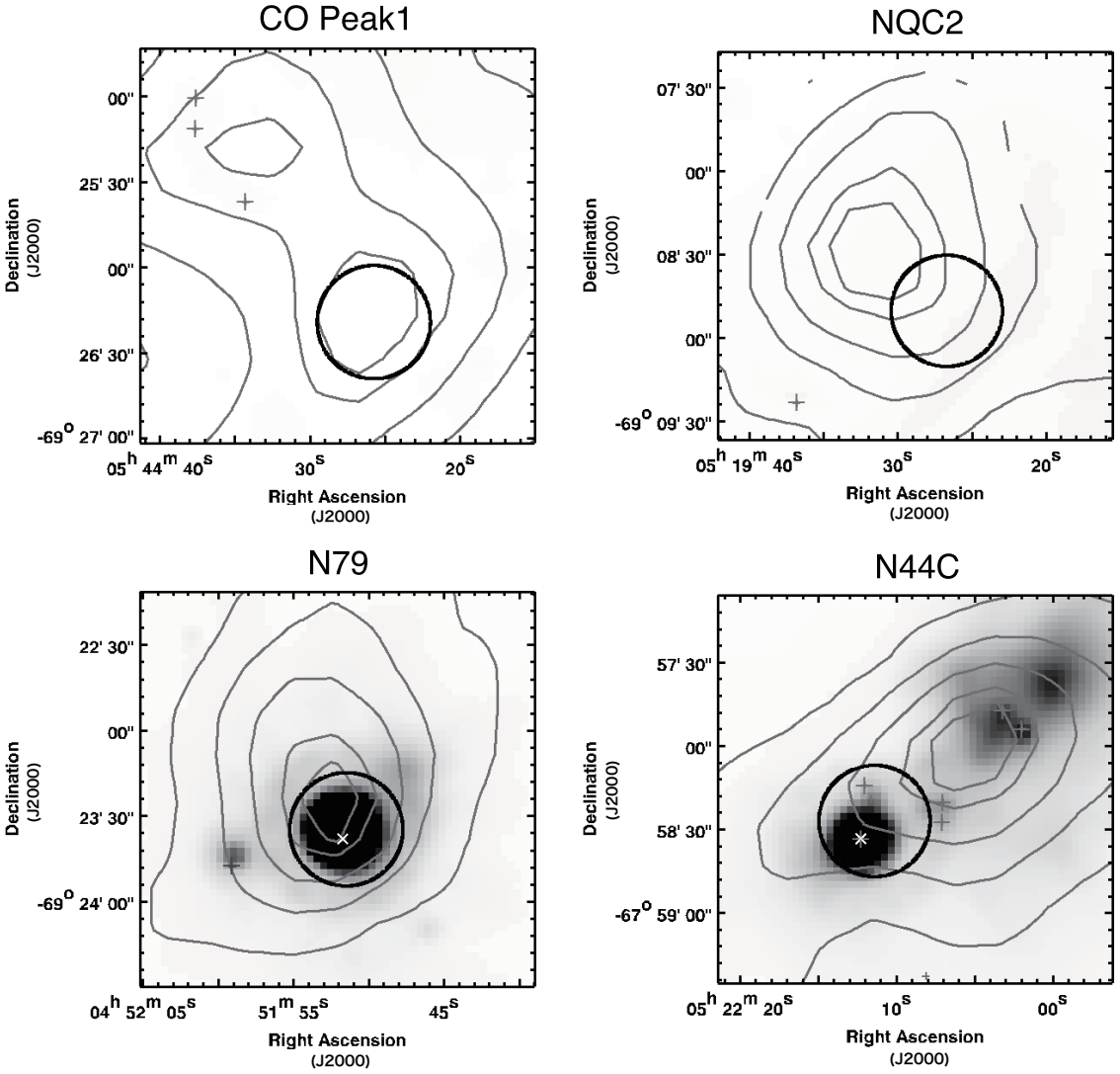

Figure 3.3 CO ($J = 1 - 0$) contours (MAGMA) and 24 μm image (*Spitzer* MIPS) of our target molecular clouds in the LMC. The solid circle represents the beam size of the Mopra telescope in 3 mm ($38'' \sim 10$ pc at the LMC) centered at the observed position. The grey crosses indicate the positions of YSOs candidates reported by Gruendl & Chu (2009), while the white x-marks indicate the positions of particularly bright high-mass YSOs within or near the beam position.

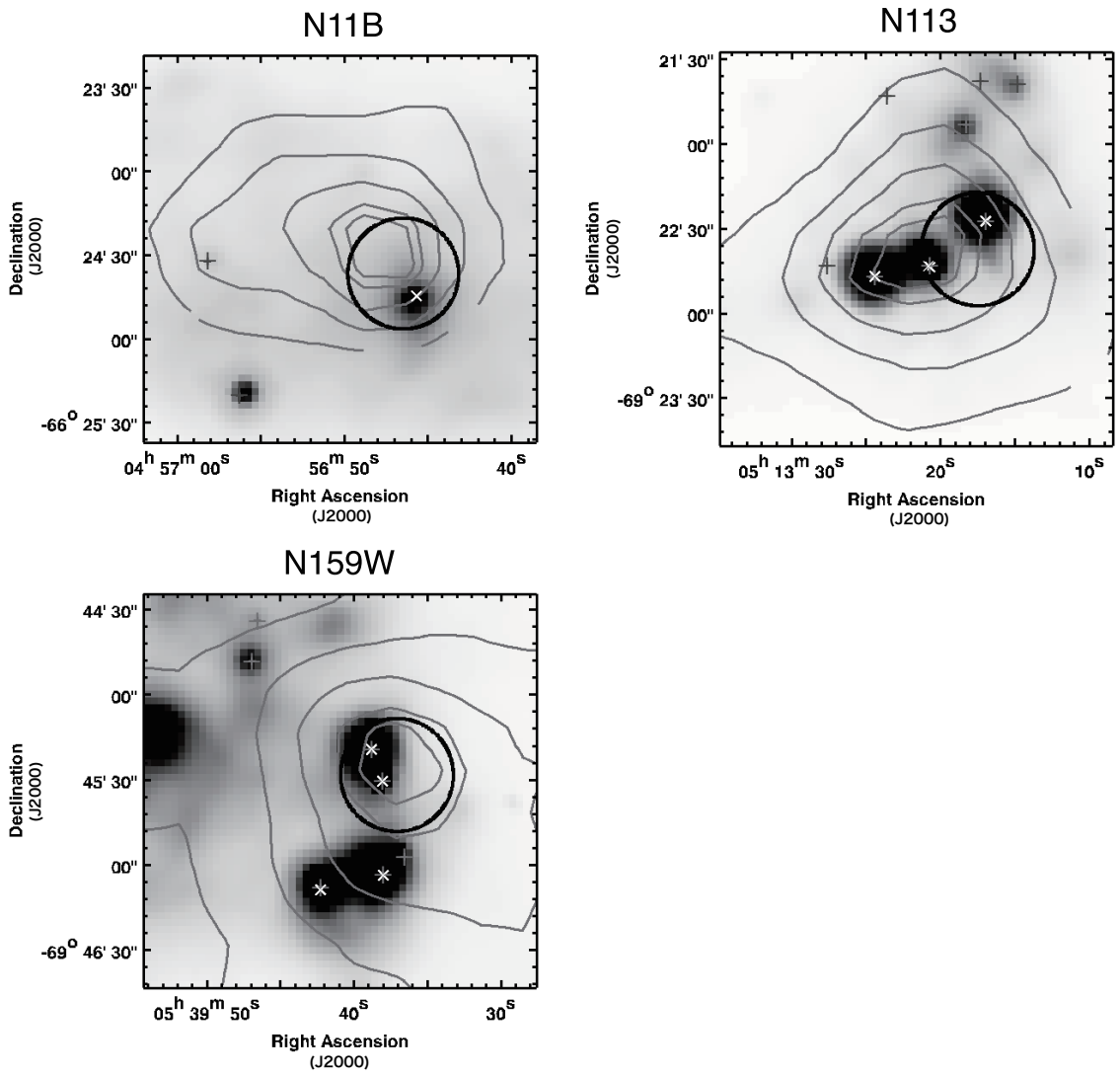

Figure 3.4 Same to Figure 3.3, CO ($J = 1 - 0$) contours (MAGMA) and 24 μm image (*Spitzer* MIPS) of our target molecular clouds in the LMC.

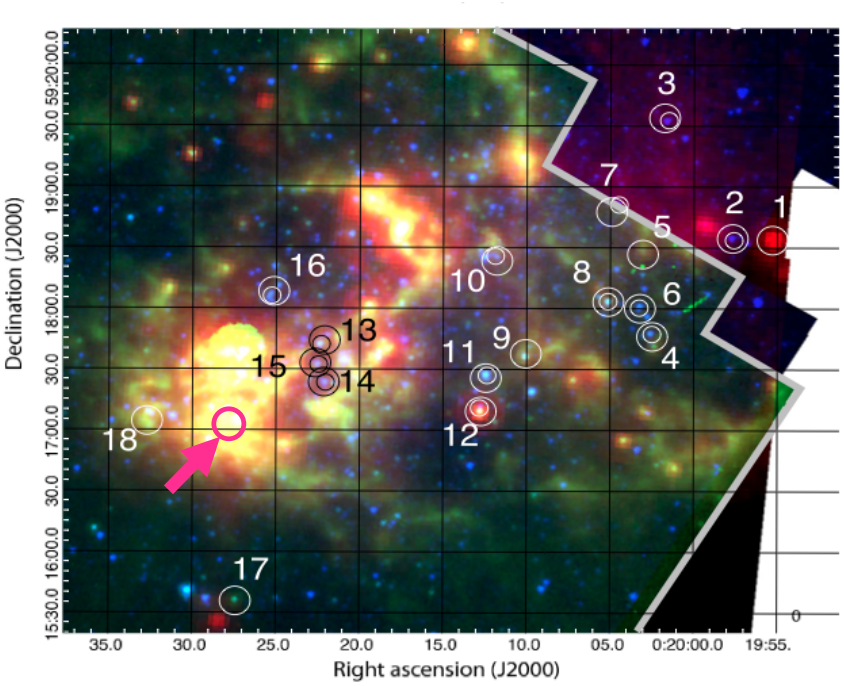

Figure 3.5 The map of IC10 (*JHK*, *Spitzer*/IRAC and *Spitzer*/MIPS), taken from Lebouteiller et al. (2012). The observed position is indicated by a magenta circle.

3.2.2 IC10

IC10 is a member of the Local Group galaxies, and its metallicity is lower by factor 5 than in the Solar neighborhood (Garnett, 1990). Morphologically, IC10 is categorized as an irregular galaxy (dIrr). The distance to IC10 remains somewhat uncertain, because it is located near the Galactic plane ($b = -3.3$). Here, we adopt 950 kpc (Hunter, 2001), which is frequently used in the literature (e.g., Leroy et al., 2006). The star formation rate estimated from the Hα emission ($0.2 M_{\odot}$ yr $^{-1}$; Gil de Paz et al., 2003) and the association of the large number of Wolf-Rayet stars ($\sim$ 100; Massey & Holmes, 2002) imply active star formation in IC10. IC10 has been studied in C II (158 μm) (Madden et al., 1997), C I ($^3P_1 \rightarrow ^3 P_0$) (Bolatto et al., 2000), and multi-transitions of CO (e.g., Petitpas & Wilson, 1998; Bolatto et al., 2000; Leroy et al., 2006). However, molecular line observations except for CO and its isotopologues have not been reported.

We selected the observing position of $\alpha_{\rm J2000} = 00^h20^m27.9^s$, $\delta_{\rm J2000} = 59°17'01.0''$, where the ^{12}CO ($J = 1-0$) line intensity is the strongest in IC10 according to Leroy et al. (2006). The position is also confirmed to be bright in infrared (Figure 3.5; *JHK*, *Spitzer*/IRAC and *Spitzer*/MIPS, Lebouteiller et al., 2012).

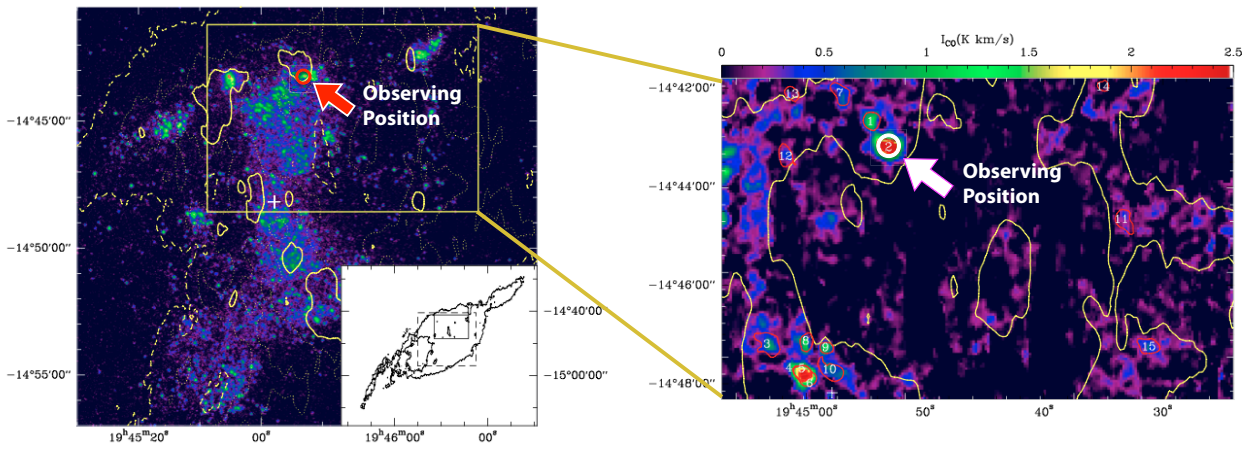

Figure 3.6 (*left*) GALEX FUV filter image of NGC6822, taken by Gratier et al. (2010). Our observing position is indicated by a red circle. (*right*) CO ($J = 2 - 1$) intensity map also taken by Gratier et al. (2010). Our observing position is indicated by a white circle.

3.2.3 NGC6822

NGC6822 is a dwarf irregular galaxy (dIrr) at a distance of about 490 kpc (Mateo, 1998) and is one of the nearest galaxies in the Local Group. This galaxy is studied at various wavelengths in many aspects. Lee et al. (2006) estimated the oxygen abundance of H II regions to be $12 + \log(\mathrm{O/H}) \sim 8.1$ by the optical observation. Hence, the metallicity of NGC6822 is considered to be roughly comparable to IC10.

Molecular-line studies of NGC6822 have been conducted toward one of the brightest H II regions designated Hubble V by Hodge et al. (1988). Although molecular line intensities of this cloud is generally fainter than those of IC10, Petitpas & Wilson (1998) conducted the CO multi-line analysis (^{12}CO $J = 3-2/2-1$) toward a molecular cloud inside Hubble V, and suggested the H_2 density higher than 10^4 cm^{-3} and a kinetic temperature higher than 100 K. Such physical conditions likely originate from the low metallicity and low gas content. In addition to the CO lines, Israel et al. (2003a) reported the detections of HCO^+ ($J = 1 - 0$), CS ($J = 3 - 2$), and H_2CO ($2_{11} - 1_{10}$). Hence, NGC6822 is an excellent target for further studies on chemical composition. Based on the previous studies, we selected the observing position of $\alpha_{\mathrm{J2000}} = 19^h44^m52.85^s$, $\delta_{\mathrm{J2000}} = -14°43'12.68''$ in Hubble V for the spectral line survey (Figure 3.6).

3.2.4 NGC55

NGC55 is an edge-on barred spiral galaxy (SBm) of the Magellanic type, which is located at the distance of 2.2 Mpc (Gieren et al., 2008). It is either a member of the Local Group (Mateo, 1998) or the Sculptor group (van den Bergh et al., 2000). The metallicity of NGC55 is lower by a factor of 3

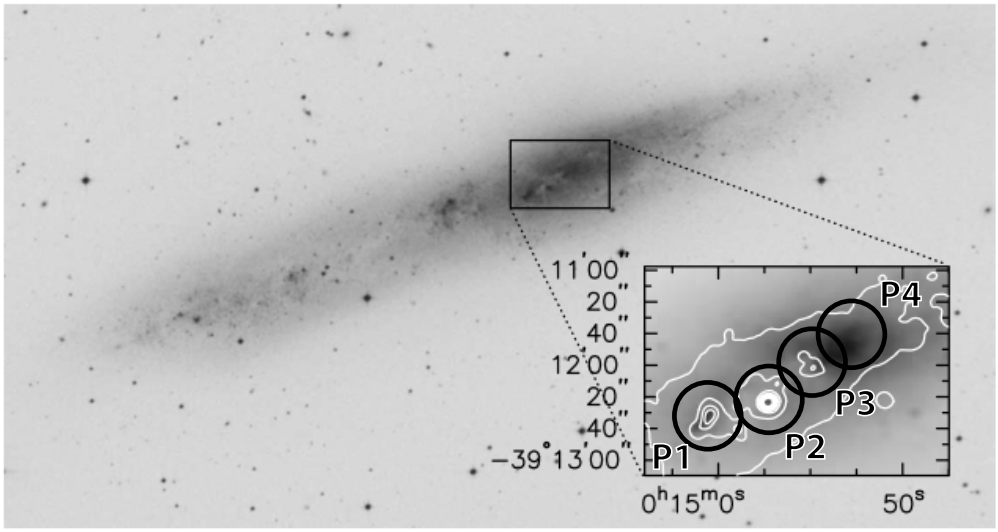

Figure 3.7 Digitized Sky Survey image of NGC55, taken from Engelbracht et al. (2004). The inset shows the I-band image with 24 μm contours in evenly spaced intervals from 50 to 4000 μJy arcsec^{-2}. The observed position in this study, P1, P2, P3, and P4 are indicated by bold black circles.

than that of the Solar neighborhood (Hartoog et al., 2012). In optical and infrared studies, NGC55 is often recognized to be similar to the LMC for its luminosity, morphological type, and metallicity. Indeed, NGC55 is one of the brightest galaxies according to the *Spitzer* 8 μm images of 15 nearby dwarf galaxies in the Local Group (Jackson et al., 2006).

As for molecular line studies, the detection of the ^{12}CO ($J = 1 - 0$) emission was reported by Dettmar & Heithausen (1989). After this study, the ^{12}CO ($J = 1 - 0$) and ^{13}CO ($J = 1 - 0$) lines were also detected by Becker & Freudling (1991) and Israel et al. (1995). However, observations of molecular lines other than ^{12}CO and ^{13}CO have not been reported.

In this study, we observed the positions P1, P2, P3, and P4, which are located in a bright central region (Figure 3.7). They are summarized in Table 3.4. Toward P2, where the ^{12}CO ($J = 1 - 0$) line is detected, we also observed the HCO^+ and CS lines and derived their upper limits to the intensities.

3.2.5 NGC185

NGC185 is a dwarf spheroidal (dSph) or elliptical galaxy (dE3), and is one of the four brightest satellite galaxies of M31 (the Andromeda Galaxy) together with NGC205, NGC147, and NGC221 (M32). Unlike the other three dwarf companions of M31, NGC185 is found to be rich in gas and dust (Marleau et al., 2010).

The oxygen abundance of NGC185 is $12 + \log(\mathrm{O/H}) \sim 8.2$ (Richer & McCall, 1995), which implies that the metallicity of NGC185 is almost comparable to IC10, NGC6822, and NGC55. The distance

Table 3.4. The observed positions of NGC55.

Position	$\alpha_{\rm J2000.0}$ (^{h} ^{m} ^{s})	$\delta_{\rm J2000.0}$ ($^\circ$ $'$ $''$)
P1	00 15 00.4	−39 12 35.0
P2	00 14 57.6	−39 12 25.0
P3	00 14 55.0	−39 12 03.0
P4	00 14 51.9	−39 11 40.0

Note. — Units of right ascension are hours, minutes, and seconds, and units of declination are degrees, arcminutes, and arcseconds.

to NGC185 is estimated to be 620 kpc (McConnachie et al., 2005). Based on the infrared observation, NGC185 seems to have experienced the last starburst a few 10^8 yr ago, although its current star formation rate is quite low (Marleau et al., 2010).

As for molecular line studies, Young & Lo (1997) reported that the peak temperature of the CO $J = 1-0$ line is 0.1 K with IRAM 30 m telescope. Young (2001) also reported the peak CO temperature of 1.1 K toward the same position with the BIMA interferometer. The CO distribution is consistent with the dust distribution revealed by the optical observations (e.g., Hodge, 1963). Considering these reports, we observed the CO peak position (Young, 2001, $\alpha_{\rm J2000} = 00^h38^m56.6^s$, $\delta_{\rm J2000} = 48^\circ20'19''$) in this study (Figure 3.8).

3.3 Observations

3.3.1 The LMC

The spectral line survey observations were carried out with the Mopra 22 m telescope of the Australia Telescope National Facility (ATNF) from June to October in 2013 and from April to October in 2014. We observed the 7 sources mentioned above (Section 3.2.1); CO Peak 1, NQC2, N79, N44C, N11B, N113, and N159W (Table 3.3). The observed frequency range is from 85 GHz to 116 GHz. We observed two orthogonal polarization signals simultaneously. For NQC2, N79, and N113, the frequency range from 101 GHz to 108 GHz is missing. We did not observe this frequency range for these three sources to save the telescope time, because no spectral lines were detected in the other sources (Table 3.5). The half-power beam width (HPBW) of the telescope is $38''$ and $30''$ at 90 and 115 GHz, which corresponds to 9.5 pc and 7.5 pc at the LMC distance, respectively. The telescope pointing was checked by observing nearby SiO maser source (R Dor) every 1.5 hours, and the pointing accuracy was estimated to be better than $\pm5''$. We used the Mopra spectrometer (MOPS) in the

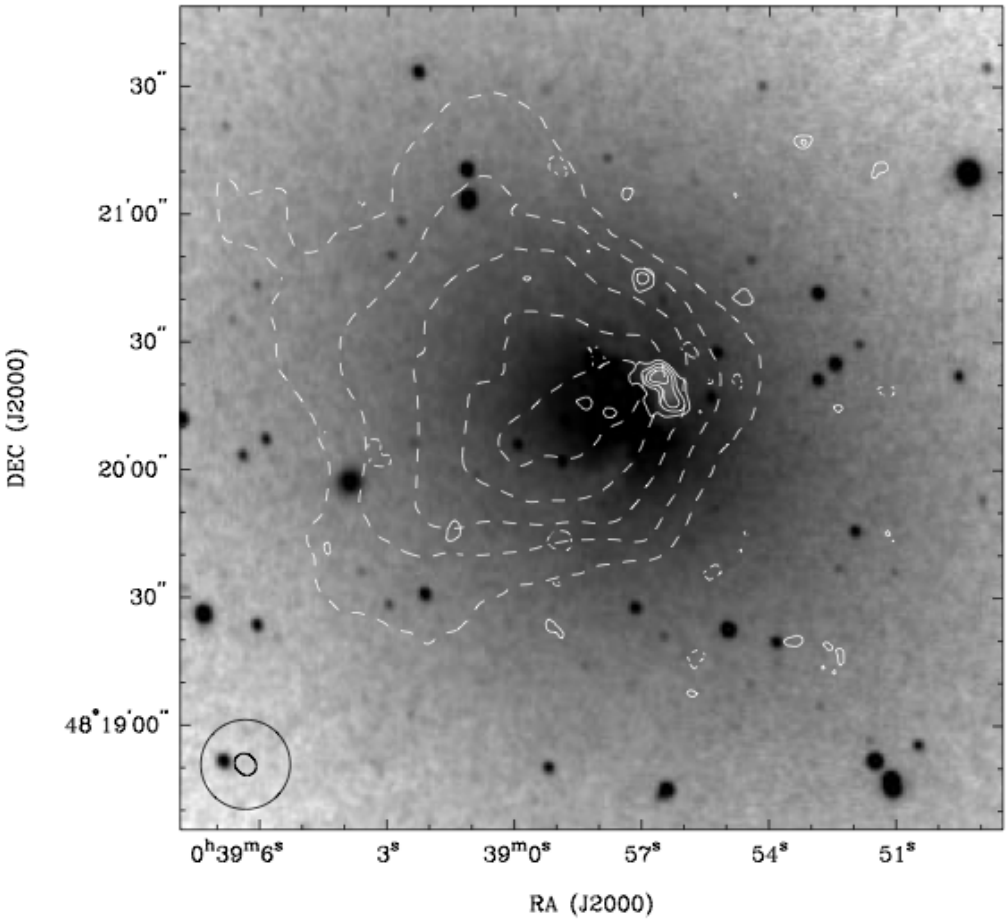

Figure 3.8 CO (solid contours) and H I (dashed contours) on an optical image of NGC185, taken from (Young, 2001). We observed the CO peak position.

Table 3.5. Achieved sensitivity and detected molecules in the LMC.

Source Name	85-93 GHz[a] r.m.s.[b] (mK)	93-101 GHz r.m.s.[b] (mK)	100-108 GHz r.m.s.[b] (mK)	108-116 GHz r.m.s.[b] (mK)	Detected Molecules
CO Peak 1 ..	5.9	10.0	6.6	40.2	CCH, HCN, HCO^+, HNC, CS, SO, ^{13}CO, ^{12}CO
NQC2	6.5	6.4	–	20.0	CCH, HCN, HCO^+, HNC, CS, SO, ^{13}CO, ^{12}CO
N79	13.4	14.4	–	23.3	c-C_3H_2, CCH, HCN, HCO^+, HNC, CS, SO, ^{13}CO, CN, ^{12}CO
N44C	8.3	8.5	14.0	29.3	c-C_3H_2, CCH, HCN, HCO^+, HNC, CS, SO, ^{13}CO, CN, ^{12}CO
N11B	10.0	9.3	7.1	23.2	c-C_3H_2, CCH, HCN, HCO^+, HNC, CS, SO, ^{13}CO, ^{12}CO
N113	22.3	24.3	–	58.8	c-C_3H_2, CCH, HCN, HCO^+, HNC, N_2H^+, CS, SO, ^{13}CO, CN, ^{12}CO
N159W	14.9	18.9	25.3	80.9	c-C_3H_2, CCH, HCN, HCO^+, HNC, N_2H^+, CS, SO, ^{13}CO, ^{12}CO

[a]The observed frequency is from 85 GHz to 93 GHz except for CO Peak 1, for which the range is from 85.25 GHz to 93.25 GHz.

[b]The root mean-square noise of the compressed spectra in the main-beam temperature ($T_{\rm MB}$) scale.

Wideband mode, which simultaneously covers the band width of 8 GHz, as a backend. The frequency resolution is 270 kHz per channel, and we binded 3 successive channels in the analysis to improve the signal-to-noise ratio. The resultant velocity resolution is 2.73 km s^{-1} at 90 GHz. We employed the position-switching mode (OFF-ON-ON-OFF sequences) with individual integrations of 30 s for all the observations.

The total on-source integration time was 16, 25, 8, 17, and 26 hours for CO Peak 1, NQC2, N79, N44C, and N11B respectively. Since the active star-forming regions, N113 and N159W, are very bright in molecular emission, we conducted shorter observations. A typical system temperatures were $\sim$ 200 K and $\sim$ 600 K at 90 GHz and 115 GHz, respectively. A typical rms noise temperature in the main-beam temperature scale for each source and each frequency bands is summarized in Table 3.5. It ranges from 5.9 mK to 80.9 mK, depending on the frequencies and the sources. The line intensity was calibrated by the chopper wheel method, and a typical calibration accuracy is 20%. The antenna temperature is divided by the main beam efficiency of 0.5 to obtain the main-beam temperature, $T_{\rm MB}$. The observation data were first reduced with the ATNF analysis programs, ASAP, and then detailed analyses were carried out using our own codes.

3.3.2 IC10

The observations were carried out with the 45 m radio telescope at Nobeyama Radio Observatory (NRO) in February and March in 2015. We observed a single position with the brightest CO line in IC10 (Table 3.1). We observed the most part of the frequency range from 84 to 116 GHz. We did not observe the frequency range of $91 - 91.5$, $95.5 - 96$, $100 - 103.5$, and $107.5 - 108$ GHz, because no spectral lines were detected in the LMC sources (Table 3.5). The half-power beam width (HPBW) of the telescope is $20.4''$, $16.6''$ and $15.3''$ at 86, 110 and 115 GHz, respectively. They correspond to the spatial scale from 71.7 to 98.8 pc at the IC10 distance ($d = 950$ kpc). The telescope pointing was checked by observing the nearby SiO maser source (Y Cas) every hour, and the pointing accuracy was maintained to be better than $\pm 5''$. We observed two orthogonal polarization signals simultaneously by using the SIS mixer receiver (TZ1), whose system temperatures ranged from 120 to 280 K. The backend is the autocorrelator SAM45. The frequency resolution and bandwidth are 488.24 kHz and 1600 MHz, respectively. We binded 2 successive channels of SAM45 in the analysis to improve the signal-to-noise ratio. The resultant velocity resolution is 3.25 km s^{-1} at 90 GHz. The line intensity was calibrated by the chopper wheel method, and a typical calibration accuracy is 20%. The antenna temperature is divided by the main beam efficiency of 0.49 at 86 GHz, 0.42 at 100 GHz, and 0.40 at 115 GHz to obtain the main beam temperature $T_{\rm MB}$. We employed the position-switching mode, where the on-source integration time of each scan was set to be 20 seconds for all the observations. The off-source position is $3'$ away in azimuth from the on-source position. The total observation time was 55 hours ($\sim$ 18 hours for on-source). A typical rms noise temperature for each line in the $T_{\rm MB}$ scale is $2.5 - 8.0$ mK for $84 - 112$ GHz and $31 - 53$ mK for $112 - 116$ GHz at a frequency resolution of 976.5 kHz.

3.3.3 NGC6822

The observations were carried out with the IRAM 30 m telescope in December 2015. We observed a single position (Table 3.1) in the frequency range from 85 to 116 GHz and from 140 to 148 GHz. The half-power beam width (HPBW) of the telescope is $29''$, $23''$ and $16''$ at 86, 115 and 145 GHz, respectively. They correspond to the spatial scale from 71, 56, and 39 pc at the NGC6822 distance ($d = 490$ kpc), respectively. The telescope pointing was checked by observing the continuum sources near the target position every hour, and the pointing accuracy was maintained to be better than $\pm 5''$. We employed the wobbler switching mode with a beam throw of $\pm 100''$ in the azimuth direction and switching frequency of 0.5 Hz.

We observed two orthogonal polarization signals simultaneously by using EMIR, whose system

temperatures ranged from 90 to 350 K for E090 band (the frequency range of $85-116$ GHz) and 110 to 170 K for E150 band ($140-148$ GHz). The backend is Fast Fourier Transform Spectrometers (FTS). We employed the wideband mode, whose frequency resolution and bandwidth are 195 kHz and 32 GHz, respectively. We binded 2 successive channels in the analysis to improve the signal-to-noise ratio. The resultant velocity resolution is 1.3 km s^{-1} at 90 GHz. The antenna temperature is scaled by multiplying $F_{\rm eff}/B_{\rm eff}$ to obtain the main beam temperature $T_{\rm MB}$. Here, the main beam efficiency ($B_{\rm eff}$) is 0.81 at 86 GHz, 0.78 at 115 GHz, and 0.74 at 145 GHz and the forward efficiency ($F_{\rm eff}$) is 0.95 at 86 GHz and 0.93 at 145 GHz. The total observation time was 29 hours. A typical rms noise temperature for each line in the $T_{\rm MB}$ scale is 4.3 mK for $85-116$ GHz and 2.5 mK for $140-148$ GHz at a frequency resolution of 0.39 MHz.

3.3.4 NGC55

The observations were carried out with the Mopra 22 m telescope from April to July in 2015. We observed 4 positions; P1, P2, P3, and P4 (Table 3.4). We observed the CO ($J=1-0$) line at 115 GHz for all four positions. For P1, we also observed the HCO$^+$ ($J=1-0$) and CS ($J=1-0$) lines. We observed two orthogonal polarization signals simultaneously. The half-power beam width (HPBW) of the telescope is $30''$ at 115 GHz, which corresponds to 330 pc at the distance of NGC55. The telescope pointing was checked by observing the nearby SiO maser source (R Hor) every 1.5 hours, and the pointing accuracy was estimated to be better than $\pm5''$.

We used the Mopra spectrometer (MOPS) in the Wideband mode, which simultaneously covers the band width of 8 GHz, as a backend. The frequency resolution is 270 kHz per channel, and we binded 3 successive channels in the analysis to improve the signal-to-noise ratio. The resultant velocity resolution is 2.11 km s^{-1} at 115 GHz. We employed the position-switching mode (OFF-ON-ON-OFF sequences) with individual integrations of 30 s for all the observations. The total on-source integration time for CO observation was 9, 20, 3, and 1.5 hours for P1, P2, P3, and P4, respectively. Additionally, we observed the HCO$^+$ and CS lines toward P1 for 48 hours and 20hours, respectively. A typical system temperatures were $\sim$ 600 K at 115 GHz. The line intensity was calibrated by the chopper wheel method, and a typical calibration accuracy is 20%. The antenna temperature is divided by the main beam efficiency of 0.5 to obtain the main-beam temperature, $T_{\rm MB}$. The observation data were first reduced with the ATNF analysis programs, ASAP, and then detailed analyses were carried out by using our own codes.

3.3.5 NGC185

The observations were carried out with the 45 m radio telescope at Nobeyama Radio Observatory (NRO) in March and April in 2015. We observed a single position shown in Table 3.1. We observed the frequency range of $87-91$, $96-104$, and $108-116$ GHz. The half-power beam width (HPBW) of the telescope is $20.4''$, $16.6''$ and $15.3''$ at 86, 110 and 115 GHz, respectively. They correspond to the spatial scale from 47.4 to 63.2 pc at the NGC6822 distance ($d = 620$ kpc). The telescope pointing was checked by observing the nearby SiO maser source (T Cas) every hour, and the pointing accuracy was maintained to be better than $\pm 5''$.

We observed two orthogonal polarization signals simultaneously by using the SIS mixer receiver (TZ1), whose system temperatures ranged from 120 to 280 K. The backend is the autocorrelator SAM45. The frequency resolution and bandwidth are 488.24 kHz and 1600 MHz, respectively. We binded 2 successive channels of SAM45 in the analysis to improve the signal-to-noise ratio. The resultant velocity resolution is 3.25 km s^{-1} at 90 GHz. The line intensity was calibrated by the chopper wheel method, and a typical calibration accuracy is 20%. The antenna temperature is divided by the main beam efficiency of 0.49 at 86 GHz, 0.42 at 100 GHz, and 0.40 at 115 GHz to obtain the main beam temperature $T_{\rm MB}$. We employed the position-switching mode, where the on-source integration time of each scan was set to be 20 seconds for all the observations. The off-source position is $3'$ away in azimuth from the on-source position. The total observation time was 49 hours ($\sim$ 16 hours for on-source).

3.4 Results

3.4.1 The LMC

Observed Spectra and Line Parameters toward the LMC

Figures 3.9a - 3.9f show compressed spectra from 85 GHz to 101 GHz toward CO Peak 1, NQC2, N79, N44C, N11B, N113, and N159W, respectively. In preparation of these data, we corrected slight intensity variation among the subscans for 1.5 hours by using the intensity of the strongest line of the observing band. For the compressed spectra, we subtracted the baseline by using the 5th-order polynomial over the 2.2 GHz region. Although the standing waves caused by the telescope system are still visible, we were readily able to identify emission lines, because a typical line width observed toward the target sources (5 km s^{-1}) is narrower than the period of the standing waves. Lines are identified with the aid of the spectral line database CDMS (Müller et al., 2001; Müller et al., 2005). We used the ^{13}CO line velocity ($V_{\rm LSR}$) of 229, 266, 285, 282, 232, 235 and 238 km s^{-1} for CO Peak 1,

NQC2, N11B, N44C, N79, N113, and N159W, respectively, to identify molecular lines. We detected 8 molecules (CO, ^{13}CO, CS, SO, CCH, HCO^+, HCN, and HNC) in the seven sources, c-C_3H_2 in N79, N44C, N11B, N113, and N159W, and CN in N79, N44C, and N113 (Table 3.6). N_2H^+ is marginally detected in N113 and N159W. The detection criterion is that the line is detected at the expected velocity with the significance of 5σ or higher in the integrated intensity. Note that the c-C_3H_2 line was not covered with the frequency setting for CO Peak 1. Since line intensities in CO Peak 1 and NQC2 are typically weaker by a factor of 2 than the other sources, a fewer lines were detected in these sources. The signal-to-noise ratio is rather poor for N113 and N159W in comparison with the previous studies (Wang et al., 2009; Heikkilä et al., 1999; Chin et al., 1997), and hence, only strong lines were detected in this study.

The spectral line profiles of detected molecules are shown in Figures 3.10 and 3.11. For Figures 3.10 and 3.11 and Table 3.6, the baselines are subtracted in a narrow range (typically 100 MHz) by using the 5th-order polynomials to remove the baseline ripples. We conducted Gaussian fitting to each base-line-subtracted spectral line to obtain the $V_{\rm LSR}$, Δv, and the peak $T_{\rm MB}$, where the observed frequencies are converted to the LSR velocities based on the rest frequency of each transition given in CDMS. Derived line parameters are summarized in Table 3.6.

Although the seven sources have different star-formation activities, as mentioned in Section 3.2.1, the spectral intensity patterns of the seven sources look similar to one another, except for a slight difference discussed later. In order to reveal the similarity, we inspected the molecule-to-molecule correlation of the integrated intensities of the 7 sources. The correlation coefficient c is calculated as

$$c = \frac{\sum(x_i - \bar{x})(y_i - \bar{y})}{\sqrt{\sum(x_i - \bar{x})^2 \sum(y_i - \bar{y})^2}}$$

where x_i and y_i are observed integrated intensities for the i-th source. $\bar{x}$ and $\bar{y}$ are the averages of x_i and y_i, respectively. If the correlation is good, the relative abundance between the two species is similar despite the different column densities along the line of sight. Table 3.7 shows the results for the 7 species. The correlation coefficients are generally higher than 0.9, except for ^{13}CO, indicating that the relative abundances of any pair of CCH, HCN, HCO^+, HNC, CS, and SO are similar among the 7 sources. On the other hand, the correlation coefficients between ^{13}CO and the other species are lower than 0.8. Thus the abundances of CCH, HCN, HCO^+, HNC, CS, and SO relative to ^{13}CO show more source-to-source variation. This implies that the emitting region of the ^{13}CO line is different from those of the other species, because of its lower critical density and/or possible saturation effect of the ^{13}CO line.

In this study, we observed the position involving the bright 24 μm source for N44C. On the other hand, Chin et al. (1997) observed various molecular lines toward the position offset by $1'$ with the

SEST 15 m telescope, whose beam does not involve the bright 24 μm source. We confirmed that the spectral intensity pattern constructed from the line intensity data observed by (Chin et al., 1997) is very similar to our result. This fact further suggests that star-formation activities would not seriously affect the chemical composition at a 10 pc-scale.

Thus, an important result of this study is that the spectral intensity pattern observed at 3 mm with Mopra is similar for all the observed sources in the LMC, although these sources have different star formation activities. The previous studies focus on particular sources (e.g., N113 and N159W) with higher sensitivity and often with higher excitation lines. As a result, the chemical composition derived from these studies is more or less specific to each source. In contrast, we are extracting a common feature of the chemical composition averaged over the molecular cloud scale (10 pc scale) with Mopra. Such a chemical composition is almost free from the influence of individual star formation activities, and can be used to study the characteristic chemical composition specific to low-metallicity conditions of the LMC.

As mentioned in Section 3.1, a similar result for molecular-cloud scale chemical compositions in a much larger scale (kpc scale) is recently reported for the spiral arm clouds of the external galaxy M51 (Watanabe et al., 2014). They observed the two positions, P1 and P2, in the spiral arm of M51, which are separated by 20″, with the IRAM 30 m telescope. Although the star formation efficiency evaluated from the Hα and 24 μm emission is higher in P1 than in P2 by a factor of 1.5, the chemical composition is essentially the same in the two positions. Thus, local star formation and its feedback do not strongly affect the spectral pattern observed at a resolution of a molecular-cloud scale. The spectrum of M51 P1 is shown in Figure 3.9h.

Comparison of our result in the LMC with the Galactic sources is not easy. Apparently, the observed spectral intensity pattern does not reflect those of star forming cores, but that averaged over the molecular cloud scale. In fact, the spectral intensity pattern observed in this study is much different from those of the Galactic star forming regions such as Orion KL and NGC 2264 (Figure 3.9j and k Watanabe et al., 2015). Hence, we need the chemical composition of the Galactic sources averaged over the molecular cloud scale (10 pc) for fair comparison. Although molecular clouds harbors dense cores and star forming cores, most parts of them would be less dense. Hence, it is worth comparing our result in the LMC with the chemical composition of the translucent clouds as the best possible effort. Turner and his collaborators observed the HCO^+, HCN, HNC, CS and SO lines toward many translucent clouds with the total visual extinction (A_v) of about $2-4$ magnitude and H_2 density of $10^3 - 10^4$ cm^{-3} (Turner, 1994, 1995a,b, 1996; Turner et al., 1997; Turner, 1998; Turner et al., 1999, 2000). We averaged the intensities of 38 translucent clouds, and prepared a hypothetical spectrum of

a translucent cloud, as shown in Figure 3.9i. Note that molecules other than HCN, HCO^+, HNC, CS, and SO lines are not included in the hypothetical spectrum due to the lack of the available data for the translucent clouds. More detailed comparison with metal-rich environment will be presented later in Section 3.5.

Column Densities

We evaluated beam-averaged column densities by statistical equilibrium calculations using the RADEX code (van der Tak et al., 2007). This is a non-LTE (local thermodynamic equilibrium) excitation calculation code, where the radiation processes (emission and absorption) and the collisional process with H_2 are balanced to evaluate the population of each rotational levels. This program calculates the line intensity from the column density, the gas kinetic temperature, and the H_2 density. Since only one rotational transition was observed for each molecular species, we assumed a range of the gas kinetic temperature to be 10 K, 20 K, 30 K, 40 K, and 50 K and a range of the H_2 density to be 3×10^3 cm^{-3}, 1×10^4 cm^{-3}, 3×10^4 cm^{-3}, and 1×10^5 cm^{-3}, and derived the column density. The results are summarized in Tables 3.8-3.14.

Abundant S-bearing Molecules in CO Peak 1

Although the spectra observed toward the seven sources in the LMC are similar to one another as a whole, we find a slight but significant difference of the CS and SO abundance. Figure 3.12 shows correlation diagrams of integrated intensities for the five species (HCO^+, HCN, HNC, CS, and SO) for the three sources (N113, N44C, and CO Peak 1). The sulfur-bearing species (CS and SO) tend to be abundant in CO Peak 1. To confirm this trend, we evaluated the CS/HCO^+ and SO/HCO^+ abundance ratios for the seven LMC clouds from the column densities. The results are shown in Figure 3.13. The abundances of CS and SO relative to HCO^+ tend to be higher in CO Peak 1 by factor of 2 than the averages for the other 6 sources. Star-formation activities would enhance the abundance of the sulfur-bearing molecules, because it is generally thought that liberation of sulfur atoms and/or sulfur-bearing molecules by outflow shocks and photostellar heating is responsible for the enhancement (e.g., Wakelam et al., 2005, 2011). However, the slight enhancement of CS and SO relative to HCO^+ in CO Peak 1 is not an effect of star-formation activity, because CO Peak 1 does not harbor high-mass YSOs. In our observations of the seven sources, the abundances of sulfur-bearing species are the highest in the quiescent cloud, CO Peak 1. We here consider the two possible reasons for this result.

The trend may be caused by depletion of S in evolved molecular clouds, or by deficiency of HCO^+

in young molecular clouds. First, we consider the former possibility. In molecular clouds, sulfur is believed to be heavily depleted on dust grains. In chemical models, the gas-phase abundance of sulfur is usually assumed to be only 1/100 of the total elemental abundance (*e.g.* Wakelam et al., 2011; Aikawa et al., 2008; Leung et al., 1984; Graedel et al., 1982). On the other hand, it is observationally known that sulfur is much less depleted in diffuse clouds than in molecular clouds (Lehner et al., 2004; Van Steenberg & Shull, 1988; Morton, 1974). Hence, sulfur would be depleted onto dust grains along molecular-cloud formation. In this context, the higher CS/HCO^+ and SO/HCO^+ ratio in CO Peak 1 than in more evolved clouds suggests that sulfur depletion is not yet completed in CO Peak 1. Because of the low metallicity, extinction of UV and visible light is less effective in the LMC than in our Galaxy for a given H_2 column density, and the dust temperature of the molecular clouds (in particular the temperature of their peripheries) is expected to be higher in the LMC than in our Galaxy (Aguirre et al., 2003; Sakon et al., 2006). The adsorption temperature of sulfur is estimated to be about 20 K by using the adsorption energy of 1100 K (Ruffle & Herbst, 2000). Hence, the sulfur depletion would be less efficient for molecular clouds in the LMC. As a result, sulfur-bearing molecules would still be abundant in the gas phase. The decrease of the CS/HCO^+ and SO/HCO^+ ratios may reflect gradual depletion of sulfur along the evolution of molecular clouds. However, it should be noted that such enhancement of sulfur-bearing molecules is not apparently seen in another quiescent cloud, NQC2. Indeed, the trend is weakened by taking an average in each category defined in Section 3.2.1 (Figure 3.15). Hence, this trend may be specific to CO Peak 1, or NQC2 may be more evolved than CO Peak 1.

Secondly, the above results may be due to the low abundance of HCO^+ in CO Peak 1. If the average density is relatively lower in CO Peak 1 than the other sources, the ionization degree is expected to be higher in CO Peak 1 due to contribution of photoionization. Since HCO^+ is produced by the reaction of $H_3^+ + CO$, its formation rate depends on the H_3^+ ion abundance. The enhancement of ionization degree (*i.e.* the electron abundance) by the photoionization leads to a lower abundance of H_3^+, and thereby a lower abundance of HCO^+. Above all, the HCO^+ abundance may be lower in CO Peak 1, which would also contributes to the trend observed in Figure 3.13.

Relative contributions of the above two possibilities are difficult to be discriminated only from the present data. It is worth noting that the CS/HCN ratio seems to show a similar trend to the CS/HCO^+ ratio in spite of large uncertainties (Figure 3.14 and 3.16). This suggests that the first possibility may work at least partly. Although further statistical studies are necessary for a definitive conclusion, the CS/HCO^+ and SO/HCO^+ ratios may be used as an evolutionary tracer of molecular clouds.

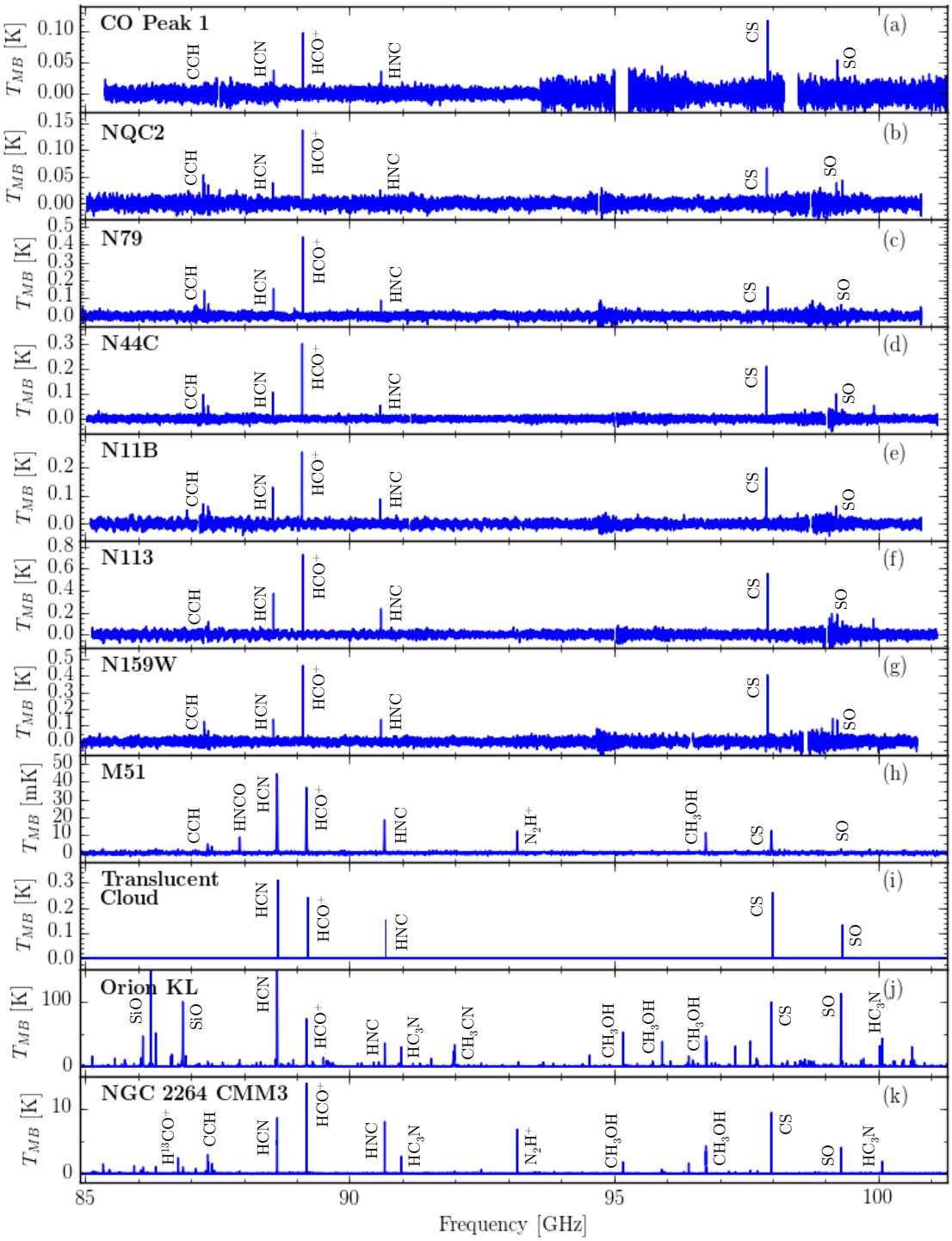

Figure 3.9 Compressed spectra observed toward (a) CO Peak 1, (b) NQC2, (c) N79, (d) N44C, (e) N11B, (f) N113, and (g) N159W. (h) The spectrum of the spiral arm of M51 P1 taken from Watanabe et al. (2014). (i) The composite spectrum of a translucent cloud prepared by averaging the intensities of HCN, HCO^+, HNC, CS and SO observed toward 38 translucent clouds by Turner (1995a,b, 1996); Turner et al. (1997). The spectrum of (j) Orion KL and (k) NGC 2264 CMM3 are taken from Watanabe et al. (2015). Note that the vertical scale is different from source to source.

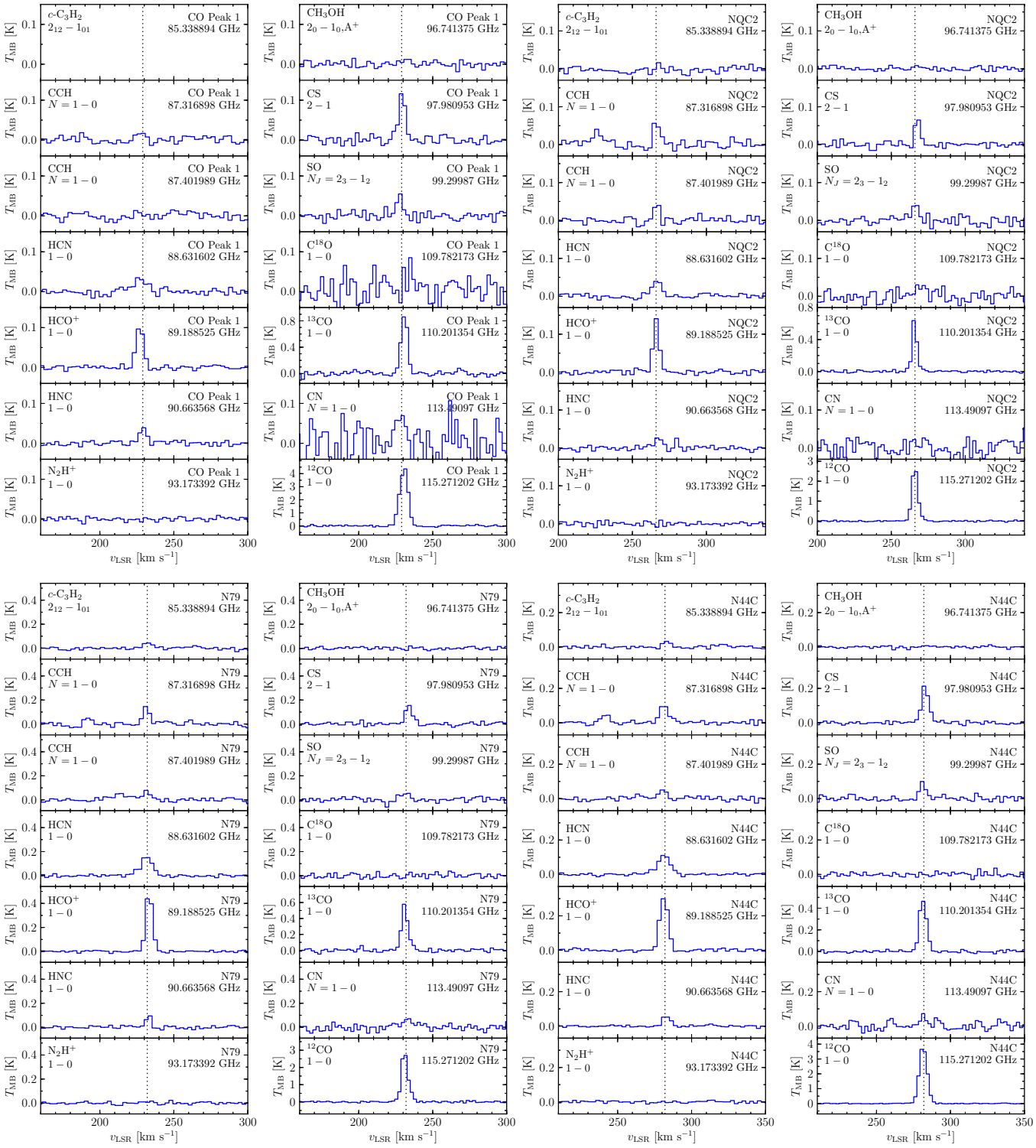

Figure 3.10 Spectral line profiles of individual molecular transitions observed in CO Peak 1, NQC2, N79, and N44C.

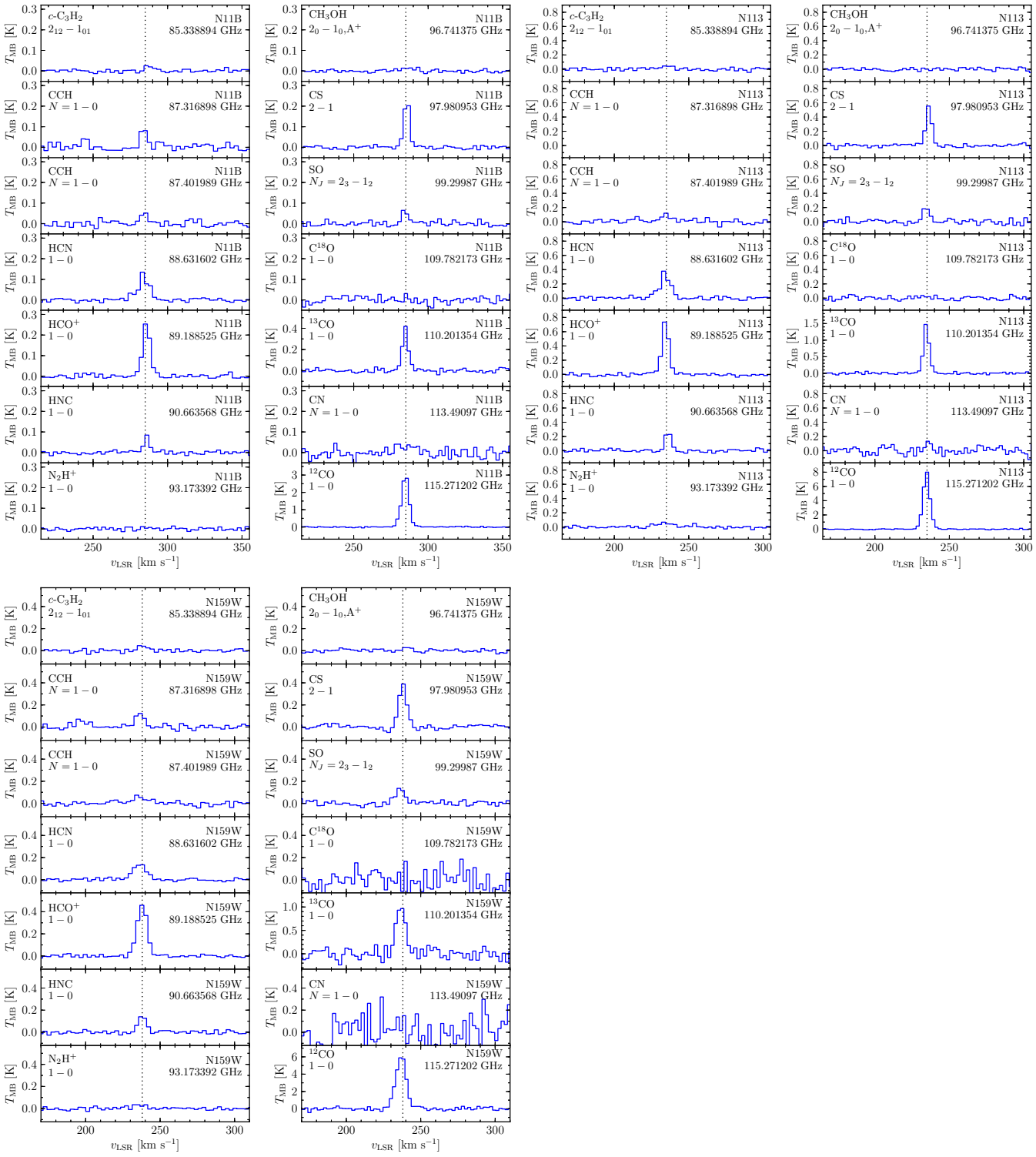

Figure 3.11 Spectral line profiles of individual molecular transitions observed in N11B, N113, and N159W.

Table 3.6. Observed line parameters toward the LMC sources.

Source/ Molecule	Frequency (GHz)	Transition	$T_{\rm MB}$ Peak (K)	$v_{\rm LSR}$ (km s^{-1})	Δv (km s^{-1})	$\int T_{\rm MB} dv$ (K km s^{-1})
(CO Peak 1)						
CCH	87.284105	$N = 1-0$, $J = 3/2-1/2$, $F = 1-1$				< 0.07
CCH	87.316898	$N = 1-0$, $J = 3/2-1/2$, $F = 2-1$	0.019 ± 0.006	227.4 ± 1.1	6.7 ± 2.5	0.15 ± 0.02
CCH	87.328585	$N = 1-0$, $J = 3/2-1/2$, $F = 1-0$				< 0.08
CCH	87.401989	$N = 1-0$, $J = 1/2-1/2$, $F = 1-1$				< 0.08
CCH	87.407165	$N = 1-0$, $J = 1/2-1/2$, $F = 0-1$				< 0.08
CCH	87.446470	$N = 1-0$, $J = 1/2-1/2$, $F = 1-0$				< 0.08
HCN	88.631602	$1-0$	0.032 ± 0.004	227.2 ± 0.7	10.8 ± 1.7	0.26 ± 0.03
HCO^+	89.188525	$1-0$	0.106 ± 0.004	226.96 ± 0.10	5.8 ± 0.3	0.652 ± 0.012
HNC	90.663568	$1-0$	0.040 ± 0.005	229.2 ± 0.3	5.4 ± 0.8	0.231 ± 0.014
N_2H^+	93.173392	$1-0$				< 0.04
CH_3OH	96.741375	$2_0 - 1_0$, A^+				< 0.08
CS	97.980953	$2-1$	0.121 ± 0.009	229.28 ± 0.18	5.1 ± 0.4	0.68 ± 0.02
SO	99.299870	$N_J = 2_3 - 1_2$	0.057 ± 0.009	227.6 ± 0.4	4.4 ± 0.9	0.273 ± 0.018
$C^{18}O$	109.782173	$1-0$				< 0.2
^{13}CO	110.201354	$1-0$	0.91 ± 0.03	230.83 ± 0.07	5.22 ± 0.18	4.95 ± 0.07
CN	113.490970	$N = 1-0$, $J = 3/2-1/2$, $F = 5/2-3/2$				< 0.4
^{12}CO	115.271202	$1-0$	4.45 ± 0.05	230.51 ± 0.03	6.70 ± 0.08	31.30 ± 0.11
(NQC2)						
c-C_3H_2	85.338894	$2_{12} - 1_{01}$				< 0.06
CCH	87.284105	$N = 1-0$, $J = 3/2-1/2$, $F = 1-1$				< 0.09
CCH	87.316898	$N = 1-0$, $J = 3/2-1/2$, $F = 2-1$	0.067 ± 0.013	266.1 ± 0.3	4.5 ± 1.1	0.343 ± 0.020
CCH	87.328585	$N = 1-0$, $J = 3/2-1/2$, $F = 1-0$	0.044 ± 0.009	266.3 ± 0.6	5 [a]	0.23 ± 0.02
CCH	87.401989	$N = 1-0$, $J = 1/2-1/2$, $F = 1-1$	0.047 ± 0.009	266 [a]	4.3 ± 1.0	0.217 ± 0.017
CCH	87.407165	$N = 1-0$, $J = 1/2-1/2$, $F = 0-1$				< 0.08
CCH	87.446470	$N = 1-0$, $J = 1/2-1/2$, $F = 1-0$				< 0.09
HCN	88.631602	$1-0$	0.042 ± 0.004	266.4 ± 0.4	7.5 ± 0.8	0.349 ± 0.014
HCO^+	89.188525	$1-0$	0.141 ± 0.004	266.05 ± 0.08	4.84 ± 0.16	0.724 ± 0.010
HNC	90.663568	$1-0$	0.027 ± 0.005	267.7 ± 0.6	5.8 ± 1.4	0.165 ± 0.017
N_2H^+	93.173392	$1-0$				< 0.05
CH_3OH	96.741375	$2_0 - 1_0$, A^+				< 0.05
CS	97.980953	$2-1$	0.075 ± 0.007	267.65 ± 0.16	4.0 ± 0.5	0.325 ± 0.013
SO	99.299870	$N_J = 2_3 - 1_2$	0.046 ± 0.009	266.3 ± 0.4	4.9 ± 1.1	0.21 ± 0.02
$C^{18}O$	109.782173	$1-0$				< 0.12
^{13}CO	110.201354	$1-0$	0.675 ± 0.014	265.67 ± 0.04	3.61 ± 0.09	2.804 ± 0.016
CN	113.490970	$N = 1-0$, $J = 3/2-1/2$, $F = 5/2-3/2$				< 0.17
^{12}CO	115.271202	$1-0$	2.73 ± 0.03	265.90 ± 0.02	4.68 ± 0.05	13.90 ± 0.04
(N79)						

Table 3.6 (*continued*)

Source/ Molecule	Frequency (GHz)	Transition	$T_{\rm MB}$ Peak (K)	$v_{\rm LSR}$ (km s^{-1})	Δv (km s^{-1})	$\int T_{\rm MB} dv$ (K km s^{-1})
c-C_3H_2	85.338894	$2_{12} - 1_{01}$	0.046 ± 0.008	232.5 ± 0.7	7.4 ± 1.5	0.31 ± 0.04
CCH	87.284105	$N = 1 - 0$, $J = 3/2 - 1/2$, $F = 1 - 1$				< 0.15
CCH	87.316898	$N = 1 - 0$, $J = 3/2 - 1/2$, $F = 2 - 1$	0.152 ± 0.016	231.4 ± 0.3	5.0 ± 0.6	0.78 ± 0.04
CCH	87.328585	$N = 1 - 0$, $J = 3/2 - 1/2$, $F = 1 - 0$				< 0.15
CCH	87.401989	$N = 1 - 0$, $J = 1/2 - 1/2$, $F = 1 - 1$	0.072 ± 0.014	231.5 ± 0.6	6.5 ± 1.4	0.47 ± 0.04
CCH	87.407165	$N = 1 - 0$, $J = 1/2 - 1/2$, $F = 0 - 1$	0.054 ± 0.013	231.1 ± 0.7	5 [a]	0.31 ± 0.03
CCH	87.446470	$N = 1 - 0$, $J = 1/2 - 1/2$, $F = 1 - 0$				< 0.14
HCN	88.631602	$1 - 0$	0.155 ± 0.007	231.6 ± 0.2	9.3 ± 0.5	1.51 ± 0.03
HCO^+	89.188525	$1 - 0$	0.504 ± 0.009	233.28 ± 0.04	5.22 ± 0.11	2.797 ± 0.019
HNC	90.663568	$1 - 0$	0.087 ± 0.012	232 [a]	5.1 ± 0.8	0.45 ± 0.03
N_2H^+	93.173392	$1 - 0$				< 0.10
CH_3OH	96.741375	$2_0 - 1_0$, A^+				< 0.10
CS	97.980953	$2 - 1$	0.157 ± 0.011	233.81 ± 0.19	5.5 ± 0.4	0.95 ± 0.03
SO	99.299870	$N_J = 2_3 - 1_2$	0.055 ± 0.012	231.2 ± 0.8	7.6 ± 1.9	0.46 ± 0.05
$C^{18}O$	109.782173	$1 - 0$				< 0.17
^{13}CO	110.201354	$1 - 0$	0.566 ± 0.017	231.03 ± 0.07	5.02 ± 0.17	3.15 ± 0.03
CN	113.490970	$N = 1 - 0$, $J = 3/2 - 1/2$, $F = 5/2 - 3/2$	0.082 ± 0.017	233.1 ± 0.6	5 [a]	0.45 ± 0.06
^{12}CO	115.271202	$1 - 0$	2.90 ± 0.04	230.99 ± 0.04	5.21 ± 0.09	16.80 ± 0.06
(N44C)						
c-C_3H_2	85.338894	$2_{12} - 1_{01}$	0.035 ± 0.006	283.2 ± 0.5	5.6 ± 1.1	0.21 ± 0.02
CCH	87.284105	$N = 1 - 0$, $J = 3/2 - 1/2$, $F = 1 - 1$				< 0.7
CCH	87.316898	$N = 1 - 0$, $J = 3/2 - 1/2$, $F = 2 - 1$	0.104 ± 0.009	281.3 ± 0.3	6.9 ± 0.7	0.80 ± 0.02
CCH	87.328585	$N = 1 - 0$, $J = 3/2 - 1/2$, $F = 1 - 0$	0.047 ± 0.015	281.8 ± 1.0	6.2 ± 2.3	0.31 ± 0.02
CCH	87.401989	$N = 1 - 0$, $J = 1/2 - 1/2$, $F = 1 - 1$	0.053 ± 0.009	280.4 ± 0.5	5.9 ± 1.1	0.33 ± 0.02
CCH	87.407165	$N = 1 - 0$, $J = 1/2 - 1/2$, $F = 0 - 1$				< 0.10
CCH	87.446470	$N = 1 - 0$, $J = 1/2 - 1/2$, $F = 1 - 0$				< 0.09
HCN	88.631602	$1 - 0$	0.111 ± 0.004	281.36 ± 0.18	9.7 ± 0.4	1.192 ± 0.017
HCO^+	89.188525	$1 - 0$	0.312 ± 0.005	281.29 ± 0.06	6.64 ± 0.13	2.164 ± 0.015
HNC	90.663568	$1 - 0$	0.060 ± 0.005	283.0 ± 0.2	6.1 ± 0.6	0.383 ± 0.013
N_2H^+	93.173392	$1 - 0$				< 0.06
CH_3OH	96.741375	$2_0 - 1_0$, A^+				< 0.06
CS	97.980953	$2 - 1$	0.214 ± 0.006	282.89 ± 0.08	5.70 ± 0.19	1.324 ± 0.015
SO	99.299870	$N_J = 2_3 - 1_2$	0.100 ± 0.012	281.2 ± 0.3	4.7 ± 0.7	0.51 ± 0.03
$C^{18}O$	109.782173	$1 - 0$				< 0.11
^{13}CO	110.201354	$1 - 0$	0.484 ± 0.009	281.41 ± 0.05	5.78 ± 0.12	2.953 ± 0.020
CN	113.490970	$N = 1 - 0$, $J = 3/2 - 1/2$, $F = 5/2 - 3/2$	0.070 ± 0.019	281.6 ± 0.6	4.1 ± 1.3	0.34 ± 0.03
^{12}CO	115.271202	$1 - 0$	3.87 ± 0.02	281.533 ± 0.016	6.23 ± 0.04	25.58 ± 0.05
(N11B)						

Table 3.6 (*continued*)

Source/ Molecule	Frequency (GHz)	Transition	$T_{\rm MB}$ Peak (K)	$v_{\rm LSR}$ (km s^{-1})	Δv (km s^{-1})	$\int T_{\rm MB} dv$ (K km s^{-1})
c-C_3H_2	85.338894	$2_{12} - 1_{01}$	0.025 ± 0.007	287.7 ± 0.9	6.8 ± 2.1	0.19 ± 0.03
CCH	87.284105	$N = 1 - 0$, $J = 3/2 - 1/2$, $F = 1 - 1$				< 1.4
CCH	87.316898	$N = 1 - 0$, $J = 3/2 - 1/2$, $F = 2 - 1$	0.100 ± 0.016	283.9 ± 0.3	4.8 ± 1.0	0.51 ± 0.03
CCH	87.328585	$N = 1 - 0$, $J = 3/2 - 1/2$, $F = 1 - 0$	0.048 ± 0.014	284.5 ± 0.8	5 [a]	0.24 ± 0.03
CCH	87.401989	$N = 1 - 0$, $J = 1/2 - 1/2$, $F = 1 - 1$	0.056 ± 0.012	284.3 ± 0.5	5.4 ± 1.4	0.32 ± 0.03
CCH	87.407165	$N = 1 - 0$, $J = 1/2 - 1/2$, $F = 0 - 1$				< 0.13
CCH	87.446470	$N = 1 - 0$, $J = 1/2 - 1/2$, $F = 1 - 0$				< 0.13
HCN	88.631602	$1 - 0$	0.112 ± 0.007	284.0 ± 0.3	8.9 ± 0.6	1.10 ± 0.02
HCO^+	89.188525	$1 - 0$	0.262 ± 0.007	285.80 ± 0.07	5.76 ± 0.17	1.662 ± 0.016
HNC	90.663568	$1 - 0$	0.085 ± 0.006	285.98 ± 0.19	4.2 ± 0.3	0.385 ± 0.014
N_2H^+	93.173392	$1 - 0$				< 0.07
CH_3OH	96.741375	$2_0 - 1_0$, A^+				< 0.07
CS	97.980953	$2 - 1$	0.241 ± 0.008	285.69 ± 0.07	4.45 ± 0.19	1.151 ± 0.014
SO	99.299870	$N_J = 2_3 - 1_2$	0.069 ± 0.011	284.2 ± 0.3	4.6 ± 0.9	0.36 ± 0.02
$C^{18}O$	109.782173	$1 - 0$				< 0.16
^{13}CO	110.201354	$1 - 0$	0.411 ± 0.013	284.65 ± 0.08	4.61 ± 0.17	2.09 ± 0.03
CN	113.490970	$N = 1 - 0$, $J = 3/2 - 1/2$, $F = 5/2 - 3/2$				< 0.20
^{12}CO	115.271202	$1 - 0$	2.98 ± 0.02	284.63 ± 0.02	5.77 ± 0.05	18.74 ± 0.04
(N113)						
c-C_3H_2	85.338894	$2_{12} - 1_{01}$	0.048 ± 0.015	235.3 ± 1.3	8.7 ± 3.2	0.42 ± 0.08
CCH	87.284105	$N = 1 - 0$, $J = 3/2 - 1/2$, $F = 1 - 1$				< 0.3
CCH	87.401989	$N = 1 - 0$, $J = 1/2 - 1/2$, $F = 1 - 1$	0.10 ± 0.02	234.6 ± 0.8	8.2 ± 1.9	0.91 ± 0.08
CCH	87.407165	$N = 1 - 0$, $J = 1/2 - 1/2$, $F = 0 - 1$				< 0.3
CCH	87.446470	$N = 1 - 0$, $J = 1/2 - 1/2$, $F = 1 - 0$				< 0.2
HCN	88.631602	$1 - 0$	0.328 ± 0.015	234.13 ± 0.19	8.6 ± 0.4	3.15 ± 0.05
HCO^+	89.188525	$1 - 0$	0.760 ± 0.014	234.30 ± 0.05	5.41 ± 0.12	4.29 ± 0.04
HNC	90.663568	$1 - 0$	0.284 ± 0.018	236.11 ± 0.12	4.6 ± 0.4	1.39 ± 0.03
N_2H^+	93.173392	$1 - 0$	0.056 ± 0.009	233.5 ± 1.0	13.6 ± 2.4	0.80 ± 0.07
CH_3OH	96.741375	$2_0 - 1_0$, A^+				< 0.19
CS	97.980953	$2 - 1$	0.560 ± 0.018	236.16 ± 0.08	4.65 ± 0.17	2.73 ± 0.04
SO	99.299870	$N_J = 2_3 - 1_2$	0.21 ± 0.04	234.3 ± 0.4	5.2 ± 1.1	1.15 ± 0.10
$C^{18}O$	109.782173	$1 - 0$				< 0.2
^{13}CO	110.201354	$1 - 0$	1.49 ± 0.02	234.50 ± 0.04	4.38 ± 0.08	7.17 ± 0.04
CN	113.490970	$N = 1 - 0$, $J = 3/2 - 1/2$, $F = 5/2 - 3/2$	0.15 ± 0.04	236.0 ± 0.6	3.9 ± 1.4	0.60 ± 0.08
^{12}CO	115.271202	$1 - 0$	7.95 ± 0.04	234.660 ± 0.015	5.46 ± 0.04	46.96 ± 0.07
(N159W)						
c-C_3H_2	85.338894	$2_{12} - 1_{01}$	0.048 ± 0.010	238.3 ± 0.7	7.4 ± 1.8	0.38 ± 0.04
CCH	87.284105	$N = 1 - 0$, $J = 3/2 - 1/2$, $F = 1 - 1$				< 0.19

Table 3.6 (*continued*)

Source/ Molecule	Frequency (GHz)	Transition	$T_{\rm MB}$ Peak (K)	$v_{\rm LSR}$ (km s^{-1})	Δv (km s^{-1})	$\int T_{\rm MB} dv$ (K km s^{-1})
CCH	87.316898	$N = 1-0$, $J = 3/2-1/2$, $F = 2-1$	0.131 ± 0.017	236.3 ± 0.4	6.7 ± 1.0	0.90 ± 0.05
CCH	87.328585	$N = 1-0$, $J = 3/2-1/2$, $F = 1-0$	0.07 ± 0.02	236.3 ± 0.9	5 [a]	0.36 ± 0.04
CCH	87.401989	$N = 1-0$, $J = 1/2-1/2$, $F = 1-1$	0.083 ± 0.013	235.1 ± 0.5	5 [a]	0.55 ± 0.03
CCH	87.407165	$N = 1-0$, $J = 1/2-1/2$, $F = 0-1$				< 0.19
CCH	87.446470	$N = 1-0$, $J = 1/2-1/2$, $F = 1-0$				< 0.16
HCN	88.631602	$1-0$	0.140 ± 0.007	236.1 ± 0.3	10.5 ± 0.6	1.53 ± 0.04
HCO^+	89.188525	$1-0$	0.469 ± 0.009	237.90 ± 0.07	7.79 ± 0.17	3.87 ± 0.03
HNC	90.663568	$1-0$	0.153 ± 0.011	237.9 ± 0.2	6.3 ± 0.5	1.02 ± 0.04
N_2H^+	93.173392	$1-0$	0.032 ± 0.007	235.7 ± 1.2	10.8 ± 2.9	0.32 ± 0.06
CH_3OH	96.741375	$2_0 - 1_0$, A^+				< 0.13
CS	97.980953	$2-1$	0.391 ± 0.016	237.92 ± 0.12	6.1 ± 0.3	2.54 ± 0.04
SO	99.299870	$N_J = 2_3 - 1_2$	0.134 ± 0.015	236.1 ± 0.4	7.3 ± 1.0	1.02 ± 0.06
$C^{18}O$	109.782173	$1-0$				< 0.9
^{13}CO	110.201354	$1-0$	1.04 ± 0.07	236.6 ± 0.2	7.3 ± 0.6	7.8 ± 0.3
CN	113.490970	$N = 1-0$, $J = 3/2-1/2$, $F = 5/2-3/2$				< 1.4
^{12}CO	115.271202	$1-0$	6.10 ± 0.12	236.71 ± 0.08	8.16 ± 0.18	53.4 ± 0.4

Note. — The errors are 1σ. The upper limits are 3σ.

[a]Assumed.

Table 3.7. Correlation coefficients of integrated intensities of molecules among the seven sources in the LMC.[a]

	CCH	HCN	HCO^+	HNC	CS	SO	^{13}CO
CCH	1.000						
HCN	0.974	1.000					
HCO^+	0.937	0.908	1.000				
HNC	0.901	0.912	0.928	1.000			
CS	0.862	0.845	0.925	0.963	1.000		
SO	0.895	0.870	0.948	0.983	0.985	1.000	
^{13}CO	0.555	0.549	0.691	0.824	0.812	0.845	1.000

[a]The correlation coefficient c is calculated as

$$c = \frac{\sum (x_i - \bar{x})(y_i - \bar{y})}{\sqrt{\sum (x_i - \bar{x})^2 \sum (y_i - \bar{y})^2}}$$

where x_i and y_i are observed integrated intensities for the i-th source. $\bar{x}$ and $\bar{y}$ are the averages of x_i and y_i, respectively. Correlation coefficients are higher than 0.8 except for the pairs including ^{13}CO.

Table 3.8. Derived column densities for CO Peak 1.[a]

	n_{H_2}	3×10^3 cm^{-3}				
molecule	T_k	10 K	20 K	30 K	40 K	50 K
c-C_3H_2 (ortho)		< 1.1(+13)	< 4.5(+12)	< 2.8(+12)	< 2.3(+12)	< 2.2(+12)
CCH		1.1(+14)	5.2(+13)	3.9(+13)	3.2(+13)	2.8(+13)
HCN		4.2(+13)	2.2(+13)	1.7(+13)	1.4(+13)	1.3(+13)
HCO^+		1.2(+13)	6.7(+12)	5.4(+12)	4.7(+12)	4.3(+12)
HNC		1.5(+13)	9.5(+12)	8.3(+12)	7.6(+12)	7.2(+12)
N_2H^+		< 6.7(+11)	< 4.1(+11)	< 3.3(+11)	< 2.9(+11)	< 2.7(+11)
CH_3OH (A)		< 7.7(+12)	< 4.4(+12)	< 3.6(+12)	< 3.2(+12)	< 3.0(+12)
CS		1.1(+14)	5.8(+13)	4.4(+13)	3.7(+13)	3.3(+13)
SO		6.1(+13)	2.9(+13)	2.1(+13)	1.8(+13)	1.6(+13)
$C^{18}O$		< 1.7(+14)	< 1.6(+14)	< 1.6(+14)	< 1.7(+14)	< 1.8(+14)
^{13}CO		4.6(+15)	4.0(+15)	4.1(+15)	4.3(+15)	4.5(+15)
CN		< 3.7(+14)	< 1.6(+14)	< 1.1(+14)	< 8.3(+13)	< 6.8(+13)
^{12}CO		5.4(+16)	3.0(+16)	2.8(+16)	2.8(+16)	2.9(+16)
	n_{H_2}	1×10^4 cm^{-3}				
molecule	T_k	10 K	20 K	30 K	40 K	50 K
c-C_3H_2 (ortho)		< 3.3(+12)	< 1.4(+12)	< 9.0(+11)	< 7.5(+11)	< 7.1(+11)
CCH		3.6(+13)	1.9(+13)	1.5(+13)	1.3(+13)	1.1(+13)
HCN		1.1(+13)	6.3(+12)	5.0(+12)	4.2(+12)	3.8(+12)
HCO^+		3.4(+12)	2.1(+12)	1.8(+12)	1.5(+12)	1.4(+12)
HNC		4.1(+12)	2.8(+12)	2.5(+12)	2.3(+12)	2.2(+12)
N_2H^+		< 2.2(+11)	< 1.4(+11)	< 1.2(+11)	< 1.0(+11)	< 9.6(+10)
CH_3OH (A)		< 3.1(+12)	< 2.0(+12)	< 1.8(+12)	< 1.7(+12)	< 1.6(+12)
CS		2.9(+13)	1.7(+13)	1.3(+13)	1.2(+13)	1.0(+13)
SO		1.9(+13)	9.3(+12)	7.1(+12)	6.1(+12)	5.6(+12)
$C^{18}O$		< 1.7(+14)	< 1.9(+14)	< 2.2(+14)	< 2.5(+14)	< 2.8(+14)
^{13}CO		4.6(+15)	4.9(+15)	5.6(+15)	6.3(+15)	7.0(+15)
CN		< 9.3(+13)	< 4.2(+13)	< 2.9(+13)	< 2.3(+13)	< 1.9(+13)
^{12}CO		4.5(+16)	3.4(+16)	3.6(+16)	3.9(+16)	4.2(+16)
	n_{H_2}	3×10^4 cm^{-3}				
molecule	T_k	10 K	20 K	30 K	40 K	50 K
c-C_3H_2 (ortho)		< 1.2(+12)	< 5.3(+11)	< 3.7(+11)	< 3.2(+11)	< 3.0(+11)
CCH		1.5(+13)	9.4(+12)	8.1(+12)	7.5(+12)	7.1(+12)
HCN		3.8(+12)	2.2(+12)	1.8(+12)	1.5(+12)	1.4(+12)

Table 3.8 (*continued*)

HCO^+		1.4(+12)	9.2(+11)	8.0(+11)	7.3(+11)	6.9(+11)
HNC		1.5(+12)	1.1(+12)	9.4(+11)	8.8(+11)	8.4(+11)
N_2H^+		< 9.3(+10)	< 6.4(+10)	< 5.6(+10)	< 5.1(+10)	< 4.9(+10)
CH_3OH (A)		< 1.9(+12)	< 1.5(+12)	< 1.5(+12)	< 1.5(+12)	< 1.6(+12)
CS		1.1(+13)	6.6(+12)	5.4(+12)	4.9(+12)	4.5(+12)
SO		7.3(+12)	4.1(+12)	3.4(+12)	3.1(+12)	3.0(+12)
$C^{18}O$		< 1.9(+14)	< 2.3(+14)	< 2.8(+14)	< 3.3(+14)	< 3.8(+14)
^{13}CO		4.9(+15)	5.9(+15)	7.2(+15)	8.4(+15)	9.6(+15)
CN		< 2.9(+13)	< 1.4(+13)	< 1.0(+13)	< 8.5(+12)	< 7.3(+12)
^{12}CO		4.5(+16)	3.9(+16)	4.5(+16)	5.1(+16)	5.8(+16)
	n_{H_2}	1×10^5 cm^{-3}				
molecule	T_k	10 K	20 K	30 K	40 K	50 K
c-C_3H_2 (ortho)		< 4.3(+11)	< 2.4(+11)	< 2.0(+11)	< 1.9(+11)	< 1.8(+11)
CCH		8.8(+12)	6.9(+12)	6.8(+12)	6.9(+12)	7.2(+12)
HCN		1.3(+12)	8.1(+11)	6.7(+11)	6.0(+11)	5.5(+11)
HCO^+		7.0(+11)	5.4(+11)	5.1(+11)	4.9(+11)	4.9(+11)
HNC		6.2(+11)	4.7(+11)	4.3(+11)	4.1(+11)	3.9(+11)
N_2H^+		< 5.1(+10)	< 4.0(+10)	< 3.8(+10)	< 3.8(+10)	< 3.8(+10)
CH_3OH (A)		< 1.7(+12)	< 1.7(+12)	< 1.9(+12)	< 2.1(+12)	< 2.2(+12)
CS		4.6(+12)	3.2(+12)	2.8(+12)	2.7(+12)	2.6(+12)
SO		3.7(+12)	2.7(+12)	2.6(+12)	2.7(+12)	2.7(+12)
$C^{18}O$		< 1.9(+14)	< 2.6(+14)	< 3.3(+14)	< 4.0(+14)	< 4.7(+14)
^{13}CO		5.1(+15)	6.5(+15)	8.3(+15)	1.0(+16)	1.2(+16)
CN		< 9.5(+12)	< 5.3(+12)	< 4.1(+12)	< 3.6(+12)	< 3.3(+12)
^{12}CO		4.6(+16)	4.3(+16)	5.1(+16)	6.1(+16)	7.1(+16)

[a] $a(+b)$ refers to $a \times 10^{+b}$ cm^{-2}.

Table 3.9. Derived column densities for NQC2.[a]

	n_{H_2}	3×10^3 cm^{-3}				
molecule	T_k	10 K	20 K	30 K	40 K	50 K
c-C_3H_2 (ortho)		< 1.4(+13)	< 5.4(+12)	< 3.4(+12)	< 2.7(+12)	< 2.6(+12)
CCH		2.6(+14)	1.2(+14)	9.2(+13)	7.6(+13)	6.6(+13)
HCN		6.3(+13)	3.3(+13)	2.5(+13)	2.1(+13)	1.8(+13)
HCO^+		1.4(+13)	7.9(+12)	6.3(+12)	5.3(+12)	4.8(+12)
HNC		9.9(+12)	6.6(+12)	5.7(+12)	5.3(+12)	5.0(+12)
N_2H^+		< 8.4(+11)	< 5.1(+11)	< 4.2(+11)	< 3.6(+11)	< 3.3(+11)
CH_3OH (A)		< 4.8(+12)	< 2.7(+12)	< 2.2(+12)	< 2.0(+12)	< 1.9(+12)
CS		4.7(+13)	2.6(+13)	2.0(+13)	1.7(+13)	1.5(+13)
SO		4.6(+13)	2.2(+13)	1.6(+13)	1.4(+13)	1.2(+13)
$C^{18}O$		< 1.0(+14)	< 9.3(+13)	< 9.7(+13)	< 1.0(+14)	< 1.1(+14)
^{13}CO		2.6(+15)	2.3(+15)	2.3(+15)	2.4(+15)	2.6(+15)
CN		< 1.4(+14)	< 6.0(+13)	< 4.1(+13)	< 3.2(+13)	< 2.6(+13)
^{12}CO		1.7(+16)	1.2(+16)	1.2(+16)	1.2(+16)	1.2(+16)
	n_{H_2}	1×10^4 cm^{-3}				
molecule	T_k	10 K	20 K	30 K	40 K	50 K
c-C_3H_2 (ortho)		< 4.0(+12)	< 1.7(+12)	< 1.1(+12)	< 9.0(+11)	< 8.5(+11)
CCH		8.4(+13)	4.3(+13)	3.4(+13)	2.9(+13)	2.6(+13)
HCN		1.6(+13)	8.8(+12)	6.9(+12)	5.8(+12)	5.1(+12)
HCO^+		3.9(+12)	2.4(+12)	2.0(+12)	1.7(+12)	1.6(+12)
HNC		2.9(+12)	2.0(+12)	1.7(+12)	1.6(+12)	1.5(+12)
N_2H^+		< 2.7(+11)	< 1.7(+11)	< 1.5(+11)	< 1.3(+11)	< 1.2(+11)
CH_3OH (A)		< 1.9(+12)	< 1.3(+12)	< 1.1(+12)	< 1.1(+12)	< 1.0(+12)
CS		1.3(+13)	7.9(+12)	6.3(+12)	5.5(+12)	4.9(+12)
SO		1.4(+13)	7.1(+12)	5.4(+12)	4.7(+12)	4.3(+12)
$C^{18}O$		< 1.0(+14)	< 1.2(+14)	< 1.3(+14)	< 1.5(+14)	< 1.7(+14)
^{13}CO		2.6(+15)	2.8(+15)	3.2(+15)	3.6(+15)	4.0(+15)
CN		< 3.5(+13)	< 1.7(+13)	< 1.2(+13)	< 9.5(+12)	< 8.1(+12)
^{12}CO		1.5(+16)	1.4(+16)	1.5(+16)	1.7(+16)	1.8(+16)
	n_{H_2}	3×10^4 cm^{-3}				
molecule	T_k	10 K	20 K	30 K	40 K	50 K
c-C_3H_2 (ortho)		< 1.4(+12)	< 6.3(+11)	< 4.4(+11)	< 3.8(+11)	< 3.7(+11)
CCH		3.6(+13)	2.2(+13)	1.9(+13)	1.7(+13)	1.6(+13)
HCN		5.1(+12)	3.0(+12)	2.4(+12)	2.0(+12)	1.8(+12)

Table 3.9 (*continued*)

HCO^+		1.5(+12)	1.0(+12)	8.9(+11)	8.1(+11)	7.7(+11)
HNC		1.1(+12)	7.5(+11)	6.7(+11)	6.3(+11)	6.0(+11)
N_2H^+		< 1.2(+11)	< 8.0(+10)	< 7.0(+10)	< 6.4(+10)	< 6.1(+10)
CH_3OH (A)		< 1.2(+12)	< 9.6(+11)	< 9.5(+11)	< 9.6(+11)	< 9.8(+11)
CS		5.0(+12)	3.1(+12)	2.6(+12)	2.3(+12)	2.1(+12)
SO		5.6(+12)	3.2(+12)	2.6(+12)	2.4(+12)	2.3(+12)
$C^{18}O$		< 1.1(+14)	< 1.4(+14)	< 1.7(+14)	< 2.0(+14)	< 2.3(+14)
^{13}CO		2.8(+15)	3.3(+15)	4.0(+15)	4.7(+15)	5.4(+15)
CN		< 1.2(+13)	< 5.9(+12)	< 4.3(+12)	< 3.5(+12)	< 3.1(+12)
^{12}CO		1.6(+16)	1.6(+16)	1.9(+16)	2.2(+16)	2.5(+16)
	n_{H_2}	1×10^5 cm^{-3}				
molecule	T_k	10 K	20 K	30 K	40 K	50 K
c-C_3H_2 (ortho)		< 5.1(+11)	< 2.8(+11)	< 2.3(+11)	< 2.2(+11)	< 2.2(+11)
CCH		2.0(+13)	1.6(+13)	1.5(+13)	1.6(+13)	1.6(+13)
HCN		1.7(+12)	1.1(+12)	9.1(+11)	8.1(+11)	7.4(+11)
HCO^+		7.8(+11)	6.1(+11)	5.7(+11)	5.5(+11)	5.5(+11)
HNC		4.4(+11)	3.3(+11)	3.0(+11)	2.9(+11)	2.8(+11)
N_2H^+		< 6.3(+10)	< 5.0(+10)	< 4.7(+10)	< 4.7(+10)	< 4.7(+10)
CH_3OH (A)		< 1.1(+12)	< 1.1(+12)	< 1.2(+12)	< 1.3(+12)	< 1.4(+12)
CS		2.2(+12)	1.5(+12)	1.4(+12)	1.3(+12)	1.2(+12)
SO		2.8(+12)	2.1(+12)	2.0(+12)	2.1(+12)	2.1(+12)
$C^{18}O$		< 1.2(+14)	< 1.5(+14)	< 2.0(+14)	< 2.4(+14)	< 2.8(+14)
^{13}CO		2.9(+15)	3.7(+15)	4.7(+15)	5.6(+15)	6.6(+15)
CN		< 3.9(+12)	< 2.2(+12)	< 1.8(+12)	< 1.5(+12)	< 1.4(+12)
^{12}CO		1.6(+16)	1.8(+16)	2.2(+16)	2.6(+16)	3.1(+16)

[a] $a(+b)$ refers to $a \times 10^{+b}$ cm^{-2}.

Table 3.10. Derived column densities for N79.[a]

	n_{H_2}	3×10^3 cm^{-3}				
molecule	T_k	10 K	20 K	30 K	40 K	50 K
c-C_3H_2 (ortho)		8.3(+13)	3.0(+13)	1.8(+13)	1.5(+13)	1.4(+13)
CCH		6.8(+14)	2.9(+14)	2.2(+14)	1.8(+14)	1.6(+14)
HCN		3.2(+14)	1.8(+14)	1.4(+14)	1.1(+14)	9.8(+13)
HCO^+		7.5(+13)	4.2(+13)	3.2(+13)	2.7(+13)	2.4(+13)
HNC		3.3(+13)	2.1(+13)	1.8(+13)	1.6(+13)	1.5(+13)
N_2H^+		< 1.7(+12)	< 1.0(+12)	< 8.4(+11)	< 7.3(+11)	< 6.7(+11)
CH_3OH (A)		< 9.6(+12)	< 5.5(+12)	< 4.5(+12)	< 4.0(+12)	< 3.8(+12)
CS		1.6(+14)	8.4(+13)	6.4(+13)	5.4(+13)	4.8(+13)
SO		1.0(+14)	4.8(+13)	3.6(+13)	3.0(+13)	2.7(+13)
$C^{18}O$		< 1.4(+14)	< 1.3(+14)	< 1.4(+14)	< 1.4(+14)	< 1.5(+14)
^{13}CO		2.8(+15)	2.5(+15)	2.6(+15)	2.7(+15)	2.9(+15)
CN		4.3(+14)	1.9(+14)	1.3(+14)	9.5(+13)	7.8(+13)
^{12}CO		2.1(+16)	1.5(+16)	1.4(+16)	1.4(+16)	1.5(+16)
	n_{H_2}	1×10^4 cm^{-3}				
molecule	T_k	10 K	20 K	30 K	40 K	50 K
c-C_3H_2 (ortho)		2.2(+13)	8.8(+12)	5.6(+12)	4.7(+12)	4.5(+12)
CCH		2.0(+14)	1.0(+14)	7.9(+13)	6.8(+13)	6.1(+13)
HCN		8.7(+13)	4.5(+13)	3.4(+13)	2.8(+13)	2.5(+13)
HCO^+		2.0(+13)	1.1(+13)	8.7(+12)	7.6(+12)	6.9(+12)
HNC		8.5(+12)	5.7(+12)	5.0(+12)	4.6(+12)	4.4(+12)
N_2H^+		< 5.6(+11)	< 3.5(+11)	< 2.9(+11)	< 2.6(+11)	< 2.4(+11)
CH_3OH (A)		< 3.9(+12)	< 2.5(+12)	< 2.2(+12)	< 2.1(+12)	< 2.0(+12)
CS		4.2(+13)	2.4(+13)	1.9(+13)	1.6(+13)	1.5(+13)
SO		3.1(+13)	1.6(+13)	1.2(+13)	1.0(+13)	9.4(+12)
$C^{18}O$		< 1.5(+14)	< 1.6(+14)	< 1.9(+14)	< 2.1(+14)	< 2.4(+14)
^{13}CO		2.9(+15)	3.1(+15)	3.5(+15)	4.0(+15)	4.4(+15)
CN		1.1(+14)	4.8(+13)	3.3(+13)	2.6(+13)	2.2(+13)
^{12}CO		1.9(+16)	1.7(+16)	1.8(+16)	2.0(+16)	2.2(+16)
	n_{H_2}	3×10^4 cm^{-3}				
molecule	T_k	10 K	20 K	30 K	40 K	50 K
c-C_3H_2 (ortho)		7.4(+12)	3.3(+12)	2.3(+12)	2.0(+12)	1.9(+12)
CCH		8.3(+13)	5.0(+13)	4.3(+13)	3.9(+13)	3.7(+13)
HCN		2.5(+13)	1.4(+13)	1.1(+13)	9.3(+12)	8.3(+12)

Table 3.10 (*continued*)

HCO^+		6.7(+12)	4.2(+12)	3.6(+12)	3.3(+12)	3.1(+12)
HNC		3.0(+12)	2.1(+12)	1.9(+12)	1.7(+12)	1.6(+12)
N_2H^+		< 2.3(+11)	< 1.6(+11)	< 1.4(+11)	< 1.3(+11)	< 1.2(+11)
CH_3OH (A)		< 2.4(+12)	< 1.9(+12)	< 1.9(+12)	< 1.9(+12)	< 2.0(+12)
CS		1.5(+13)	9.3(+12)	7.6(+12)	6.8(+12)	6.2(+12)
SO		1.2(+13)	6.9(+12)	5.8(+12)	5.3(+12)	5.0(+12)
$C^{18}O$		< 1.6(+14)	< 2.0(+14)	< 2.4(+14)	< 2.8(+14)	< 3.2(+14)
^{13}CO		3.1(+15)	3.7(+15)	4.5(+15)	5.3(+15)	6.1(+15)
CN		3.2(+13)	1.6(+13)	1.2(+13)	9.6(+12)	8.2(+12)
^{12}CO		2.0(+16)	2.0(+16)	2.3(+16)	2.7(+16)	3.0(+16)
	n_{H_2}	1×10^5 cm^{-3}				
molecule	T_k	10 K	20 K	30 K	40 K	50 K
c-C_3H_2 (ortho)		2.7(+12)	1.5(+12)	1.2(+12)	1.2(+12)	1.1(+12)
CCH		4.7(+13)	3.6(+13)	3.5(+13)	3.6(+13)	3.7(+13)
HCN		7.9(+12)	4.9(+12)	4.0(+12)	3.6(+12)	3.3(+12)
HCO^+		3.2(+12)	2.4(+12)	2.2(+12)	2.2(+12)	2.1(+12)
HNC		1.2(+12)	9.1(+11)	8.3(+11)	7.9(+11)	7.6(+11)
N_2H^+		< 1.3(+11)	< 1.0(+11)	< 9.6(+10)	< 9.4(+10)	< 9.4(+10)
CH_3OH (A)		< 2.1(+12)	< 2.1(+12)	< 2.3(+12)	< 2.6(+12)	< 2.8(+12)
CS		6.5(+12)	4.5(+12)	4.0(+12)	3.7(+12)	3.6(+12)
SO		6.2(+12)	4.6(+12)	4.4(+12)	4.5(+12)	4.6(+12)
$C^{18}O$		< 1.6(+14)	< 2.2(+14)	< 2.8(+14)	< 3.4(+14)	< 4.0(+14)
^{13}CO		3.2(+15)	4.1(+15)	5.2(+15)	6.3(+15)	7.3(+15)
CN		1.1(+13)	6.0(+12)	4.7(+12)	4.0(+12)	3.7(+12)
^{12}CO		2.0(+16)	2.2(+16)	2.7(+16)	3.2(+16)	3.7(+16)

[a] $a(+b)$ refers to $a \times 10^{+b}$ cm^{-2}.

Table 3.11. Derived column densities for N44C.[a]

	n_{H_2}	3×10^3 cm^{-3}				
molecule	T_k	10 K	20 K	30 K	40 K	50 K
c-C_3H_2 (ortho)		5.5(+13)	2.0(+13)	1.2(+13)	1.0(+13)	9.4(+12)
CCH		6.6(+14)	2.9(+14)	2.2(+14)	1.8(+14)	1.6(+14)
HCN		2.4(+14)	1.3(+14)	1.0(+14)	8.5(+13)	7.3(+13)
HCO^+		5.1(+13)	2.8(+13)	2.2(+13)	1.8(+13)	1.6(+13)
HNC		2.6(+13)	1.7(+13)	1.4(+13)	1.3(+13)	1.2(+13)
N_2H^+		< 1.0(+12)	< 6.2(+11)	< 5.1(+11)	< 4.4(+11)	< 4.0(+11)
CH_3OH (A)		< 5.8(+12)	< 3.3(+12)	< 2.7(+12)	< 2.4(+12)	< 2.3(+12)
CS		2.4(+14)	1.2(+14)	9.4(+13)	7.9(+13)	6.9(+13)
SO		1.2(+14)	5.5(+13)	4.0(+13)	3.4(+13)	3.0(+13)
$C^{18}O$		< 9.3(+13)	< 8.5(+13)	< 8.9(+13)	< 9.3(+13)	< 9.8(+13)
^{13}CO		2.6(+15)	2.4(+15)	2.4(+15)	2.5(+15)	2.7(+15)
CN		3.2(+14)	1.4(+14)	9.3(+13)	7.1(+13)	5.8(+13)
^{12}CO		3.9(+16)	2.3(+16)	2.2(+16)	2.3(+16)	2.3(+16)
	n_{H_2}	1×10^4 cm^{-3}				
molecule	T_k	10 K	20 K	30 K	40 K	50 K
c-C_3H_2 (ortho)		1.5(+13)	6.0(+12)	3.8(+12)	3.2(+12)	3.0(+12)
CCH		2.0(+14)	1.0(+14)	8.0(+13)	6.9(+13)	6.2(+13)
HCN		6.4(+13)	3.4(+13)	2.6(+13)	2.2(+13)	1.9(+13)
HCO^+		1.3(+13)	7.7(+12)	6.2(+12)	5.4(+12)	5.0(+12)
HNC		7.0(+12)	4.8(+12)	4.2(+12)	3.9(+12)	3.7(+12)
N_2H^+		< 3.3(+11)	< 2.1(+11)	< 1.7(+11)	< 1.5(+11)	< 1.4(+11)
CH_3OH (A)		< 2.3(+12)	< 1.5(+12)	< 1.3(+12)	< 1.3(+12)	< 1.2(+12)
CS		6.1(+13)	3.4(+13)	2.7(+13)	2.3(+13)	2.1(+13)
SO		3.5(+13)	1.8(+13)	1.3(+13)	1.2(+13)	1.1(+13)
$C^{18}O$		< 9.5(+13)	< 1.1(+14)	< 1.2(+14)	< 1.4(+14)	< 1.5(+14)
^{13}CO		2.7(+15)	2.9(+15)	3.3(+15)	3.7(+15)	4.1(+15)
CN		7.9(+13)	3.6(+13)	2.5(+13)	2.0(+13)	1.7(+13)
^{12}CO		3.3(+16)	2.7(+16)	2.9(+16)	3.1(+16)	3.4(+16)
	n_{H_2}	3×10^4 cm^{-3}				
molecule	T_k	10 K	20 K	30 K	40 K	50 K
c-C_3H_2 (ortho)		5.0(+12)	2.2(+12)	1.5(+12)	1.3(+12)	1.3(+12)
CCH		8.5(+13)	5.1(+13)	4.3(+13)	4.0(+13)	3.8(+13)
HCN		1.9(+13)	1.1(+13)	8.5(+12)	7.3(+12)	6.5(+12)

Table 3.11 (*continued*)

HCO^+		4.8(+12)	3.2(+12)	2.7(+12)	2.5(+12)	2.3(+12)
HNC		2.5(+12)	1.7(+12)	1.6(+12)	1.5(+12)	1.4(+12)
N_2H^+		< 1.4(+11)	< 9.6(+10)	< 8.4(+10)	< 7.7(+10)	< 7.3(+10)
CH_3OH (A)		< 1.4(+12)	< 1.2(+12)	< 1.1(+12)	< 1.2(+12)	< 1.2(+12)
CS		2.1(+13)	1.3(+13)	1.1(+13)	9.6(+12)	8.8(+12)
SO		1.4(+13)	7.8(+12)	6.4(+12)	5.9(+12)	5.6(+12)
$C^{18}O$		< 1.0(+14)	< 1.3(+14)	< 1.6(+14)	< 1.8(+14)	< 2.1(+14)
^{13}CO		2.8(+15)	3.5(+15)	4.2(+15)	4.9(+15)	5.6(+15)
CN		2.4(+13)	1.2(+13)	8.8(+12)	7.2(+12)	6.2(+12)
^{12}CO		3.4(+16)	3.1(+16)	3.6(+16)	4.2(+16)	4.7(+16)
	n_{H_2}	1×10^5 cm^{-3}				
molecule	T_k	10 K	20 K	30 K	40 K	50 K
c-C_3H_2 (ortho)		1.8(+12)	9.9(+11)	8.2(+11)	7.9(+11)	7.8(+11)
CCH		4.8(+13)	3.7(+13)	3.6(+13)	3.7(+13)	3.8(+13)
HCN		6.1(+12)	3.8(+12)	3.1(+12)	2.8(+12)	2.6(+12)
HCO^+		2.4(+12)	1.8(+12)	1.7(+12)	1.6(+12)	1.6(+12)
HNC		1.0(+12)	7.7(+11)	7.1(+11)	6.7(+11)	6.5(+11)
N_2H^+		< 7.6(+10)	< 6.0(+10)	< 5.7(+10)	< 5.7(+10)	< 5.7(+10)
CH_3OH (A)		< 1.3(+12)	< 1.3(+12)	< 1.4(+12)	< 1.6(+12)	< 1.7(+12)
CS		9.2(+12)	6.3(+12)	5.6(+12)	5.3(+12)	5.1(+12)
SO		7.0(+12)	5.1(+12)	4.9(+12)	5.0(+12)	5.1(+12)
$C^{18}O$		< 1.1(+14)	< 1.4(+14)	< 1.8(+14)	< 2.2(+14)	< 2.6(+14)
^{13}CO		3.0(+15)	3.8(+15)	4.9(+15)	5.9(+15)	6.9(+15)
CN		8.1(+12)	4.5(+12)	3.5(+12)	3.1(+12)	2.8(+12)
^{12}CO		3.5(+16)	3.4(+16)	4.2(+16)	4.9(+16)	5.7(+16)

[a] $a(+b)$ refers to $a \times 10^{+b}$ cm^{-2}.

Table 3.12. Derived column densities for N11B.[a]

	n_{H_2}	3×10^3 cm^{-3}				
molecule	T_k	10 K	20 K	30 K	40 K	50 K
c-C_3H_2 (ortho)		4.7(+13)	1.8(+13)	1.1(+13)	8.9(+12)	8.4(+12)
CCH		4.1(+14)	1.9(+14)	1.4(+14)	1.1(+14)	1.0(+14)
HCN		2.3(+14)	1.2(+14)	9.4(+13)	7.8(+13)	6.8(+13)
HCO^+		3.8(+13)	2.1(+13)	1.6(+13)	1.4(+13)	1.2(+13)
HNC		2.8(+13)	1.8(+13)	1.5(+13)	1.4(+13)	1.3(+13)
N_2H^+		< 1.2(+12)	< 7.2(+11)	< 5.9(+11)	< 5.1(+11)	< 4.7(+11)
CH_3OH (A)		< 6.8(+12)	< 3.8(+12)	< 3.1(+12)	< 2.8(+12)	< 2.6(+12)
CS		2.1(+14)	1.1(+14)	8.4(+13)	7.0(+13)	6.1(+13)
SO		8.1(+13)	3.8(+13)	2.8(+13)	2.4(+13)	2.1(+13)
$C^{18}O$		< 1.4(+14)	< 1.2(+14)	< 1.3(+14)	< 1.4(+14)	< 1.4(+14)
^{13}CO		1.9(+15)	1.7(+15)	1.7(+15)	1.8(+15)	1.9(+15)
CN		< 1.7(+14)	< 7.2(+13)	< 4.9(+13)	< 3.8(+13)	< 3.1(+13)
^{12}CO		2.4(+16)	1.6(+16)	1.6(+16)	1.6(+16)	1.6(+16)
	n_{H_2}	1×10^4 cm^{-3}				
molecule	T_k	10 K	20 K	30 K	40 K	50 K
c-C_3H_2 (ortho)		1.3(+13)	5.4(+12)	3.4(+12)	2.9(+12)	2.7(+12)
CCH		1.3(+14)	6.5(+13)	5.1(+13)	4.4(+13)	4.0(+13)
HCN		5.9(+13)	3.1(+13)	2.4(+13)	2.0(+13)	1.7(+13)
HCO^+		9.9(+12)	5.8(+12)	4.7(+12)	4.1(+12)	3.8(+12)
HNC		7.3(+12)	4.9(+12)	4.3(+12)	4.0(+12)	3.7(+12)
N_2H^+		< 3.8(+11)	< 2.4(+11)	< 2.0(+11)	< 1.8(+11)	< 1.7(+11)
CH_3OH (A)		< 2.7(+12)	< 1.8(+12)	< 1.6(+12)	< 1.5(+12)	< 1.4(+12)
CS		5.4(+13)	3.0(+13)	2.4(+13)	2.0(+13)	1.8(+13)
SO		2.5(+13)	1.2(+13)	9.4(+12)	8.2(+12)	7.4(+12)
$C^{18}O$		< 1.4(+14)	< 1.5(+14)	< 1.8(+14)	< 2.0(+14)	< 2.2(+14)
^{13}CO		1.9(+15)	2.0(+15)	2.3(+15)	2.6(+15)	2.9(+15)
CN		< 4.2(+13)	< 2.0(+13)	< 1.4(+13)	< 1.1(+13)	< 9.5(+12)
^{12}CO		2.1(+16)	1.9(+16)	2.0(+16)	2.3(+16)	2.5(+16)
	n_{H_2}	3×10^4 cm^{-3}				
molecule	T_k	10 K	20 K	30 K	40 K	50 K
c-C_3H_2 (ortho)		4.5(+12)	2.0(+12)	1.4(+12)	1.2(+12)	1.2(+12)
CCH		5.4(+13)	3.2(+13)	2.8(+13)	2.5(+13)	2.4(+13)
HCN		1.8(+13)	9.9(+12)	7.8(+12)	6.7(+12)	6.0(+12)

Table 3.12 (*continued*)

HCO^+		3.7(+12)	2.4(+12)	2.1(+12)	1.9(+12)	1.8(+12)
HNC		2.6(+12)	1.8(+12)	1.6(+12)	1.5(+12)	1.4(+12)
N_2H^+		< 1.6(+11)	< 1.1(+11)	< 9.7(+10)	< 9.0(+10)	< 8.6(+10)
CH_3OH (A)		< 1.7(+12)	< 1.3(+12)	< 1.3(+12)	< 1.3(+12)	< 1.4(+12)
CS		1.9(+13)	1.1(+13)	9.4(+12)	8.4(+12)	7.7(+12)
SO		9.7(+12)	5.4(+12)	4.5(+12)	4.2(+12)	4.0(+12)
$C^{18}O$		< 1.5(+14)	< 1.8(+14)	< 2.3(+14)	< 2.7(+14)	< 3.0(+14)
^{13}CO		2.0(+15)	2.4(+15)	3.0(+15)	3.5(+15)	4.0(+15)
CN		< 1.4(+13)	< 7.0(+12)	< 5.1(+12)	< 4.2(+12)	< 3.6(+12)
^{12}CO		2.2(+16)	2.2(+16)	2.6(+16)	3.0(+16)	3.4(+16)
	n_{H_2}	1×10^5 cm^{-3}				
molecule	T_k	10 K	20 K	30 K	40 K	50 K
c-C_3H_2 (ortho)		1.6(+12)	8.9(+11)	7.4(+11)	7.1(+11)	7.0(+11)
CCH		3.0(+13)	2.3(+13)	2.3(+13)	2.4(+13)	2.4(+13)
HCN		5.7(+12)	3.5(+12)	2.9(+12)	2.6(+12)	2.4(+12)
HCO^+		1.8(+12)	1.4(+12)	1.3(+12)	1.3(+12)	1.2(+12)
HNC		1.0(+12)	7.8(+11)	7.1(+11)	6.8(+11)	6.6(+11)
N_2H^+		< 8.9(+10)	< 7.0(+10)	< 6.6(+10)	< 6.6(+10)	< 6.6(+10)
CH_3OH (A)		< 1.5(+12)	< 1.5(+12)	< 1.6(+12)	< 1.8(+12)	< 2.0(+12)
CS		8.0(+12)	5.5(+12)	4.9(+12)	4.6(+12)	4.4(+12)
SO		4.9(+12)	3.6(+12)	3.5(+12)	3.5(+12)	3.6(+12)
$C^{18}O$		< 1.6(+14)	< 2.0(+14)	< 2.6(+14)	< 3.2(+14)	< 3.7(+14)
^{13}CO		2.1(+15)	2.7(+15)	3.4(+15)	4.2(+15)	4.9(+15)
CN		< 4.7(+12)	< 2.6(+12)	< 2.1(+12)	< 1.8(+12)	< 1.6(+12)
^{12}CO		2.3(+16)	2.4(+16)	3.0(+16)	3.6(+16)	4.2(+16)

[a] $a(+b)$ refers to $a \times 10^{+b}$ cm^{-2}.

Table 3.13. Derived column densities for N113.[a]

	n_{H_2}	3×10^3 cm^{-3}				
molecule	T_k	10 K	20 K	30 K	40 K	50 K
c-C_3H_2 (ortho)		1.2(+14)	4.1(+13)	2.5(+13)	2.0(+13)	1.9(+13)
CCH		1.5(+15)	8.4(+14)	6.3(+14)	5.1(+14)	4.3(+14)
HCN		7.2(+14)	4.0(+14)	3.1(+14)	2.6(+14)	2.3(+14)
HCO^+		1.3(+14)	7.1(+13)	5.6(+13)	4.7(+13)	4.2(+13)
HNC		1.3(+14)	8.2(+13)	7.1(+13)	6.6(+13)	6.2(+13)
N_2H^+		1.4(+13)	8.5(+12)	6.9(+12)	6.0(+12)	5.5(+12)
CH_3OH (A)		< 1.9(+13)	< 1.0(+13)	< 8.5(+12)	< 7.6(+12)	< 7.1(+12)
CS		5.8(+14)	3.2(+14)	2.4(+14)	2.0(+14)	1.8(+14)
SO		3.0(+14)	1.3(+14)	9.4(+13)	7.9(+13)	7.1(+13)
$C^{18}O$		< 1.7(+14)	< 1.6(+14)	< 1.6(+14)	< 1.7(+14)	< 1.8(+14)
^{13}CO		7.3(+15)	6.0(+15)	6.1(+15)	6.4(+15)	6.7(+15)
CN		6.0(+14)	2.8(+14)	1.9(+14)	1.4(+14)	1.1(+14)
^{12}CO		3.9(+25)	6.1(+16)	5.0(+16)	4.8(+16)	4.8(+16)
	n_{H_2}	1×10^4 cm^{-3}				
molecule	T_k	10 K	20 K	30 K	40 K	50 K
c-C_3H_2 (ortho)		3.0(+13)	1.2(+13)	7.7(+12)	6.4(+12)	6.1(+12)
CCH		4.5(+14)	2.8(+14)	2.2(+14)	1.9(+14)	1.7(+14)
HCN		2.1(+14)	1.1(+14)	8.6(+13)	7.1(+13)	6.2(+13)
HCO^+		3.5(+13)	1.9(+13)	1.5(+13)	1.2(+13)	1.1(+13)
HNC		3.4(+13)	2.1(+13)	1.8(+13)	1.7(+13)	1.6(+13)
N_2H^+		4.5(+12)	2.8(+12)	2.3(+12)	2.1(+12)	1.9(+12)
CH_3OH (A)		< 7.4(+12)	< 4.8(+12)	< 4.2(+12)	< 4.0(+12)	< 3.9(+12)
CS		1.6(+14)	8.3(+13)	6.3(+13)	5.4(+13)	4.8(+13)
SO		8.3(+13)	4.0(+13)	3.1(+13)	2.7(+13)	2.4(+13)
$C^{18}O$		< 1.7(+14)	< 1.9(+14)	< 2.2(+14)	< 2.5(+14)	< 2.8(+14)
^{13}CO		7.2(+15)	7.3(+15)	8.3(+15)	9.3(+15)	1.0(+16)
CN		1.6(+14)	7.0(+13)	4.7(+13)	3.7(+13)	3.0(+13)
^{12}CO		2.3(+25)	6.3(+16)	6.1(+16)	6.4(+16)	6.9(+16)
	n_{H_2}	3×10^4 cm^{-3}				
molecule	T_k	10 K	20 K	30 K	40 K	50 K
c-C_3H_2 (ortho)		1.0(+13)	4.5(+12)	3.1(+12)	2.7(+12)	2.6(+12)
CCH		2.0(+14)	1.4(+14)	1.2(+14)	1.0(+14)	9.7(+13)
HCN		6.3(+13)	3.3(+13)	2.5(+13)	2.1(+13)	1.9(+13)

Table 3.13 (*continued*)

HCO^+		1.1(+13)	6.9(+12)	5.7(+12)	5.2(+12)	4.9(+12)
HNC		1.0(+13)	7.0(+12)	6.1(+12)	5.7(+12)	5.4(+12)
N_2H^+		1.9(+12)	1.3(+12)	1.1(+12)	1.0(+12)	9.8(+11)
CH_3OH (A)		< 4.6(+12)	< 3.6(+12)	< 3.6(+12)	< 3.7(+12)	< 3.7(+12)
CS		5.0(+13)	2.9(+13)	2.3(+13)	2.1(+13)	1.9(+13)
SO		3.2(+13)	1.8(+13)	1.5(+13)	1.3(+13)	1.3(+13)
$C^{18}O$		< 1.9(+14)	< 2.3(+14)	< 2.8(+14)	< 3.3(+14)	< 3.8(+14)
^{13}CO		7.6(+15)	8.7(+15)	1.1(+16)	1.2(+16)	1.4(+16)
CN		4.6(+13)	2.2(+13)	1.6(+13)	1.3(+13)	1.1(+13)
^{12}CO		2.0(+25)	7.1(+16)	7.5(+16)	8.4(+16)	9.3(+16)
	n_{H_2}	1×10^5 cm^{-3}				
molecule	T_k	10 K	20 K	30 K	40 K	50 K
c-C_3H_2 (ortho)		3.6(+12)	2.0(+12)	1.6(+12)	1.6(+12)	1.5(+12)
CCH		1.1(+14)	9.4(+13)	9.0(+13)	9.0(+13)	9.2(+13)
HCN		1.8(+13)	1.1(+13)	8.7(+12)	7.7(+12)	7.0(+12)
HCO^+		5.1(+12)	3.7(+12)	3.5(+12)	3.3(+12)	3.3(+12)
HNC		4.0(+12)	2.9(+12)	2.6(+12)	2.5(+12)	2.4(+12)
N_2H^+		1.0(+12)	8.1(+11)	7.6(+11)	7.5(+11)	7.5(+11)
CH_3OH (A)		< 4.0(+12)	< 4.0(+12)	< 4.5(+12)	< 4.9(+12)	< 5.3(+12)
CS		2.0(+13)	1.3(+13)	1.2(+13)	1.1(+13)	1.1(+13)
SO		1.6(+13)	1.2(+13)	1.1(+13)	1.1(+13)	1.1(+13)
$C^{18}O$		< 1.9(+14)	< 2.6(+14)	< 3.3(+14)	< 4.0(+14)	< 4.7(+14)
^{13}CO		7.9(+15)	9.6(+15)	1.2(+16)	1.5(+16)	1.7(+16)
CN		1.5(+13)	8.1(+12)	6.3(+12)	5.5(+12)	5.0(+12)
^{12}CO		1.9(+25)	7.7(+16)	8.5(+16)	9.9(+16)	1.1(+17)

[a] $a(+b)$ refers to $a \times 10^{+b}$ cm^{-2}.

Table 3.14. Derived column densities for N159W.[a]

	n_{H_2}	3×10^3 cm^{-3}				
molecule	T_k	10 K	20 K	30 K	40 K	50 K
c-C_3H_2 (ortho)		1.1(+14)	3.8(+13)	2.3(+13)	1.8(+13)	1.7(+13)
CCH		7.6(+14)	3.3(+14)	2.5(+14)	2.0(+14)	1.8(+14)
HCN		3.2(+14)	1.8(+14)	1.3(+14)	1.1(+14)	9.7(+13)
HCO^+		1.0(+14)	5.6(+13)	4.4(+13)	3.7(+13)	3.3(+13)
HNC		8.4(+13)	5.4(+13)	4.6(+13)	4.2(+13)	3.9(+13)
N_2H^+		5.5(+12)	3.3(+12)	2.7(+12)	2.4(+12)	2.1(+12)
CH_3OH (A)		< 1.3(+13)	< 7.1(+12)	< 5.8(+12)	< 5.2(+12)	< 4.9(+12)
CS		5.1(+14)	2.8(+14)	2.1(+14)	1.7(+14)	1.5(+14)
SO		2.5(+14)	1.1(+14)	8.1(+13)	6.8(+13)	6.1(+13)
$C^{18}O$		< 7.8(+14)	< 7.0(+14)	< 7.2(+14)	< 7.6(+14)	< 8.0(+14)
^{13}CO		7.4(+15)	6.4(+15)	6.5(+15)	6.8(+15)	7.1(+15)
CN		< 1.5(+15)	< 7.0(+14)	< 4.8(+14)	< 3.7(+14)	< 3.0(+14)
^{12}CO		3.3(+17)	5.8(+16)	5.2(+16)	5.1(+16)	5.1(+16)
	n_{H_2}	1×10^4 cm^{-3}				
molecule	T_k	10 K	20 K	30 K	40 K	50 K
c-C_3H_2 (ortho)		2.7(+13)	1.1(+13)	7.0(+12)	5.8(+12)	5.5(+12)
CCH		2.3(+14)	1.2(+14)	9.0(+13)	7.8(+13)	7.0(+13)
HCN		8.6(+13)	4.5(+13)	3.4(+13)	2.8(+13)	2.5(+13)
HCO^+		2.7(+13)	1.5(+13)	1.2(+13)	1.0(+13)	9.5(+12)
HNC		2.1(+13)	1.4(+13)	1.2(+13)	1.1(+13)	1.0(+13)
N_2H^+		1.8(+12)	1.1(+12)	9.4(+11)	8.3(+11)	7.7(+11)
CH_3OH (A)		< 5.1(+12)	< 3.3(+12)	< 2.9(+12)	< 2.7(+12)	< 2.6(+12)
CS		1.3(+14)	7.2(+13)	5.6(+13)	4.8(+13)	4.2(+13)
SO		7.2(+13)	3.5(+13)	2.7(+13)	2.3(+13)	2.1(+13)
$C^{18}O$		< 7.9(+14)	< 8.6(+14)	< 1.0(+15)	< 1.1(+15)	< 1.3(+15)
^{13}CO		7.3(+15)	7.8(+15)	8.9(+15)	1.0(+16)	1.1(+16)
CN		< 4.3(+14)	< 1.9(+14)	< 1.2(+14)	< 9.4(+13)	< 7.8(+13)
^{12}CO		1.5(+17)	6.3(+16)	6.5(+16)	7.0(+16)	7.5(+16)
	n_{H_2}	3×10^4 cm^{-3}				
molecule	T_k	10 K	20 K	30 K	40 K	50 K
c-C_3H_2 (ortho)		9.1(+12)	4.0(+12)	2.8(+12)	2.4(+12)	2.3(+12)
CCH		9.6(+13)	5.7(+13)	4.9(+13)	4.5(+13)	4.3(+13)
HCN		2.5(+13)	1.4(+13)	1.1(+13)	9.4(+12)	8.4(+12)

Table 3.14 (*continued*)

HCO^+		9.2(+12)	5.8(+12)	5.0(+12)	4.5(+12)	4.3(+12)
HNC		7.0(+12)	4.9(+12)	4.3(+12)	4.0(+12)	3.8(+12)
N_2H^+		7.5(+11)	5.2(+11)	4.5(+11)	4.1(+11)	3.9(+11)
CH_3OH (A)		< 3.1(+12)	< 2.5(+12)	< 2.5(+12)	< 2.5(+12)	< 2.6(+12)
CS		4.4(+13)	2.6(+13)	2.1(+13)	1.9(+13)	1.7(+13)
SO		2.8(+13)	1.6(+13)	1.3(+13)	1.2(+13)	1.1(+13)
$C^{18}O$		< 8.5(+14)	< 1.0(+15)	< 1.3(+15)	< 1.5(+15)	< 1.7(+15)
^{13}CO		7.8(+15)	9.3(+15)	1.1(+16)	1.3(+16)	1.5(+16)
CN		< 1.2(+14)	< 5.5(+13)	< 3.9(+13)	< 3.1(+13)	< 2.7(+13)
^{12}CO		1.4(+17)	7.3(+16)	8.1(+16)	9.2(+16)	1.0(+17)
	n_{H_2}	1×10^5 cm^{-3}				
molecule	T_k	10 K	20 K	30 K	40 K	50 K
c-C_3H_2 (ortho)		3.3(+12)	1.8(+12)	1.5(+12)	1.4(+12)	1.4(+12)
CCH		5.4(+13)	4.1(+13)	4.1(+13)	4.2(+13)	4.3(+13)
HCN		7.9(+12)	4.9(+12)	4.0(+12)	3.6(+12)	3.3(+12)
HCO^+		4.4(+12)	3.3(+12)	3.1(+12)	3.0(+12)	2.9(+12)
HNC		2.8(+12)	2.1(+12)	1.9(+12)	1.8(+12)	1.7(+12)
N_2H^+		4.1(+11)	3.2(+11)	3.1(+11)	3.0(+11)	3.0(+11)
CH_3OH (A)		< 2.7(+12)	< 2.7(+12)	< 3.1(+12)	< 3.4(+12)	< 3.7(+12)
CS		1.8(+13)	1.2(+13)	1.1(+13)	1.0(+13)	9.8(+12)
SO		1.4(+13)	1.0(+13)	9.9(+12)	1.0(+13)	1.0(+13)
$C^{18}O$		< 8.8(+14)	< 1.1(+15)	< 1.5(+15)	< 1.8(+15)	< 2.1(+15)
^{13}CO		8.2(+15)	1.0(+16)	1.3(+16)	1.6(+16)	1.8(+16)
CN		< 3.6(+13)	< 1.9(+13)	< 1.5(+13)	< 1.3(+13)	< 1.2(+13)
^{12}CO		1.3(+17)	7.9(+16)	9.2(+16)	1.1(+17)	1.2(+17)

[a] $a(+b)$ refers to $a \times 10^{+b}$ cm^{-2}.

3.4.2 IC10

Figure 3.17 shows the observed spectrum of IC10 in the frequency range from 84 to 100 GHz, which is a part of the total observed spectrum. We detected the lines of CCH($N = 1 - 0$), HCN($J = 1 - 0$), HCO^+($J = 1 - 0$), HNC($J = 1 - 0$; tentative detection), CS($J = 2 - 1$), and SO($N_J = 2_3 - 1_2$) in this frequency range for the first time. In addition, we also detected the lines of ^{13}CO($J = 1 - 0$) and ^{12}CO($J = 1 - 0$). On the other hand, the lines of c-C_3H_2($2_{12} - 1_{01}$), N_2H^+($J = 1 - 0$), CH_3OH($J_k = 2_0 - 1_0$, A^+), $C^{18}O$($J = 1 - 0$), and CN($N = 1 - 0$) were not detected (Figure 3.18). Surprisingly, the spectral intensity pattern of IC10 is very similar to that of the molecular cloud N44C in the LMC, although the molecular line intensities are weaker by a factor of about 1/6 than those toward N44C. Figure 3.19 (left) shows a correlation diagram between the integrated intensities of IC10 and those of N44C in the LMC. Indeed a good correlation is seen between the two sources. The correlation

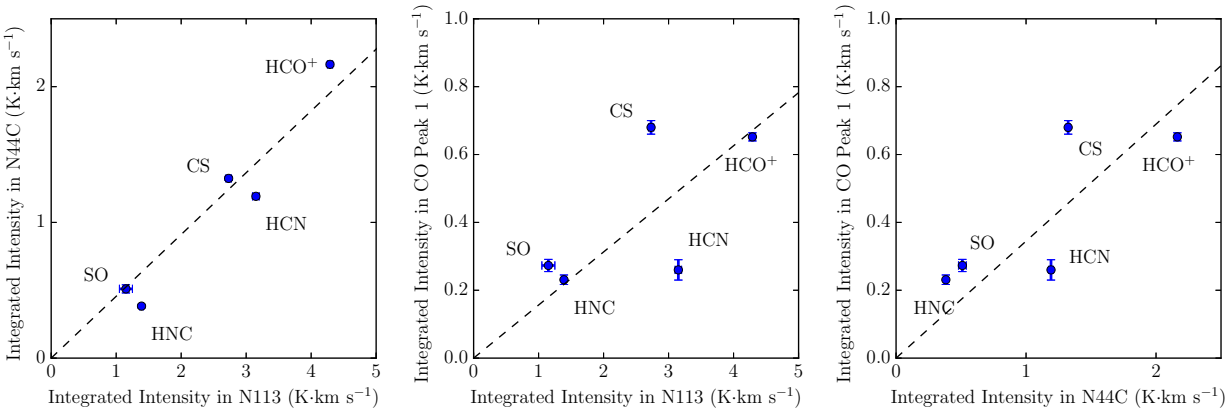

Figure 3.12 Correlation diagrams of integrated intensities of detected species between (*left*) N113 and N44C, (*middle*) N113 and CO Peak 1, and (*right*) N44C and CO Peak 1. Correlation coefficients are 0.971, 0.665, and 0.792, respectively. The dashed line indicates the average ratio of the integrated intensities of the two sources. The CS and SO lines tend to be relatively stronger in CO Peak 1.

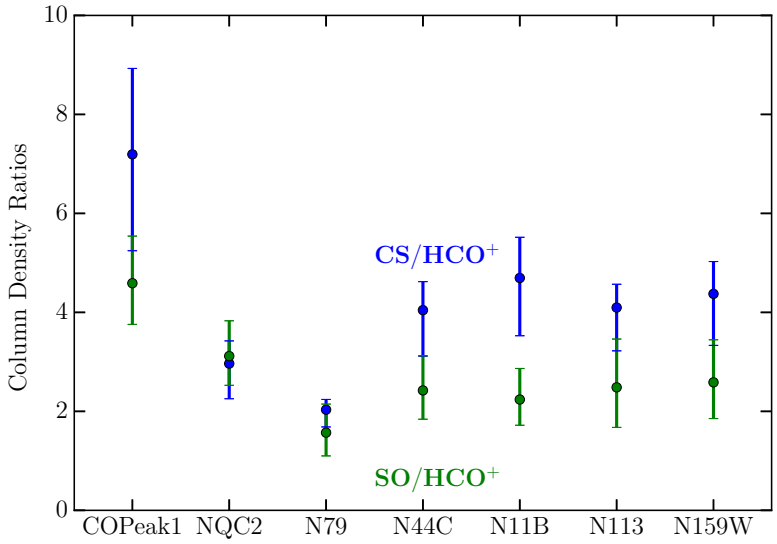

Figure 3.13 Column density ratios of CS/HCO^+ and SO/HCO^+ in the observed sources. The error bars include the errors caused by the assumed range of the gas kinetic temperature ($10 - 50$ K) and the gas density ($3 \times 10^3 - 1 \times 10^5$ cm^{-3}). The CS/HCO^+ and SO/HCO^+ ratios are higher in CO Peak 1.

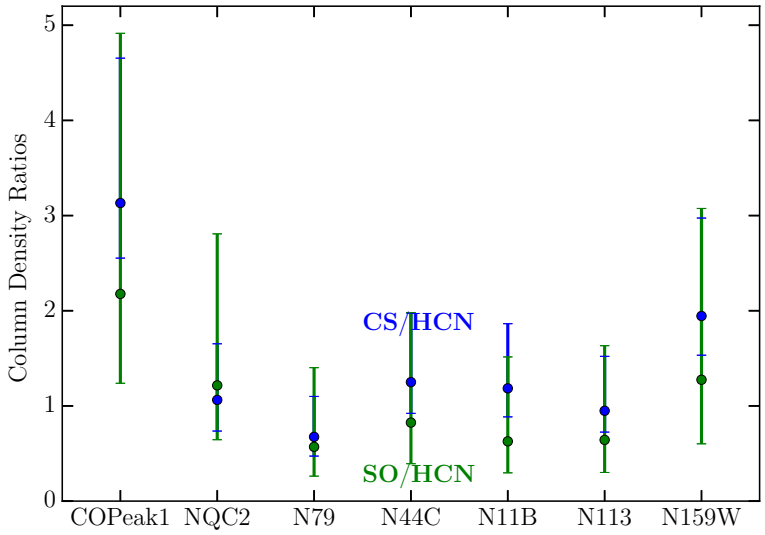

Figure 3.14 Column density ratios of CS/HCN and SO/HCN in the observed sources. The error bars include the errors caused by the assumed range of the gas kinetic temperature ($10 - 50$ K) and the gas density ($3 \times 10^3 - 1 \times 10^5$ cm^{-3}). A trend for CO Peak 1 seen in Figure 3.13 is also seen.

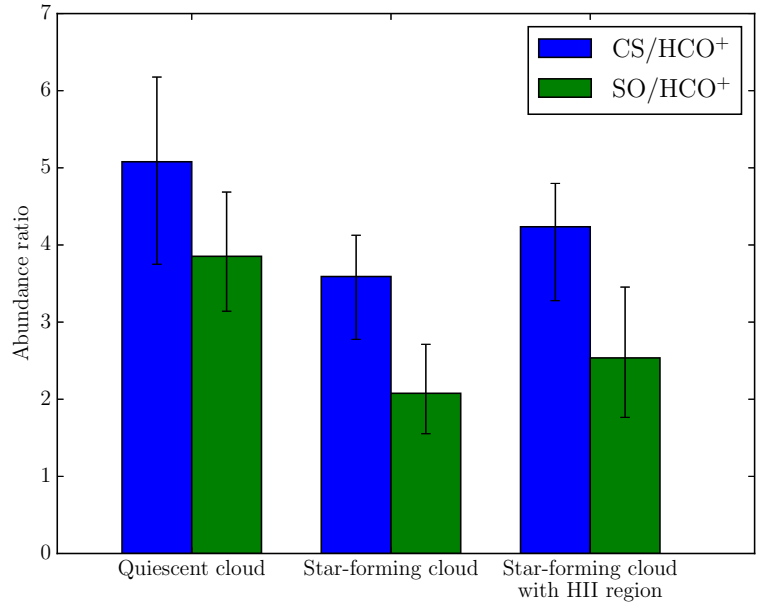

Figure 3.15 Averaged column density ratios of CS/HCO$^+$ and SO/HCO$^+$ of quiescent clouds (CO Peak 1 and NQC2), star-forming clouds (N79, N44C, and N11B), and star-forming clouds with H II regions (N113 and N159W) in the LMC. The error bars include the errors caused by the assumed range of the gas kinetic temperature ($10 - 50$ K) and the gas density ($3 \times 10^3 - 1 \times 10^5$ cm^{-3}). The CS/HCO$^+$ and SO/HCO$^+$ ratios are slightly high in quiescent clouds.

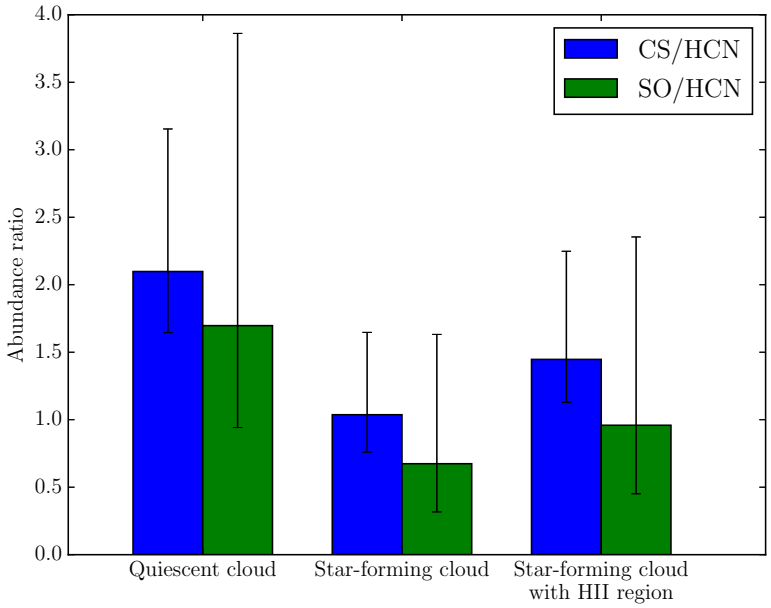

Figure 3.16 Averaged column density ratios of CS/HCN and SO/HCN of quiescent clouds (CO Peak 1 and NQC2), star-forming clouds (N79, N44C, and N11B), and star-forming clouds with H II regions (N113 and N159W) in the LMC. The error bars include the errors caused by the assumed range of the gas kinetic temperature ($10 - 50$ K) and the gas density ($3 \times 10^3 - 1 \times 10^5$ cm^{-3}).

coefficient is as high as 0.96. Even if the ^{13}CO data are excluded, it is 0.90. On the other hand, the spectrum toward IC10 significantly differs from that observed in the spiral arm of M51. This is also confirmed by the rather poor correlation in Figure 3.19 (right). The correlation coefficient is 0.83, while it is as low as 0.18 without ^{13}CO. As mentioned in Section 3.4.1, the spectrum of N44C reflects the molecular-cloud-scale chemical composition characteristic to the LMC, and hence, the similarity seems to originate from the low-metallicity environment of IC10.

The line parameters derived by Gaussian fitting are summarized in Table 3.15. The velocity of the intensity peak of the ^{12}CO line (-330.2 km s^{-1}) is consistent with the previous observation of the ^{12}CO ($J = 1 - 0$) line toward the same position with the Arizona Radio Observatory 12 m telescope (HPBW of $55''$) by Leroy et al. (2006) (-330.5 km s^{-1}). The integrated intensity of the ^{12}CO line observed by Leroy et al. (2006) is lower than ours only by a factor of 1.3, in spite of a large difference of the telescope beam size ($15.3''$ and $55.5''$). This result indicates that the ^{12}CO emitting region is at least extended over the beam size of the Nobeyama 45 m telescope. The $V_{\rm LSR}$ values of the detected lines range from -326 to -333 km s^{-1}, which are consistent with that of the ^{13}CO line. The line widths are mostly in the range from 12 km s^{-1} to 16 km s^{-1}. Exceptions are the HNC line and one of the CCH lines (87.401989 GHz) probably due to a poor signal to noise ratio (3.8σ) and the blending

of nearby hyperfine components, respectively (Figure 3.18).

We evaluated beam-averaged column densities by statistical equilibrium calculations, as we did for the LMC clouds. We employed the RADEX code (van der Tak et al., 2007) for this purpose. Since only one rotational transition was observed for each molecular species, we assumed a range of the gas kinetic temperature to be from 10 K to 50 K, and a range of the H_2 density from 3×10^3 cm^{-3} to 1×10^5 cm^{-3}. We assumed the wide range of the physical condition for robust estimate. The beam-averaged column densities were derived for the gas kinetic temperatures of 10 K, 20 K, 30 K, 40 K, and 50 K and the H_2 density of 3×10^3 cm^{-3}, 1×10^4 cm^{-3}, 3×10^4 cm^{-3}, and 1×10^5 cm^{-3}, as listed in Table 3.16.

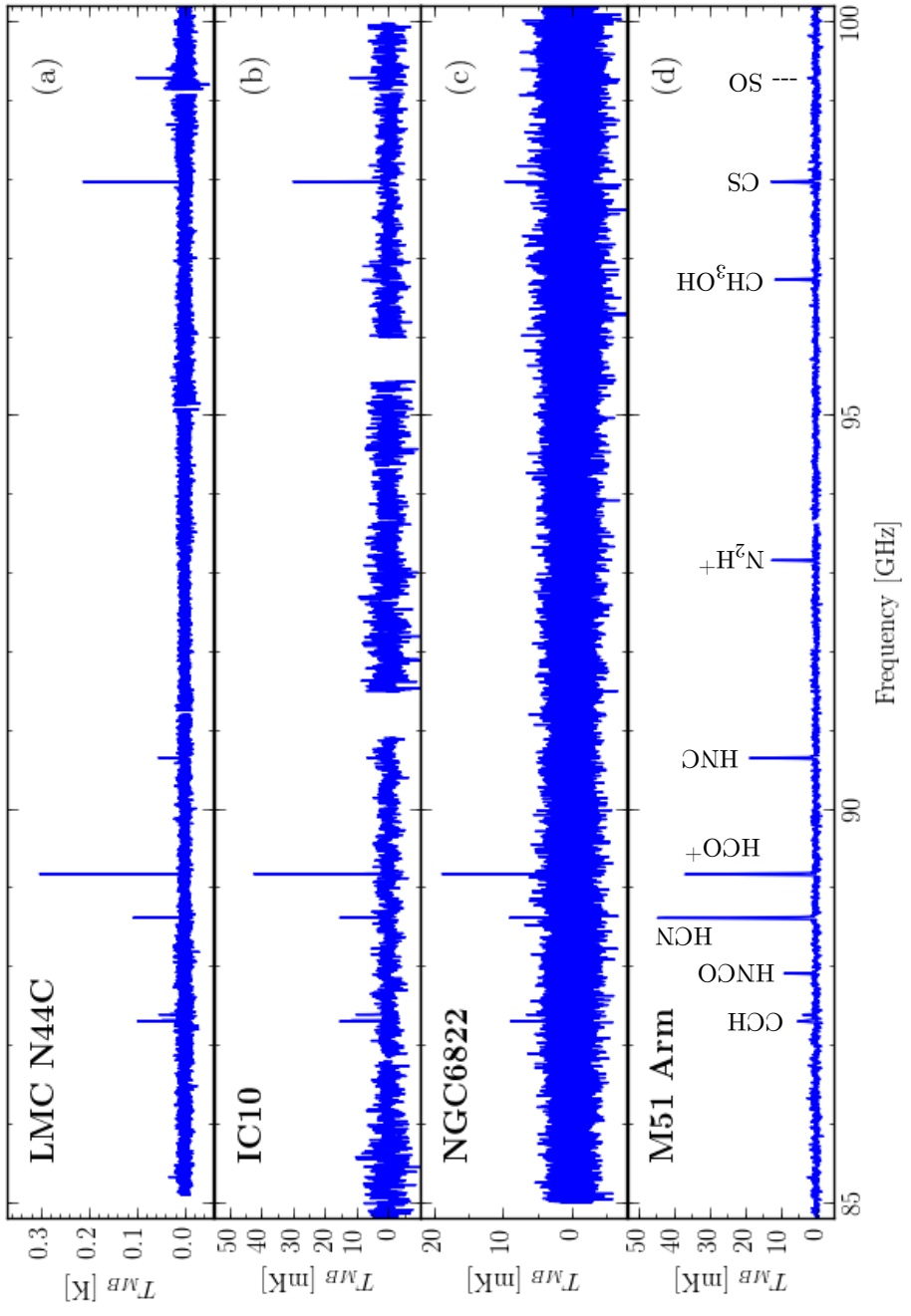

Figure 3.17 Compressed spectra observed toward (a) LMC N44C, (b) IC10, (c) NGC6822, and (d) the spiral arm of M51 (Watanabe et al., 2014). Note that the vertical scale is different from source to source.

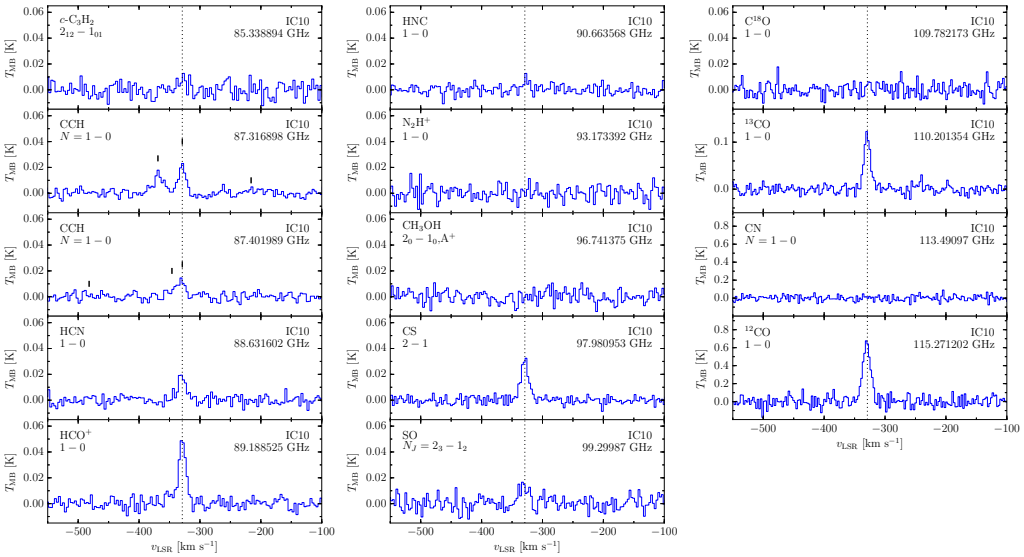

Figure 3.18 Spectral line profiles of individual molecular transitions observed toward IC10. Small vertical lines in the CCH panel represent the positions of the hyperfine components.

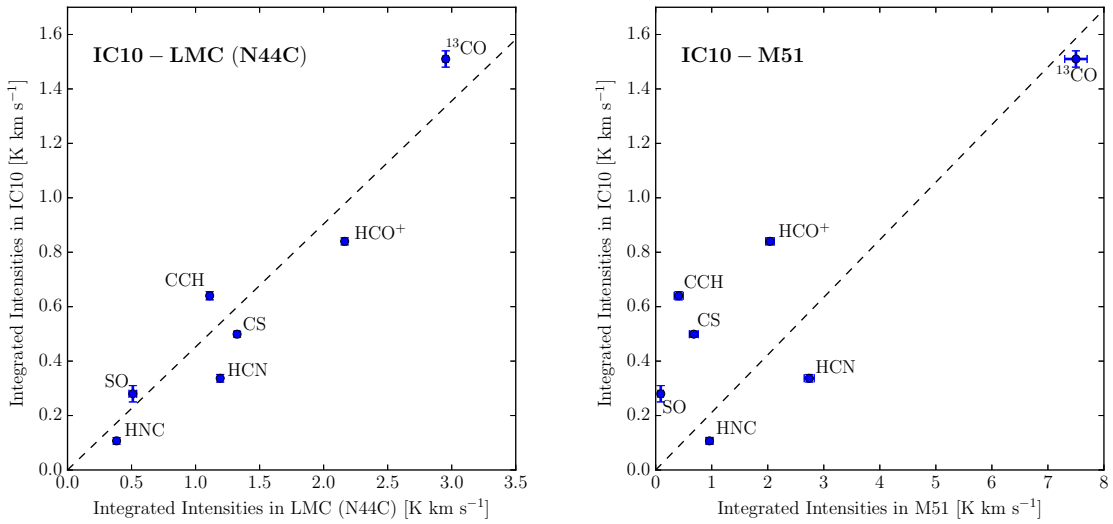

Figure 3.19 Correlation diagrams of integrated intensities of detected species (*left*) between IC10 and LMC (N44C), and (*right*) between IC10 and M51 (Watanabe et al., 2014). Correlation coefficients are 0.96 and 0.83, respectively. When the ^{13}CO data are excluded, they are 0.90 and 0.18, respectively. The dashed line indicates the average ratio of the integrated intensities between the two sources.

Table 3.15. Observed line parameters toward IC10.

Molecule	Frequency (GHz)	Transition	$T_{\rm MB}$ Peak (mK)	$v_{\rm LSR}$ (km s^{-1})	Δv (km s^{-1})	$\int T_{\rm MB} dv$ (K km s^{-1})
c-C_3H_2	85.338894	$2_{12} - 1_{01}$				< 0.12
CCH	87.284105	$N = 1 - 0$, $J = 5/2 - 3/2$, $F = 1 - 1$				< 0.05
CCH	87.316898	$N = 1 - 0$, $J = 5/2 - 3/2$, $F = 2 - 1$	20 ± 2	-328.9 ± 0.6	15.5 ± 1.4	0.329 ± 0.015
CCH	87.328585	$N = 1 - 0$, $J = 5/2 - 3/2$, $F = 1 - 0$	15.7 ± 1.9	–	–	0.311 ± 0.014
CCH	87.401989	$N = 1 - 0$, $J = 3/2 - 3/2$, $F = 1 - 1$	12 ± 3	-333 ± 2	21 ± 5	0.28 ± 0.03
CCH	87.407165	$N = 1 - 0$, $J = 3/2 - 3/2$, $F = 0 - 1$	–	–	–	–
CCH	87.446470	$N = 1 - 0$, $J = 3/2 - 3/2$, $F = 1 - 0$				< 0.05
HCN	88.631602	$1 - 0$	19 ± 2	-329.8 ± 0.8	15 ± 2	0.337 ± 0.014
HCO^+	89.188525	$1 - 0$	49 ± 2	-328.9 ± 0.3	13.9 ± 0.8	0.840 ± 0.013
HNC	90.663568	$1 - 0$	10 ± 3	-326.7 ± 1.2	9 ± 3	0.107 ± 0.012
N_2H^+	93.173392	$1 - 0$				< 0.11
CH_3OH	96.741375	$2_0 - 1_0$, A^+				< 0.09
CS	97.980953	$2 - 1$	30.7 ± 1.6	-329.2 ± 0.4	15.0 ± 0.9	0.499 ± 0.011
SO	99.299870	$N_J = 2_3 - 1_2$	14 ± 3	-331.2 ± 1.7	18 ± 4	0.28 ± 0.03
$C^{18}O$	109.782173	$1 - 0$				< 0.10
^{13}CO	110.201354	$1 - 0$	118 ± 5	-329.4 ± 0.3	12.0 ± 0.6	1.51 ± 0.03
CN	113.490970	$N = 1 - 0$, $J = 3/2 - 1/2$, $F = 5/2 - 3/2$				< 0.6
^{12}CO	115.271202	$1 - 0$	653 ± 31	-330.2 ± 0.3	15.1 ± 0.8	10.4 ± 0.2

Note. — The errors are 1σ. The upper limits are 3σ. The calibration error ($\sim 20\%$) is not included.

Table 3.16. Derived column densities for IC10.[a]

	n_{H_2}	3×10^3 cm^{-3}				
molecule	T_k	10 K	20 K	30 K	40 K	50 K
c-C_3H_2 (ortho)		< 2.7(+13)	< 1.1(+13)	< 6.7(+12)	< 5.5(+12)	< 5.2(+12)
CCH		2.4(+14)	1.1(+14)	8.6(+13)	7.1(+13)	6.2(+13)
HCN		5.3(+13)	2.8(+13)	2.2(+13)	1.9(+13)	1.6(+13)
HCO^+		1.4(+13)	8.3(+12)	6.7(+12)	5.8(+12)	5.3(+12)
HNC		6.1(+12)	4.1(+12)	3.6(+12)	3.3(+12)	3.1(+12)
N_2H^+		< 1.8(+12)	< 1.1(+12)	< 9.2(+11)	< 8.0(+11)	< 7.3(+11)
CH_3OH (A)		< 8.7(+12)	< 4.9(+12)	< 4.0(+12)	< 3.6(+12)	< 3.4(+12)
CS		6.5(+13)	3.8(+13)	3.0(+13)	2.5(+13)	2.3(+13)
SO		6.0(+13)	2.8(+13)	2.1(+13)	1.8(+13)	1.6(+13)
$C^{18}O$		< 8.5(+13)	< 7.8(+13)	< 8.1(+13)	< 8.5(+13)	< 8.9(+13)
^{13}CO		1.3(+15)	1.2(+15)	1.2(+15)	1.3(+15)	1.3(+15)
CN		< 5.0(+14)	< 2.2(+14)	< 1.5(+14)	< 1.1(+14)	< 9.4(+13)
^{12}CO		9.2(+15)	7.8(+15)	7.9(+15)	8.2(+15)	8.6(+15)
	n_{H_2}	1×10^4 cm^{-3}				
molecule	T_k	10 K	20 K	30 K	40 K	50 K
c-C_3H_2 (ortho)		< 7.9(+12)	< 3.3(+12)	< 2.1(+12)	< 1.8(+12)	< 1.7(+12)
CCH		7.8(+13)	4.1(+13)	3.2(+13)	2.8(+13)	2.5(+13)
HCN		1.4(+13)	8.2(+12)	6.4(+12)	5.5(+12)	4.9(+12)
HCO^+		4.3(+12)	2.7(+12)	2.2(+12)	1.9(+12)	1.8(+12)
HNC		1.8(+12)	1.3(+12)	1.1(+12)	1.0(+12)	9.9(+11)
N_2H^+		< 6.0(+11)	< 3.8(+11)	< 3.2(+11)	< 2.8(+11)	< 2.6(+11)
CH_3OH (A)		< 3.5(+12)	< 2.3(+12)	< 2.0(+12)	< 1.9(+12)	< 1.8(+12)
CS		2.0(+13)	1.2(+13)	9.5(+12)	8.2(+12)	7.4(+12)
SO		1.9(+13)	9.4(+12)	7.2(+12)	6.3(+12)	5.7(+12)
$C^{18}O$		< 8.6(+13)	< 9.6(+13)	< 1.1(+14)	< 1.3(+14)	< 1.4(+14)
^{13}CO		1.3(+15)	1.5(+15)	1.7(+15)	1.9(+15)	2.1(+15)
CN		< 1.3(+14)	< 6.0(+13)	< 4.2(+13)	< 3.4(+13)	< 2.9(+13)
^{12}CO		8.9(+15)	9.4(+15)	1.1(+16)	1.2(+16)	1.3(+16)
	n_{H_2}	3×10^4 cm^{-3}				
molecule	T_k	10 K	20 K	30 K	40 K	50 K
c-C_3H_2 (ortho)		< 2.8(+12)	< 1.3(+12)	< 8.7(+11)	< 7.6(+11)	< 7.3(+11)
CCH		3.4(+13)	2.1(+13)	1.8(+13)	1.6(+13)	1.6(+13)
HCN		4.9(+12)	2.8(+12)	2.3(+12)	2.0(+12)	1.8(+12)

Table 3.16 (*continued*)

HCO^+		1.7(+12)	1.2(+12)	1.0(+12)	9.3(+11)	8.8(+11)
HNC		6.9(+11)	4.9(+11)	4.3(+11)	4.1(+11)	3.9(+11)
N_2H^+		< 2.6(+11)	< 1.8(+11)	< 1.5(+11)	< 1.4(+11)	< 1.4(+11)
CH_3OH (A)		< 2.2(+12)	< 1.7(+12)	< 1.7(+12)	< 1.7(+12)	< 1.8(+12)
CS		7.5(+12)	4.7(+12)	3.9(+12)	3.5(+12)	3.2(+12)
SO		7.4(+12)	4.2(+12)	3.5(+12)	3.2(+12)	3.1(+12)
$C^{18}O$		< 9.3(+13)	< 1.2(+14)	< 1.4(+14)	< 1.7(+14)	< 1.9(+14)
^{13}CO		1.4(+15)	1.7(+15)	2.1(+15)	2.5(+15)	2.9(+15)
CN		< 4.1(+13)	< 2.1(+13)	< 1.5(+13)	< 1.3(+13)	< 1.1(+13)
^{12}CO		9.5(+15)	1.1(+16)	1.4(+16)	1.6(+16)	1.8(+16)
	n_{H_2}	1×10^5 cm^{-3}				
molecule	T_k	10 K	20 K	30 K	40 K	50 K
c-C_3H_2 (ortho)		< 1.0(+12)	< 5.6(+11)	< 4.7(+11)	< 4.5(+11)	< 4.4(+11)
CCH		1.9(+13)	1.5(+13)	1.5(+13)	1.5(+13)	1.6(+13)
HCN		1.7(+12)	1.0(+12)	8.7(+11)	7.8(+11)	7.2(+11)
HCO^+		8.9(+11)	6.9(+11)	6.5(+11)	6.3(+11)	6.3(+11)
HNC		2.9(+11)	2.2(+11)	2.0(+11)	1.9(+11)	1.8(+11)
N_2H^+		< 1.4(+11)	< 1.1(+11)	< 1.0(+11)	< 1.0(+11)	< 1.0(+11)
CH_3OH (A)		< 1.9(+12)	< 1.9(+12)	< 2.1(+12)	< 2.3(+12)	< 2.5(+12)
CS		3.3(+12)	2.3(+12)	2.1(+12)	2.0(+12)	1.9(+12)
SO		3.8(+12)	2.8(+12)	2.7(+12)	2.7(+12)	2.8(+12)
$C^{18}O$		< 9.7(+13)	< 1.3(+14)	< 1.6(+14)	< 2.0(+14)	< 2.3(+14)
^{13}CO		1.5(+15)	1.9(+15)	2.5(+15)	3.0(+15)	3.5(+15)
CN		< 1.4(+13)	< 7.9(+12)	< 6.2(+12)	< 5.4(+12)	< 4.9(+12)
^{12}CO		9.9(+15)	1.2(+16)	1.6(+16)	1.9(+16)	2.2(+16)

[a] $a(+b)$ refers to $a \times 10^{+b}$ cm^{-2}.

3.4.3 NGC6822

Figure 3.17 shows the observed spectrum in the frequency range from 85 to 100 GHz, which is a part of the total observed spectrum. Although the lines are generally faint, we detected the lines of CCH ($N = 1 - 0$), HCN ($J = 1 - 0$), HCO^+ ($J = 1 - 0$), and CS ($J = 2 - 1$) in this frequency range. In addition, we also detected the lines of ^{13}CO ($J = 1 - 0$) and ^{12}CO ($J = 1 - 0$) in the 3 mm band and ortho-H_2CO($2_{12} - 1_{11}$), para-H_2CO ($2_{02} - 1_{01}$), and CS ($J = 3 - 2$) in the 2 mm band. HNC and SO, which were detected in the LMC and IC10, were not detected in NGC6822 in this observation, probably because of insufficient sensitivity. As in the case of IC10, the lines of c-C_3H_2 ($2_{12} - 1_{01}$), N_2H^+ ($J = 1 - 0$), CH_3OH ($J_k = 2_0 - 1_0$, A^+), $C^{18}O$ ($J = 1 - 0$), and CN ($N = 1 - 0$) were not detected (Figure **??**). The line parameters derived by Gaussian fitting are summarized in Table 3.17. Judging from this result, NGC6822 is found to have similar spectral intensity pattern in the 3 mm

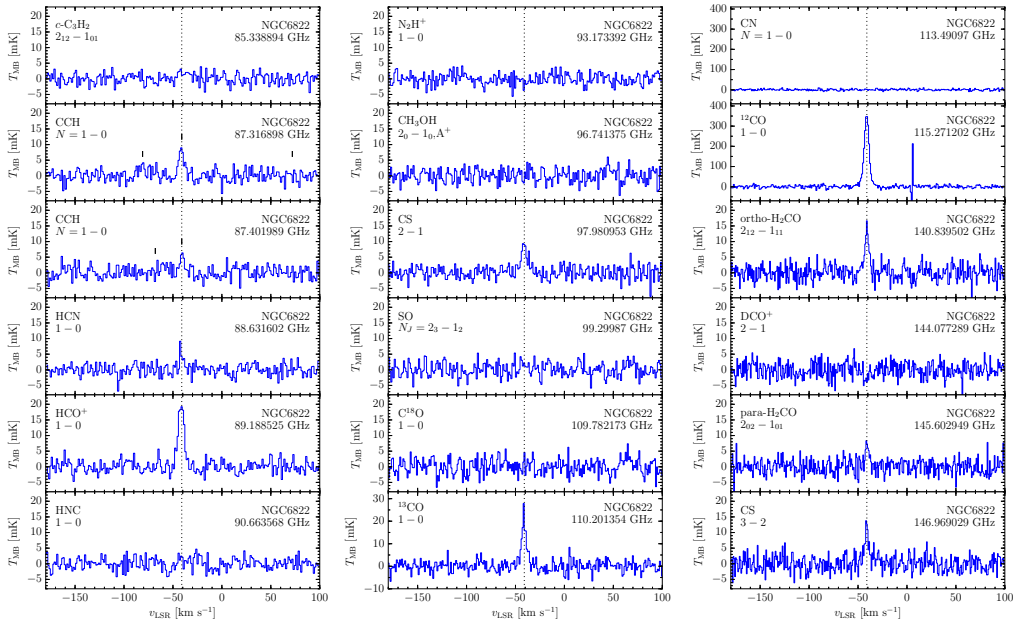

Figure 3.20 Spectral line profiles of individual molecular transitions observed in NGC6822. Small vertical lines in the CCH panel represent the positions of the hyperfine components.

band to the LMC and IC10.

In spite of the general resemblance of the spectra of the LMC, IC10, and NGC6822, the ^{13}CO line is found to be much fainter in NGC6822 than the LMC and IC10. Figure 3.21 shows the correlation of integrated intensities of NGC6822 versus those of IC10 and the LMC cloud (N44C). Even though the data of NGC6822 are well correlated with those of IC10 and the LMC for the most molecular species, the intensity of ^{13}CO is significantly low in NGC6822. Indeed, the ^{12}CO ($J = 1 - 0$)/^{13}CO ($J = 1-0$) intensity ratio of NGC6822 is much higher (16.5) than those of IC10 (6.9) and the LMC (6.8; average of 7 clouds). This result implies that the ^{12}CO/^{13}CO abundance ratio in NGC6822 is high. There are several possibilities for the high ^{12}CO/^{13}CO intensity ratio, such as excitation conditions, optical depth effects, chemical fractionation, isotope selective photodissociation, and nucleosynthesis history (the high $^{12}/^{13}$C ratio). To establish this ^{12}CO/^{13}CO anomaly and explore its origin, further observations are necessary.

For NGC6822, we evaluated beam-averaged column densities by statistical equilibrium calculations using the RADEX code (van der Tak et al., 2007), as described in Section 3.4.1. The gas kinetic temperatures of 10 K, 20 K, 30 K, 40 K, and 50 K and the H_2 density of 3×10^3 cm^{-3}, 1×10^4 cm^{-3}, 3×10^4 cm^{-3}, and 1×10^5 cm^{-3} are assumed. The derived column densities are listed in Table 3.18.

Table 3.17. Observed line parameters toward NGC6822.

Molecule	Frequency (GHz)	Transition	$T_{\rm MB}$ Peak (mK)	$v_{\rm LSR}$ (km s^{-1})	Δv (km s^{-1})	$\int T_{\rm MB} dv$ (K km s^{-1})
c-C_3H_2	85.338894	$2_{12} - 1_{01}$				< 0.013
CCH	87.284105	$N = 1 - 0$, $J = 5/2 - 3/2$, $F = 1 - 1$				< 0.014
CCH	87.316898	$N = 1 - 0$, $J = 5/2 - 3/2$, $F = 2 - 1$	8.6 ± 1.1	-41.5 ± 0.4	6.2 ± 0.9	0.057 ± 0.004
CCH	87.328585	$N = 1 - 0$, $J = 5/2 - 3/2$, $F = 1 - 0$	3.5 ± 0.9	–	–	0.020 ± 0.005
CCH	87.401989	$N = 1 - 0$, $J = 3/2 - 3/2$, $F = 1 - 1$	5.8 ± 1.2	-40.8 ± 0.5	5.7 ± 1.3	0.035 ± 0.004
CCH	87.407165	$N = 1 - 0$, $J = 3/2 - 3/2$, $F = 0 - 1$	3.0 ± 1.1	–	–	0.020 ± 0.004
CCH	87.446470	$N = 1 - 0$, $J = 3/2 - 3/2$, $F = 1 - 0$				< 0.015
HNCO	87.925237	$4_{04} - 3_{03}$				< 0.015
HCN	88.631602	$1 - 0$	11 ± 4	-42.2 ± 0.3	1.7 ± 0.7	0.0291 ± 0.0011
HCO^+	89.188525	$1 - 0$	20.3 ± 1.1	-41.65 ± 0.19	7.1 ± 0.5	0.154 ± 0.004
HNC	90.663568	$1 - 0$				< 0.015
N_2H^+	93.173392	$1 - 0$				< 0.014
CH_3OH	96.741375	$2_0 - 1_0$, A^+				< 0.017
CS	97.980953	$2 - 1$	8.4 ± 1.0	-41.0 ± 0.5	8.3 ± 1.2	0.079 ± 0.004
SO	99.299870	$N_J = 2_3 - 1_2$				< 0.017
$C^{18}O$	109.782173	$1 - 0$				< 0.018
^{13}CO	110.201354	$1 - 0$	21.6 ± 1.5	-41.39 ± 0.19	5.5 ± 0.4	0.136 ± 0.004
CN	113.490970	$N = 1 - 0$, $J = 3/2 - 1/2$, $F = 5/2 - 3/2$				< 0.03
^{12}CO	115.271202	$1 - 0$	351 ± 9	-41.20 ± 0.08	5.80 ± 0.18	2.24 ± 0.02
H_2CO	140.839502	$2_{12} - 1_{11}$ (ortho)	14.0 ± 1.4	-40.9 ± 0.2	4.8 ± 0.5	0.078 ± 0.003
DCO^+	144.077289	$2 - 1$				< 0.015
CH_3OH	145.093707	$3_0 - 2_0$, A^+				< 0.016
H_2CO	145.602949	$2_{02} - 1_{01}$ (para)	7.5 ± 1.4	-40.6 ± 0.4	4.3 ± 0.9	0.034 ± 0.003
CS	146.969029	$3 - 2$	11.7 ± 1.4	-41.2 ± 0.3	4.8 ± 0.7	0.060 ± 0.004

Note. — The errors are 1σ. The upper limits are 3σ.

Table 3.18. Derived column densities for NGC6822.[a]

	n_{H_2}	3×10^3 cm^{-3}				
molecule	T_k	10 K	20 K	30 K	40 K	50 K
c-C_3H_2 (ortho)		< 2.8(+12)	< 1.1(+12)	< 7.2(+11)	< 5.9(+11)	< 5.6(+11)
CCH		4.0(+13)	1.9(+13)	1.5(+13)	1.2(+13)	1.1(+13)
HCN		4.4(+12)	2.4(+12)	1.9(+12)	1.6(+12)	1.4(+12)
HCO^+		2.4(+12)	1.4(+12)	1.2(+12)	1.0(+12)	9.5(+11)
HNC		< 8.2(+11)	< 5.6(+11)	< 5.0(+11)	< 4.6(+11)	< 4.4(+11)
N_2H^+		< 2.3(+11)	< 1.4(+11)	< 1.2(+11)	< 1.0(+11)	< 9.3(+10)
CH_3OH (A)		< 1.6(+12)	< 9.3(+11)	< 7.6(+11)	< 6.8(+11)	< 6.4(+11)
CS		9.8(+12)	5.8(+12)	4.6(+12)	3.9(+12)	3.5(+12)
SO		< 3.6(+12)	< 1.7(+12)	< 1.3(+12)	< 1.1(+12)	< 9.8(+11)
$C^{18}O$		< 1.5(+13)	< 1.4(+13)	< 1.4(+13)	< 1.5(+13)	< 1.6(+13)
^{13}CO		1.2(+14)	1.1(+14)	1.1(+14)	1.2(+14)	1.2(+14)
CN		< 1.9(+13)	< 9.5(+12)	< 6.7(+12)	< 5.2(+12)	< 4.4(+12)
^{12}CO		1.9(+15)	1.7(+15)	1.7(+15)	1.8(+15)	1.8(+15)
	n_{H_2}	1×10^4 cm^{-3}				
molecule	T_k	10 K	20 K	30 K	40 K	50 K
c-C_3H_2 (ortho)		< 8.5(+11)	< 3.6(+11)	< 2.3(+11)	< 2.0(+11)	< 1.8(+11)
CCH		1.3(+13)	7.1(+12)	5.6(+12)	4.8(+12)	4.4(+12)
HCN		1.2(+12)	7.0(+11)	5.5(+11)	4.7(+11)	4.2(+11)
HCO^+		7.7(+11)	4.9(+11)	4.0(+11)	3.6(+11)	3.3(+11)
HNC		< 2.6(+11)	< 1.8(+11)	< 1.6(+11)	< 1.4(+11)	< 1.4(+11)
N_2H^+		< 7.6(+10)	< 4.9(+10)	< 4.1(+10)	< 3.6(+10)	< 3.4(+10)
CH_3OH (A)		< 6.6(+11)	< 4.3(+11)	< 3.8(+11)	< 3.6(+11)	< 3.5(+11)
CS		3.1(+12)	1.9(+12)	1.5(+12)	1.3(+12)	1.2(+12)
SO		< 1.1(+12)	< 5.7(+11)	< 4.4(+11)	< 3.8(+11)	< 3.5(+11)
$C^{18}O$		< 1.6(+13)	< 1.7(+13)	< 2.0(+13)	< 2.3(+13)	< 2.5(+13)
^{13}CO		1.2(+14)	1.3(+14)	1.5(+14)	1.7(+14)	1.9(+14)
CN		< 5.8(+12)	< 2.9(+12)	< 2.1(+12)	< 1.6(+12)	< 1.4(+12)
^{12}CO		1.9(+15)	2.0(+15)	2.3(+15)	2.5(+15)	2.8(+15)
	n_{H_2}	3×10^4 cm^{-3}				
molecule	T_k	10 K	20 K	30 K	40 K	50 K
c-C_3H_2 (ortho)		< 3.0(+11)	< 1.4(+11)	< 9.5(+10)	< 8.3(+10)	< 7.9(+10)
CCH		5.9(+12)	3.6(+12)	3.1(+12)	2.8(+12)	2.7(+12)
HCN		4.2(+11)	2.5(+11)	2.0(+11)	1.7(+11)	1.5(+11)

Table 3.18 (*continued*)

HCO^+		3.2(+11)	2.1(+11)	1.8(+11)	1.7(+11)	1.6(+11)
HNC		< 9.5(+10)	< 6.8(+10)	< 6.0(+10)	< 5.6(+10)	< 5.4(+10)
N_2H^+		< 3.3(+10)	< 2.2(+10)	< 1.9(+10)	< 1.8(+10)	< 1.7(+10)
CH_3OH (A)		< 4.1(+11)	< 3.3(+11)	< 3.2(+11)	< 3.3(+11)	< 3.3(+11)
CS		1.2(+12)	7.5(+11)	6.2(+11)	5.5(+11)	5.1(+11)
SO		< 4.5(+11)	< 2.6(+11)	< 2.1(+11)	< 2.0(+11)	< 1.9(+11)
$C^{18}O$		< 1.7(+13)	< 2.1(+13)	< 2.5(+13)	< 3.0(+13)	< 3.4(+13)
^{13}CO		1.3(+14)	1.6(+14)	1.9(+14)	2.3(+14)	2.6(+14)
CN		< 2.0(+12)	< 1.0(+12)	< 7.6(+11)	< 6.2(+11)	< 5.4(+11)
^{12}CO		2.0(+15)	2.4(+15)	2.9(+15)	3.4(+15)	3.9(+15)
	n_{H_2}	1×10^5 cm^{-3}				
molecule	T_k	10 K	20 K	30 K	40 K	50 K
c-C_3H_2 (ortho)		< 1.1(+11)	< 6.1(+10)	< 5.1(+10)	< 4.9(+10)	< 4.8(+10)
CCH		3.3(+12)	2.6(+12)	2.6(+12)	2.6(+12)	2.7(+12)
HCN		1.4(+11)	9.1(+10)	7.5(+10)	6.7(+10)	6.2(+10)
HCO^+		1.6(+11)	1.3(+11)	1.2(+11)	1.2(+11)	1.2(+11)
HNC		< 4.0(+10)	< 3.0(+10)	< 2.7(+10)	< 2.6(+10)	< 2.5(+10)
N_2H^+		< 1.8(+10)	< 1.4(+10)	< 1.3(+10)	< 1.3(+10)	< 1.3(+10)
CH_3OH (A)		< 3.6(+11)	< 3.6(+11)	< 4.0(+11)	< 4.4(+11)	< 4.8(+11)
CS		5.3(+11)	3.7(+11)	3.3(+11)	3.1(+11)	3.0(+11)
SO		< 2.3(+11)	< 1.7(+11)	< 1.6(+11)	< 1.7(+11)	< 1.7(+11)
$C^{18}O$		< 1.7(+13)	< 2.3(+13)	< 2.9(+13)	< 3.6(+13)	< 4.2(+13)
^{13}CO		1.3(+14)	1.7(+14)	2.2(+14)	2.7(+14)	3.2(+14)
CN		< 7.0(+11)	< 3.9(+11)	< 3.1(+11)	< 2.7(+11)	< 2.5(+11)
^{12}CO		2.1(+15)	2.7(+15)	3.4(+15)	4.1(+15)	4.7(+15)

[a] $a(+b)$ refers to $a \times 10^{+b}$ cm^{-2}.

3.4.4 NGC55

We observed the ^{12}CO line toward the 4 positions, P1, P2, P3, and P4, in NGC55. As a result, we detected the ^{12}CO line only in P1 with the peak intensity of 0.12 K (Figure 3.22), which is the second brightest position in the 24 μm continuum. P2 is the brightest in the 24 μm continuum (Engelbracht et al., 2004), and is also reported to be one of the brightest position in ^{12}CO ($J = 1 - 0$; ~ 0.14 K) by the result by Dettmar & Heithausen (1989). However, we found that that ^{12}CO is faint (< 0.05 K) toward P2 in our Mopra observations (Figure 3.22). The line parameters are summarized in Table 3.19. The ^{12}CO emission is found to be brighter in P1 (40 arcsec away from P2). A possible reason for this discrepancy between our result and Dettmar & Heithausen (1989) is puzzling, but it may be the difference of the beam size, where the beam size of Mopra 22 m (30 arcsec) is smaller than that of SEST 15 m (43.5 arcsec).

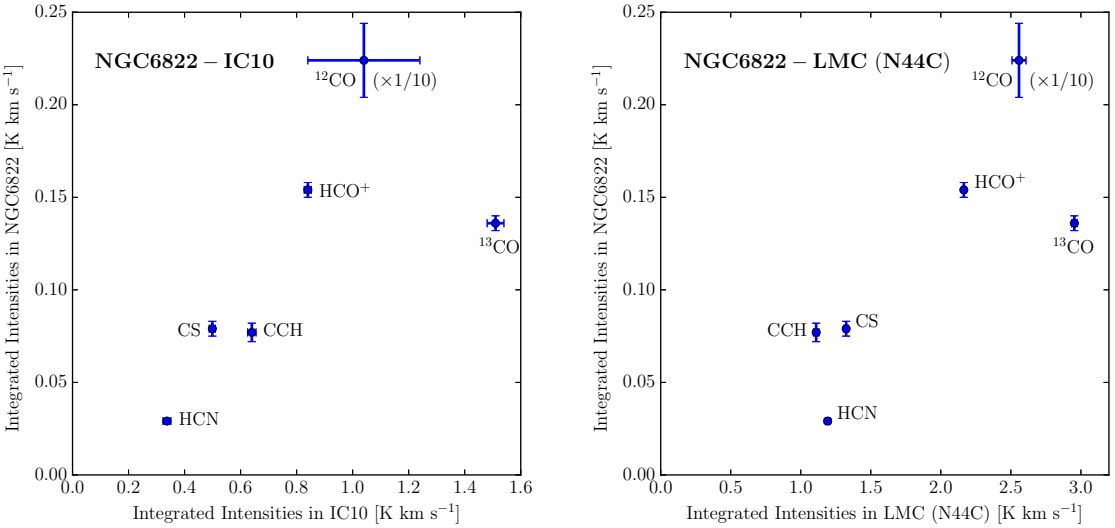

Figure 3.21 Correlation diagrams of integrated intensities of detected species (*left*) between NGC6822 and IC10, and (*right*) between NGC6822 and the LMC (N44C). Correlation coefficients among CCH, HCN, HCO^+, and CS are 0.954 and 0.893, respectively. When ^{13}CO is taken into account, correlation coefficients are 0.762 and 0.808, respectively. ^{13}CO is apparently faint in NGC6822.

After we confirmed the ^{12}CO detection in P1, we observed the HCO^+ and CS lines toward P1. However, the sensitivity of the Mopra 22 m telescope seems to be not enough to detect these molecular lines in this galaxy. Although we found a hint of the HCO^+ line, it is heavily disturbed by the periodic base line distortion. Hence, the detection of HCO^+ is left for future observations.

We also conducted the observation of the ^{12}CO ($J = 3 - 2$) line toward NGC55 with the ASTE 10 m telescope. The ^{12}CO line ($J = 3 - 2$) line was successfully detected toward the P1 position with the peak intensity of 0.15 K in $T_{\rm MB}$. Considering that the $J = 3 - 2$ transition is brighter than the $J = 1 - 0$ transition, the high temperature and high H_2 density condition is expected in P1. Such a physical environment might be responsible for the faintness of the low-J transition lines of the other molecules. Hence, we think that non-detection of molecular lines other than ^{12}CO does not necessarily mean the deficiency of dense molecular gas in NGC55. Sensitive submillimeter-wave observations of the other molecules are awaited.

3.4.5 NGC185

We conducted observations of NGC185 in the same way as we did for IC10. We only detected the ^{12}CO and ^{13}CO lines in NGC185. Although we achieved the rms noise temperature of $\sim$ 2 mK (T_A^*), neither of HCO^+ nor CS was detected. To explore chemical composition of this galaxy, higher sensitivity observation is necessary. We found the peak intensity of ^{12}CO to be 91 mK and that

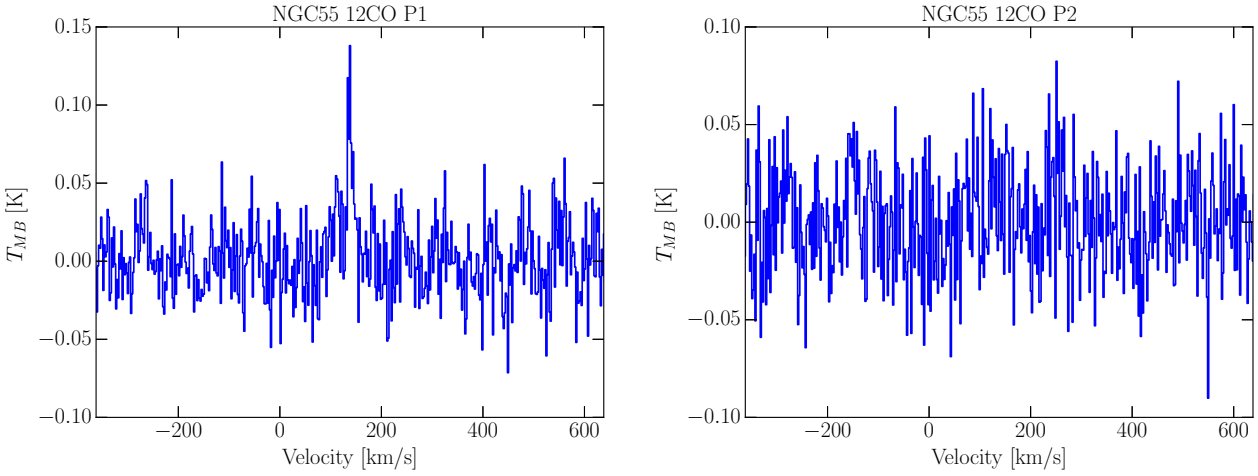

Figure 3.22 The CO ($J = 1 - 0$) line observed toward (*left*) P1 and (*right*) P2 in NGC55.

Table 3.19. Observed line parameters of the CO ($J = 1 - 0$) line in NGC55.

Position	$T_{\rm MB}$ Peak (mK)	$v_{\rm LSR}$ (km s^{-1})	Δv (km s^{-1})	$\int T_{\rm MB} dv$ (K km s^{-1})
P1	103.8 ± 13.1	138.2 ± 0.8	12.8 ± 1.9	1.4 ± 0.3
P2	···	···	···	< 0.100
P3	···	···	···	< 0.421
P4	···	···	···	< 0.627

Note. — The errors are 1σ. The upper limits are 3σ. The calibration error ($\sim 20\%$) is not included.

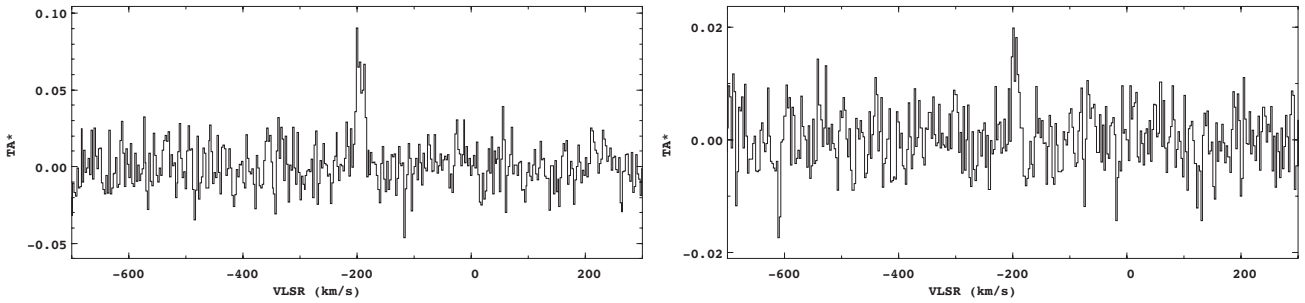

Figure 3.23 (*left*) The ^{12}CO ($J = 1 - 0$) line and (*right*) the ^{13}CO ($J = 1 - 0$) line observed toward NGC185.

of ^{13}CO to be 14 mK in $T_A{}^*$. The intensity of ^{12}CO is comparable to or somewhat lower than the previous reports of the ^{12}CO observation (Young & Lo, 1997; Young, 2001). The ^{12}CO/^{13}CO integrated intensity ratio is almost comparable to the LMC and IC10.

3.5 Characteristic Chemical Composition of Low-Metallicity Dwarf Galaxies

3.5.1 Effect of Elemental Abundances

Elemental abundances are measured toward H II regions in each galaxy mainly by optical lines. They are known to be different from galaxies to galaxies, reflecting the past history of star formation. Here, we assumed the elemental abundances in molecular clouds to be same as that of the H II regions. In the low-metallicity galaxies, heavy elements are generally deficient, and in particular, the deficiency of nitrogen is the most significant among the abundant second row elements (C, N, O) (Vincenzo et al., 2016). Because of this reason, one of the characteristic features in the chemical compositions would be the deficiency of the N-bearing molecules. The chemical model by Millar & Herbst (1990) indeed predicted that abundances of N-bearing molecules are sensitive to the elemental abundance of nitrogen. The deficiency of the N-bearing molecules is evident in the spectral pattern of the observed low-metallicity galaxies in comparison with that of the spiral arm of M51. To confirm the deficiency

of the N-bearing molecules in dwarf galaxies, we calculated the abundance ratios of HCN/HCO^+ and HNC/HCO^+ for the dwarf galaxies NGC6822, IC10, and the LMC, under the assumption of the H_2 density of 3×10^3, 1×10^4, 3×10^4, and 1×10^5 cm^{-3}, and the gas kinetic temperature of 10, 20, 30, 40, and 50 K. As we cannot determine the physical condition of the cloud only from one transition line for each molecular species, we assumed the wide range of H_2 density and temperature for robust estimate. We compared the column density ratios with the average ratios for the three translucent clouds (CB17, CB24, CB228) in our Galaxy (Turner, 1995b; Turner et al., 1997), and the ratio for the spiral arm position (P1) of M51 observed by Watanabe et al. (2014), as shown in Table 3.20. The observed spectra are ones averaged over molecular clouds ($\sim$ 80 pc scale for IC10 and $\sim$ 60 pc scale for NGC6822), and seem to be dominated by the diffuse part of molecular clouds rather than dense star-forming cores (typically 0.1 pc scale; See Chapter 4). This is true even for smaller-scale observations of the LMC clouds ($\sim$ 10 pc scale). Hence, for fair comparison, we chose the translucent clouds as representatives of our Galaxy. Although the column densities are sensitive to the assumed H_2 density and the assumed gas kinetic temperature, the column density ratios are affected only less than $\pm$50% in the above range of the H_2 density and temperature. Note that the errors in Table 3.20 and Figure 3.24, 3.25, and 3.26 are estimated from the variation due to the assumed gas kinetic temperature and H_2 density. Measurement and fitting errors are considered to be smaller (< 20 %) than the above errors.

The elemental N/O ratios in dwarf galaxies are lower by a factor of 3 than that in our Galaxy (Table 3.20 and Figure 3.24). The HCN/HCO^+ and HNC/HCO^+ ratios in NGC6822, IC10, and the LMC are indeed found to be lower than in the three Galactic translucent clouds (CB17, CB24, CB228). Although the HCN/HCO^+ ratios of IC10 and the LMC marginally overlap with that of the Galactic translucent clouds within the mutual error ranges, the overlap occurs only for the particular conditions that is not very likely (3×10^3 cm^{-3} and 10 K for IC10 and the LMC and 1×10^5 cm^{-3} and 50 K for the Galactic translucent clouds). Hence, we can state the above conclusion in spite of the formal error ranges. A similar comparison can also be made for M51 P1, which has the higher N/O ratio than the Solar neighborhood by a factor of 2 (Bresolin et al., 2004). The HCN/HCO^+ and HNC/HCO^+ ratios in M51 P1 are $8.4^{+4.0}_{-4.6}$ and $1.6^{+0.6}_{-0.6}$, respectively, which are higher than those in NGC6822 ($1.2^{+0.6}_{-0.47}$ and < 0.3, respectively), IC10 ($2.5^{+1.3}_{-1.4}$ and $0.4^{+0.2}_{-0.2}$, respectively), and the LMC ($3.4^{+1.3}_{-1.8}$ and $0.8^{+0.3}_{-0.3}$, respectively). As shown in Table 3.21, the HCN/HCO^+ and HNC/HCO^+ ratios vary by $\pm$40 % and $\pm$50 %, respectively, among the observed seven clouds in the LMC. Indeed, the variation range of HCN/HCO^+ and HNC/HCO^+ is smaller than the difference of N/O ratio (a factor of $3 - 7$) between dwarf galaxies and spiral galaxies. This means that the deficiency of N-bearing

molecules is not caused by the environmental effects peculiar to each molecular cloud but is mainly caused by the lower elemental nitrogen abundances. This fact also suggests that the observed chemical composition reflects general characteristics of the galaxy rather than each star-forming region. Hence, it is most likely that the deficiency of the N-bearing molecules directly reflects the elemental deficiency of nitrogen in the IC10.

The HCN/HCO^+ ratio for nuclear regions of external galaxies has been discussed actively. The HCN/HCO^+ ratio is known to be higher for the AGNs, which is interpreted as the effect of XDRs, cosmic-rays, and/or shock heatings (e.g., Lepp & Dalgarno, 1996; Kohno et al., 2001; Meijerink et al., 2007; Aladro et al., 2015). In this study, we observed molecular clouds without such effects, and found the lower HCN/HCO^+ ratio than the Galactic translucent clouds. Hence, the various effects suggested for the AGNs cannot be applied to these dwarf galaxies. Rather, the intrinsic effect of the elemental abundance can be seen in dwarf galaxies.

It is noteworthy that $C^{18}O$ is not detected in any dwarf galaxies, while it is as bright as HCO^+ in M51 (Watanabe et al., 2014). Because ^{18}O is a product of α-capture on ^{14}N, the low abundance of $C^{18}O$ in dwarf galaxies may reflect the deficiency of ^{18}O atoms. The elemental abundance of ^{18}O is not known for these dwarf galaxies, as the atomic ^{18}O and ^{16}O lines cannot be distinguished due to the line blending. We should also note that the selective photodissociation of $C^{18}O$ (van Dishoeck & Black, 1988) or chemical fractionation/dilution may also affect the abundance of $C^{18}O$.

While nitrogen is characteristically less abundant, sulfur is relatively abundant in low-metallicity galaxies. The elemental S/O ratio is actually higher in low-metallicity galaxies than in the Solar neighborhood and M51. Although sulfur-bearing species are known to behave in a complex manner, as described in Section 3.4.1, the CS/HCO^+ ratio seems to follow the S/O ratio (Table 3.20 and Figure 3.25). This might also be the effect of elemental abundances on molecular abundances, although we need to examine the effect of sulfur depletion onto dust grains and chemical fractionation/dilution carefully.

The CS/SO ratios are almost comparable among IC10 ($1.1^{+0.3}_{-0.4}$) and the LMC ($1.6^{+0.6}_{-0.7}$). The ratios are also comparable to that in the Galactic translucent clouds ($1.0^{+0.4}_{-0.5}$), but is lower than that of M51 P1 ($4.6^{+1.2}_{-1.8}$). The 3 sigma lower limit to the ratio in NGC6822 is > 2.9, which is likely to be similar to M51. Any significant trend due to the difference of the elemental C/O ratio is not seen in the CS/SO ratio in this study.

3.5.2 Effect of Extended Photon Dominated Regions

We calculated the abundance ratio of CCH/HCO^+ in the same way as those of HCN/HCO^+ and HNC/HCO^+. The CCH/HCO^+ ratio is higher in dwarf galaxies (NGC6822: $16.7^{+6.9}_{-5.3}$, IC10: $17.5^{+7.6}_{-5.8}$, LMC: $13.9^{+7.2}_{-5.3}$) than in the Galactic translucent clouds ($5.3^{+3.9}_{-2.4}$) by a factor of ~ 3, as shown in Figure 3.26. This enhancement of CCH in dwarf galaxies cannot be interpreted as the effect of elemental abundances. Indeed, the elemental C/O ratio is estimated to be 0.50 in NGC6822 (Esteban et al., 2014), 0.3 in IC10 (Lequeux et al., 1979; Bolatto et al., 2000), and 0.33 in the LMC (Dufour et al., 1982), while it is 0.6 in Solar neighborhood (Dufour et al., 1982) and M51 (Garnett et al., 2004). When the low C/O ratio is taken into account, the high CCH/HCO^+ ratio in dwarf galaxies is striking.

It is generally thought that CCH is abundant in the photodissociation region (PDR) illuminated by UV radiation (e.g., Pety et al., 2005; Martín et al., 2014; Ginard et al., 2015). In PDRs, C^+ is abundant, and CCH is efficiently produced from C^+ through gas-phase reactions. In low-metallicity galaxies, the extinction of the UV radiation by dust grains is expected to be less effective for a given column density of H_2 because of the lower abundance of dust grains. The PDR is thus extended deeper into molecular clouds, which would be responsible to the relatively high abundance of CCH. In the PDR, the growth of large carbon-chain molecules containing more than three carbon atoms are generally suppressed by competitive photodissociation processes (e.g., Lucas & Liszt, 2000). The c-C_3H_2/CCH ratio is indeed found to be less than 0.1 both in all three dwarf galaxies, which is lower than that observed in the Galactic translucent clouds (0.22; Turner et al., 1999, 2000). The ratio is rather consistent with the ratio in some Galactic diffuse clouds observed in absorption against the bright continuum sources (0.04; Lucas & Liszt, 2000) and the ratio in M82 which also hosts extended PDRs (0.04; Fuente et al., 2005; Aladro et al., 2015). This fact further supports the extended PDRs in cloud peripheries in dwarf galaxies.

Non-detection of CH_3OH in any dwarf galaxies is notable. We obtained the upper limits to the intensity and the column density of CH_3OH in dwarf galaxies. The abundance ratios of CH_3OH/HCO^+ are < 1.6 in NGC6822, < 2.2 in IC10, and < 0.8 in the LMC, which seem lower than that found in M51 ($3.8^{+5.8}_{-2.3}$). This result can also be interpreted in terms of a stronger UV effect owing to low abundance of dust grains in low-metallicity environments. CH_3OH is thought to be produced by hydrogenation of CO on dust grains, and is liberated into the gas phase by thermal and/or non-thermal desorption (e.g., Watanabe & Kouchi, 2002). A low abundance of dust grains tends to make the CH_3OH formation inefficient. Furthermore, laboratory experiments show that the efficiency of CH_3OH formation significantly decreases at the temperature higher than 20 K due to a fall of sticking probability of hydrogen atom (Watanabe et al., 2003). Since the temperature of cloud peripheries is

expected to be higher in the low-metallicity condition due to penetration of the UV radiation, CH_3OH would not be formed efficiently. According to Shimonishi et al. (2016), the lower abundance of CH_3OH ice observed in the LMC may be also caused by a relatively high dust temperature. Their result is consistent with ours.

We also evaluated the HNC/HCN ratio to be $0.29^{+0.11}_{-0.11}$ in NGC6822, $0.18^{+0.07}_{-0.07}$ in IC10, $0.28^{+0.11}_{-0.10}$ and in the LMC. They are lower than the ratio in typical dark clouds ($0.54 - 4.5$; Hirota et al., 1998) in the Solar neighborhood. It is close to the ratio reported in some Galactic diffuse clouds, where the HCN and HNC lines are detected in absorption against bright continuum sources (0.21 ± 0.05; Liszt & Lucas, 2001). Hirota et al. (1998) reported that the HNC/HCN ratio is lower under higher-temperature environments: the ratio decreases above 24 K, possibly reflecting isomerization mechanisms of HNC to HCN. The relatively low HNC/HCN ratios observed in IC10 and the LMC clouds may also originate from warmer temperature conditions due to higher UV field and/or lower grain abundance. In addition, it is worth noting non-detection of N_2H^+. This seems to originate mainly from the low elemental abundance of nitrogen. In addition, the UV radiation may also contribute to the low-abundance of N_2H^+. Deeper penetration of UV radiation enhances the ionization degree, which efficiently destroys N_2H^+ through the recombination reaction with an electron (Aikawa et al., 2015).

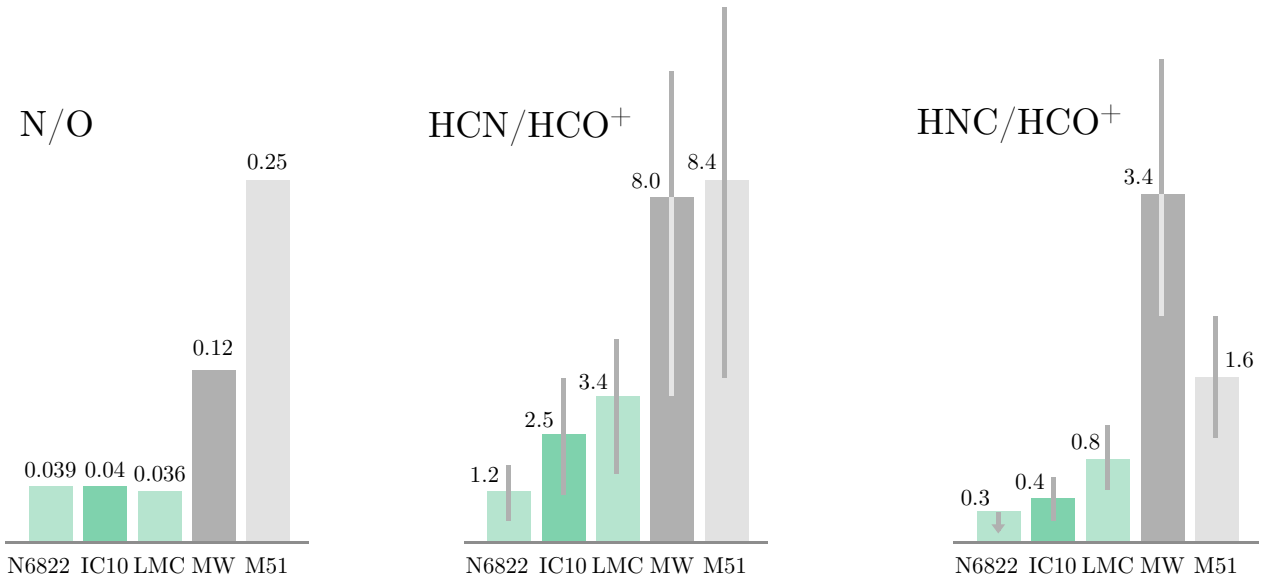

Figure 3.24 Column density ratios of HCN/HCO^+ and HNC/HCO^+ compared with the elemental abundance ratios of N/O in each galaxy. Gray lines indicate errors estimated from the variation due to the assumed gas kinetic temperature and H_2 density.

Table 3.20. Column density ratios compared with elemental abundance ratios.

		NGC6822	IC10	LMC	"Solar"	M51
Elemental abundance ratio	N/O	0.039	0.04	0.036	0.12	~ 0.25
	C/O	0.50	0.3	0.33	0.60	~ 0.6
	S/O	0.03	~ 0.03	0.043	0.023	~ 0.025
Column density ratio	N[HCN]/N[HCO$^+$]	$1.2^{+0.6}_{-0.7}$	$2.5^{+1.3}_{-1.4}$	$3.4^{+1.3}_{-1.8}$	$8.0^{+2.9}_{-4.6}$	$8.4^{+4.0}_{-4.6}$
	N[HNC]/N[HCO$^+$]	< 0.3	$0.4^{+0.2}_{-0.2}$	$0.8^{+0.3}_{-0.3}$	$3.4^{+1.3}_{-1.2}$	$1.6^{+0.6}_{-0.6}$
	N[HNC]/N[HCN]	< 0.3	$0.18^{+0.07}_{-0.07}$	$0.3^{+0.1}_{-0.1}$	$0.4^{+0.2}_{-0.2}$	$0.21^{+0.07}_{-0.07}$
	N[CCH]/N[HCO$^+$]	$16.7^{+6.9}_{-5.3}$	$17.5^{+7.6}_{-5.8}$	$13.9^{+7.2}_{-5.3}$	$5.3^{+3.9}_{-2.4}$	$9.1^{+3.8}_{-2.9}$
	N[CS] /N[HCO$^+$]	$3.5^{+0.6}_{-0.9}$	$4.0^{+0.7}_{-1.0}$	$4.2^{+0.7}_{-1.0}$	$3.4^{+0.5}_{-0.7}$	$2.3^{+0.4}_{-0.6}$
	N[CS] /N[SO]	> 2.9	$1.1^{+0.3}_{-0.4}$	$1.6^{+0.6}_{-0.7}$	$1.0^{+0.4}_{-0.5}$	$4.6^{+1.2}_{-1.8}$

Note. — Elemental abundances are of (a) H II region(s) in each galaxy based on Lequeux et al. (1979) (Oxygen and Nitrogen), Bolatto et al. (2000) (Carbon), and Magrini & Gonçalves (2009) (Sulfur) for IC10, Esteban et al. (2014) for NGC6822, Dufour et al. (1982) for the LMC and "Solar", Bresolin et al. (2004) (Oxygen, Nitrogen, and Sulfur), Garnett et al. (2004) (Carbon) for M51. Column densities are calculated for the H_2 density range of $3 \times 10^3 - 1 \times 10^5$ cm^{-3} and the gas kinetic temperature range of $10 - 50$ K. For "Solar", we took an average of nearby translucent clouds; CB17, CB24, CB228 (Turner, 1995a,b, 1996; Turner et al., 1997, 2000). We choose these clouds, because all molecules listed in this table are observed. For M51, we used the literature data reported by Watanabe et al. (2014). Note that the H_2 density is derived toward this source to be $\sim 10^4$ cm^{-3} by observations of the H_2CO lines (Nishimura et al., 2016). The errors are estimated from the variation due to the assumed gas kinetic temperature and H_2 density.

Table 3.21. Column density ratios of the observed seven clouds in the LMC.

	COP1	NQC2	N79	N44C	N11B	N113	N159W
N[HCN]/N[HCO$^+$]	$2.4^{+1.1}_{-1.3}$	$3.0^{+1.5}_{-1.7}$	$3.3^{+1.2}_{-1.8}$	$3.5^{+1.4}_{-1.9}$	$4.3^{+1.7}_{-2.4}$	$4.7^{+1.5}_{-2.5}$	$2.4^{+0.8}_{-1.3}$
N[HNC]/N[HCO$^+$]	$1.23^{+0.46}_{-0.43}$	$0.76^{+0.27}_{-0.25}$	$0.49^{+0.14}_{-0.13}$	$0.57^{+0.18}_{-0.17}$	$0.78^{+0.29}_{-0.26}$	$1.07^{+0.39}_{-0.34}$	$0.87^{+0.31}_{-0.28}$
N[HNC]/N[HCN]	$0.52^{+0.19}_{-0.17}$	$0.27^{+0.10}_{-0.11}$	$0.16^{+0.07}_{-0.06}$	$0.17^{+0.08}_{-0.07}$	$0.19^{+0.09}_{-0.07}$	$0.24^{+0.10}_{-0.08}$	$0.38^{+0.15}_{-0.13}$
N[CCH]/N[HCO$^+$]	$10.1^{+4.6}_{-3.4}$	$20.6^{+9.5}_{-6.9}$	$11.1^{+6.4}_{-4.7}$	$15.4^{+8.1}_{-5.9}$	$12.9^{+6.6}_{-4.9}$	$17.8^{+10.0}_{-7.5}$	$9.3^{+5.3}_{-3.9}$
N[CS] /N[HCO$^+$]	$7.19^{+1.74}_{-1.95}$	$2.97^{+0.46}_{-0.71}$	$2.03^{+0.21}_{-0.35}$	$4.05^{+0.58}_{-0.93}$	$4.70^{+0.82}_{-1.17}$	$4.10^{+0.47}_{-0.87}$	$4.37^{+0.65}_{-1.04}$
N[CS] /N[SO]	$1.61^{+0.49}_{-0.66}$	$0.98^{+0.28}_{-0.39}$	$1.36^{+0.44}_{-0.58}$	$1.74^{+0.61}_{-0.74}$	$2.18^{+0.80}_{-0.95}$	$1.76^{+0.81}_{-0.83}$	$1.78^{+0.78}_{-0.82}$

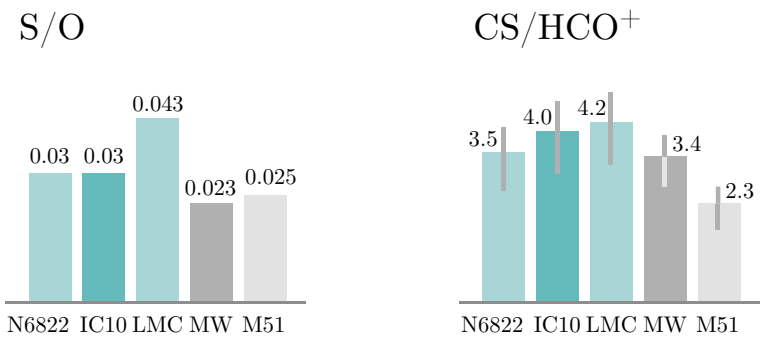

Figure 3.25 Column density ratios of CS/HCO^+ compared with the elemental abundance ratios of S/O in each galaxy. Gray lines indicate errors estimated from the variation due to the assumed gas kinetic temperature and H_2 density.

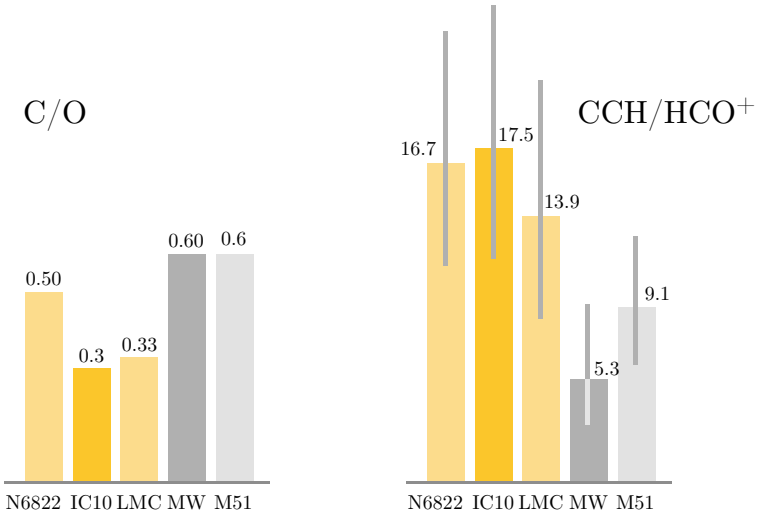

Figure 3.26 Column density ratios of CCH/HCO^+ compared with the elemental abundance ratios of C/O in each galaxy. Gray lines indicate errors estimated from the variation due to the assumed gas kinetic temperature and H_2 density.

3.6 Summary

We have characterized the molecular-cloud-scale chemical composition of the low-metallicity dwarf galaxy for the first time. That is deficient nitrogen-bearing species, enhancement of CCH, and deficient CH_3OH. The effect of the elemental abundances and that of the extended PDRs in cloud peripheries likely contributed the characteristic chemical composition. This result can be obtained by sensitive observations of faint molecular lines of the dwarf galaxies.

Chapter 4

Molecular-Cloud-Scale Chemical Composition: Galactic Cloud W3(OH)

4.1 Large-Scale Observation of Galactic Molecular Clouds

Recently, chemical compositions of nearby extragalactic objects have been studied by taking advantage of increasing sensitivity of single-dish telescopes and interferometers. Unbiased spectral line surveys at millimeter wavelengths have been conducted toward a variety of targets, including active galaxies, such as active galactic nuclei (AGNs; e.g., Aladro et al., 2013), starburst galaxies (e.g., Martín et al., 2006), and (ultra) luminous infrared galaxies ((U)LIRGs; e.g., Martín et al., 2011), as well as low-metallicity dwarf galaxies, as described in the preceding chapter. The chemical composition of each galaxy revealed by the spectral line survey is discussed in relation to a galaxy type, an evolutional stage, and physical environment. Yet, comparison between extragalactic and galactic observations requires special attention to the large difference of the size that can be resolved in their observations. Due to the limited spatial resolution, these extragalactic studies are of (a) molecular-cloud(s) scale, while we can readily resolve dense cores and star-forming regions for Galactic sources.

To fill this gap and understand the meaning of the molecular-cloud-scale chemical composition in terms of astrochemical concepts developed for Galactic sources, the mapping spectral line survey observation toward a Galactic molecular cloud is useful. By averaging the spectra over the large mapped area covering a whole molecular cloud, we can simulate the spectrum of Milky Way from a distant point of view, just as we observe it from the other galaxy. The mapping line survey will also offer us a deeper understanding of the origin of the molecular-cloud-scale chemical composition, as we can look into the spatial distribution of molecules within a cloud. With this mind, we have conducted the mapping spectral line survey observation toward the active star-forming region W3(OH). We have

revealed the molecular-cloud-scale chemical composition of W3(OH), and have found that it reflects rather diffuse parts of the cloud than dense star-forming cores.

4.2 W3(OH)

The W3 giant molecular cloud is an active star-forming cloud in the Perseus arm, which is located in the outer part of the our Galaxy (the Galactocentric distance is 9.95 kpc; Xu et al., 2006). In this cloud, the most active star-forming regions are W3 Main, W3(OH), and AFGL333 (Figure 4.1). These three star-forming regions are located in the eastern edge of the W3 giant molecular cloud. This structure is considered to be formed probably from materials swept up by the expansion of the W4 H II region (Lada et al., 1978). W3(OH), the target of this mapping survey, is a ultracompact H II region rich in OH masers (Wynn-Williams et al., 1972) and the second active star-forming region after W3 Main.

The W3 giant molecular cloud has been studied in various wavelengths in order to investigate its star-formation activities and evolutional stages. Infrared maps (70 μm, 160 μm, 250 μm, 350 μm, and 500 μm) are observed with *Herschel* (Rivera-Ingraham et al., 2013). The distributions of CO and atomic carbon were also reported (e.g., Sakai et al., 2006). The spectral line survey from 85 to 115 GHz was conducted toward several star-forming cores in the W3 giant molecular cloud (Kim et al., 2006). Hence, the W3 giant molecular cloud is considered to be one of the most favorable targets for molecular-cloud-scale chemical study. In this study, we focus on the molecular-cloud-scale chemical composition rather than the properties of the each star-forming region.

4.3 Observations

The observations were carried out with the 45 m radio telescope at Nobeyama Radio Observatory (NRO) in March in 2015. We observed the frequency ranges of $87-91$, $96-103$, and $108-112$ GHz to cover the frequencies of important molecular lines observed in external galaxies (Chapter 3). The half-power beam widths (HPBW) of the telescope are $20.2''$ and $16.1''$ at 87 and 112 GHz, respectively, which correspond to 0.19 and 0.15 pc at the distance of W3 (1.95 kpc; Xu et al., 2006), respectively. We observed two orthogonal polarization signals simultaneously by using the SIS mixer receiver (TZ1), whose system temperature ranged from 130 to 180 K. The backend is the autocorrelator SAM45. The frequency resolution and bandwidth are 488.28 kHz and 1600 MHz, respectively. The line intensity was calibrated by the chopper wheel method, and a typical calibration accuracy is 20%. The antenna temperature is divided by the main beam efficiency of 0.48 and 0.41 at 87 and 112 GHz, respectively,

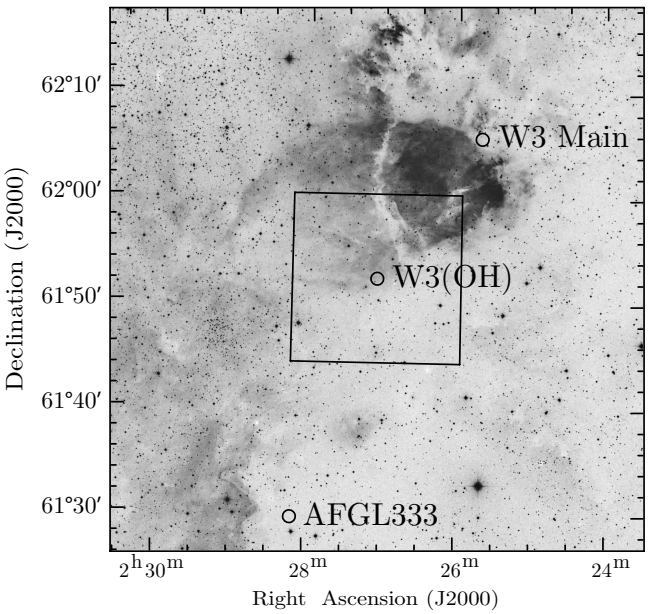

Figure 4.1 The Digitized Sky Survey image (R band; 700 nm) of the W3 giant molecular cloud. Three star-forming regions, W3 Main, W3(OH), and AFGL333, are indicated by circles. We observed the 9.0 pc × 9.0 pc area enclosed by a solid black line. The Digitized Sky Survey was produced at the Space Telescope Science Institute and the images of these surveys are based on photographic data obtained using the Oschin Schmidt Telescope on Palomar Mountain and the UK Schmidt Telescope.

to obtain the main beam temperature $T_{\rm MB}$.

We employed the On-The-Fly (OTF) mode for the mapping observation. The center position of the map is W3(OH): ($\alpha_{\rm J2000.0}$, $\delta_{\rm J2000.0}$) = ($2^{\rm h}28^{\rm m}4.0^{\rm s}$, $61^\circ52'24.0''$). The mapping area is a rectangle of $16.0' \times 16.0'$ centered at W3(OH), as shown in Figure 4.1, which corresponds to the linear scale of 9.0 pc ×9.0 pc. The grid spacing for the observation is $6''$. The total observation time was $\sim$ 20 hours. In addition to the OTF mapping, we conducted a short observation for a few minutes toward the center position with the position-switching mode. Hereafter, we refer the spectrum of this position to as a 'hot core' spectrum. For both the mapping and single-point observations, the reference position is taken as: ($\alpha_{\rm J2000.0}$, $\delta_{\rm J2000.0}$) = ($2^{\rm h}29^{\rm m}57.1^{\rm s}$, $62^\circ5'41.1''$). The telescope pointing was checked by observing the nearby SiO maser source (S Per) every hour, and the pointing accuracy was maintained to be better than $5''$.

The observation data were first reduced with the NRO software *NOSTAR* and *NEWSTAR*, and then detailed analyses were carried out by using our own codes. Although we scanned two orthogonal direction (α- and δ-direction) in the OTF mapping observation, we did not use the δ-direction data in the analyses because of poor signal-to-noise ratios due to bad weather conditions. Since we adopted a grid size of $30''$ in the analyses, the scanning effect can be ignored.

We first combined successive channels of SAM45 to improve the signal-to-noise ratio. The resultant frequency resolution is 1 MHz. A baseline of the 5th-order polynomial was subtracted from each 0.2 GHz range. We identified the observed lines with the aid of the spectral line database CDMS (Müller et al., 2001; Müller et al., 2005). For the detailed analysis of each molecular line, we made the velocity resolution to be 1 km s^{-1}, and a baseline of the 5th-order polynomial was subtracted in the narrower velocity range from -150 to 50 km s^{-1}.

4.4 Results

4.4.1 Hot-Core-Scale and Molecular-Cloud-Scale Spectra

Figure 4.2 shows the 'hot core' spectrum and the spectrum averaged over the 9.0 pc $\times$ 9.0 pc area. The lines of CCH, HCN, HCO^+, HNC, CS, SO, $C^{18}O$, and ^{13}CO are strongly detected in the both spectra. In the 'hot core' spectrum, the lines of $C^{34}S$, CH_3OH, and HC_3N are also detected with relatively high intensity. Furthermore, we identified $H^{13}CN$, $C^{33}S$, OCS, ^{34}SO, H_2CS, CH_3CCH, and CH_3CN in spite of the short integration time of a few minutes, as shown in Figure 4.3. On the other hand, even $C^{34}S$ and CH_3OH are marginally detected in the averaged spectrum, and HC_3N is absent. The spectral line profiles of individual molecular transitions are shown in Figure 4.4. The line parameters obtained by the Gaussian fitting are summarized in Table 4.1.

Generally, the line intensities of the averaged spectrum are fainter than those of the 'hot core' spectrum. However, intensity ratios of molecular lines between the 'hot core' spectrum and the averaged spectrum are different from species to species. Using HCO^+ as a reference, CCH is found to be relatively strong in the averaged spectrum, while the other species such as HCN, HNC, CS, and SO are much fainter. This fact would reflect the different distribution of each species. We will discuss this point more closely in Section 4.5.2. OCS, H_2CS, CH_3CCH, and CH_3CN are detected only in the 'hot core' spectrum. These species would mainly be distributed just around the star-forming region.

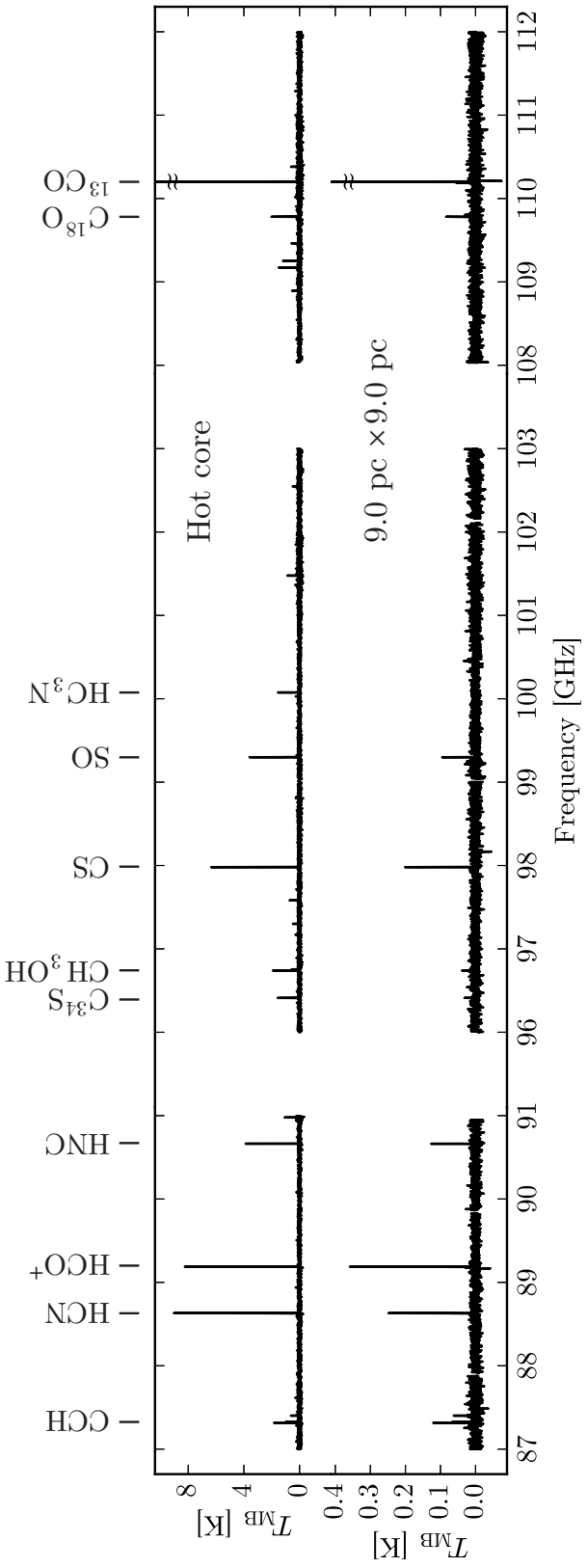

Figure 4.2 *Upper:* Spectrum of the W3(OH) hot core. *Lower:* The spectrum averaged over all the observed area (9.0 pc × 9.0 pc). The representative molecular lines are indicated on the top.

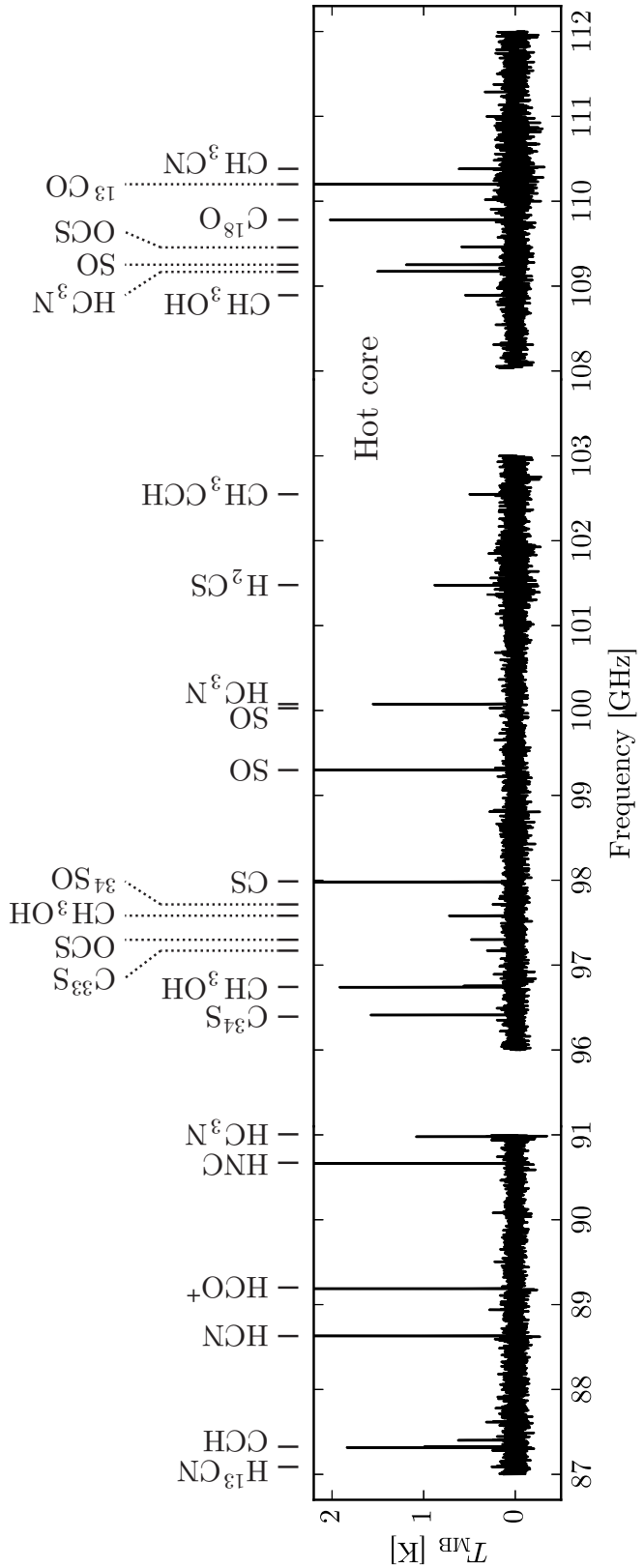

Figure 4.3 Zoomed spectrum of the W3(OH) hot core. The representative molecular lines detected are indicated on the top.

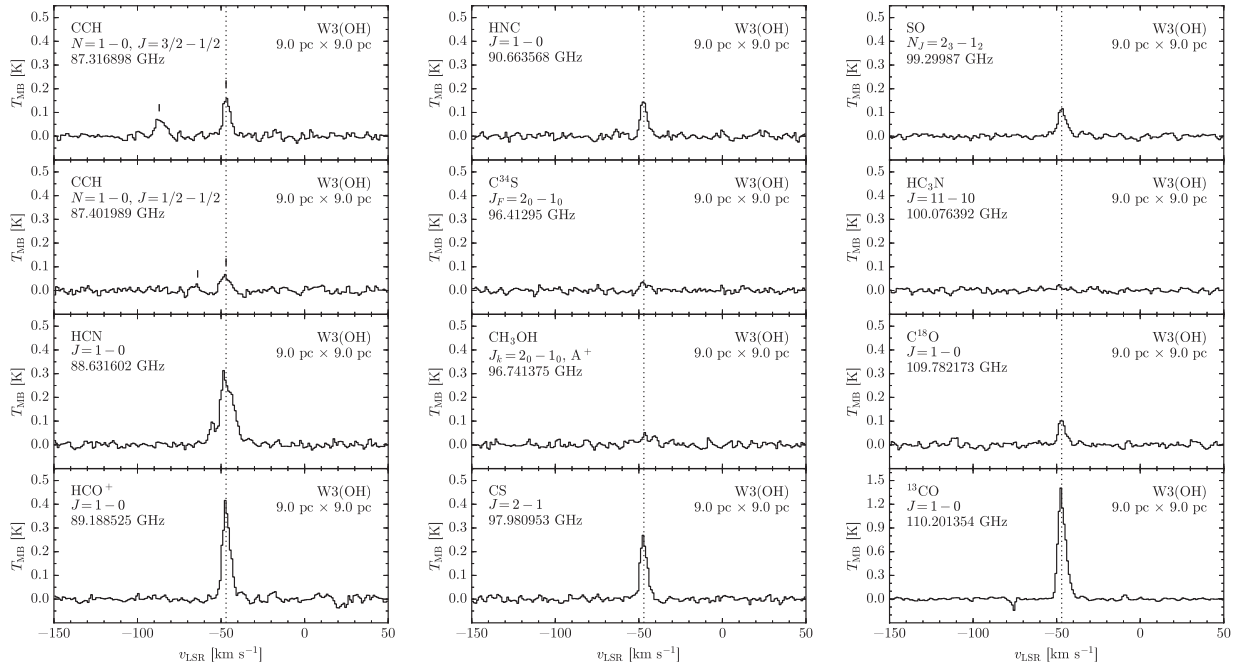

Figure 4.4 Spectral line profiles of individual molecular transitions in the spectrum averaged over the whole area (9.0 pc × 9.0 pc). The dashed line indicates the systemic velocity of -47 km s^{-1}. Small vertical lines in the CCH panel represent the positions of the hyperfine components.

Table 4.1. Line parameters of the spectrum averaged over all the observed area (9.0 pc × 9.0 pc).

Molecule	Frequency (GHz)	Transition	$T_{\rm MB}$ Peak (mK)	$v_{\rm LSR}$ (km s^{-1})	Δv (km s^{-1})	$\int T_{\rm MB} dv$ (K km s^{-1})
CCH	87.284105	$N = 1 - 0$, $J = 3/2 - 1/2$, $F = 1 - 1$				< 0.1
CCH	87.316898	$N = 1 - 0$, $J = 3/2 - 1/2$, $F = 2 - 1$	0.159 ± 0.010	-46.64 ± 0.16	5.2 ± 0.4	0.87 ± 0.02
CCH	87.328585	$N = 1 - 0$, $J = 3/2 - 1/2$, $F = 1 - 0$	0.072 ± 0.013	-46.1 ± 0.6	6.9 ± 1.5	0.52 ± 0.05
CCH	87.401989	$N = 1 - 0$, $J = 1/2 - 1/2$, $F = 1 - 1$	0.063 ± 0.006	-47.6 ± 0.3	5.9 ± 0.7	0.393 ± 0.018
CCH	87.407165	$N = 1 - 0$, $J = 1/2 - 1/2$, $F = 0 - 1$	0.026 ± 0.010	-47.7 ± 0.8	4.4 ± 2.0	0.12 ± 0.02
CCH	87.446470	$N = 1 - 0$, $J = 1/2 - 1/2$, $F = 1 - 0$				< 0.1
HCN	88.631602	$J = 1 - 0$	0.263 ± 0.006	-46.73 ± 0.12	10.7 ± 0.3	3.14 ± 0.03
HCO^+	89.188525	$J = 1 - 0$	0.381 ± 0.008	-46.85 ± 0.06	5.60 ± 0.14	2.261 ± 0.019
HNC	90.663568	$J = 1 - 0$	0.149 ± 0.007	-47.08 ± 0.11	4.6 ± 0.2	0.760 ± 0.014
$C^{34}S$	96.412950	$J_F = 2_0 - 1_0$	0.031 ± 0.005	-46.7 ± 0.5	5.7 ± 1.1	0.190 ± 0.015
CH_3OH	96.741375	$J_k = 2_0 - 1_0$, A^+	0.030 ± 0.004	-45.5 ± 0.9	14 ± 2	0.44 ± 0.03
CS	97.980953	$J = 2 - 1$	0.255 ± 0.006	-47.15 ± 0.06	4.95 ± 0.14	1.364 ± 0.013
SO	99.299870	$N_J = 2_3 - 1_2$	0.110 ± 0.004	-46.75 ± 0.12	6.2 ± 0.3	0.748 ± 0.012
HC_3N	100.076392	$J = 11 - 10$				< 0.05
$C^{18}O$	109.782173	$J = 1 - 0$	0.103 ± 0.006	-46.88 ± 0.14	5.0 ± 0.3	0.546 ± 0.014
^{13}CO	110.201354	$J = 1 - 0$	1.286 ± 0.018	-46.93 ± 0.04	5.52 ± 0.09	7.71 ± 0.04

Note. — The errors are 1σ. The upper limits are 3σ. The calibration error ($\sim 20\%$) is not included.

4.4.2 Distribution of Key Molecular Species

In order to characterize the chemical composition averaged over the 9.0 pc × 9.0 pc area, it is necessary to investigate which molecular emission comes from which part of the molecular cloud. We selected the 11 strongest lines, CCH ($N = 1 - 0$), HCN ($J = 1 - 0$), HCO^+ ($J = 1 - 0$), HNC ($J = 1 - 0$), $C^{34}S$ ($J = 2 - 1$), CH_3OH ($J_k = 2_k - 1_k$), CS ($J = 2 - 1$), SO ($J_k = 3_2 - 2_1$), HC_3N ($J = 11 - 10$), $C^{18}O$ ($J = 1 - 0$), and ^{13}CO ($J = 1 - 0$), and presented their integrated intensity maps with the $30''$ resolution, as shown in Figure 4.5. The grid size (resolution) corresponds to the spatial scale of 0.28 pc at the distance of W3 (1.95 kpc). The velocity range of integration is from -57 to -37 km s^{-1} except for HCN. For HCN, the velocity range is from -67 to -27 km s^{-1} in order to cover all the hyperfine components.

The distribution of ^{13}CO extends to the north-south direction, which is consistent with the ^{13}CO map previously reported by Sakai et al. (2006). The distribution of $C^{18}O$ is also consistent with the map by Sakai et al. (2006), in spite of the rather poor signal-to-noise ratio of our data. All the distributions including those of ^{13}CO and $C^{18}O$ have a peak at the center position. However, the degree of concentration to the center differs from species to species. We can classify the distributions into the following three types; (i) species concentrated just around the center, such as $C^{34}S$, CH_3OH, SO, and HC_3N, (ii) species loosely concentrated around the center, such as HCN, HCO^+, HNC, and CS, and (iii) species extended widely over the mapped area, such as CCH, $C^{18}O$, and ^{13}CO. Such a difference of the distributions seems to reflect chemical nature of each species under different H_2 density, temperature, and UV radiation field. Further discussions on this classification will be presented in Section 4.5.1.

4.5 Discussion on Molecular-Cloud-Scale Chemical Composition

4.5.1 Correlation between the Integrated Intensities of Molecules and the ^{13}CO Integrated Intensity

As mentioned in Section 4.4.2, the distribution is different among the observed molecular species. In order to characterize the difference, we investigate correlations between the integrated intensities of ^{13}CO and those of various molecules. Here, we employ ^{13}CO as a reference molecule, because the ^{13}CO integrated intensity would roughly represent the line-of-sight column density of H_2. Figure 4.6 shows the correlation diagrams. Each data point represents the integrated intensity averaged over a $30'' \times 30''$ (0.28 pc × 0.28 pc) area. The number of the data for the whole mapped area ($16' \times 16'$) is consequently 1024 in total. Note that the typical error of each data point is 2 K km s^{-1} (3σ).

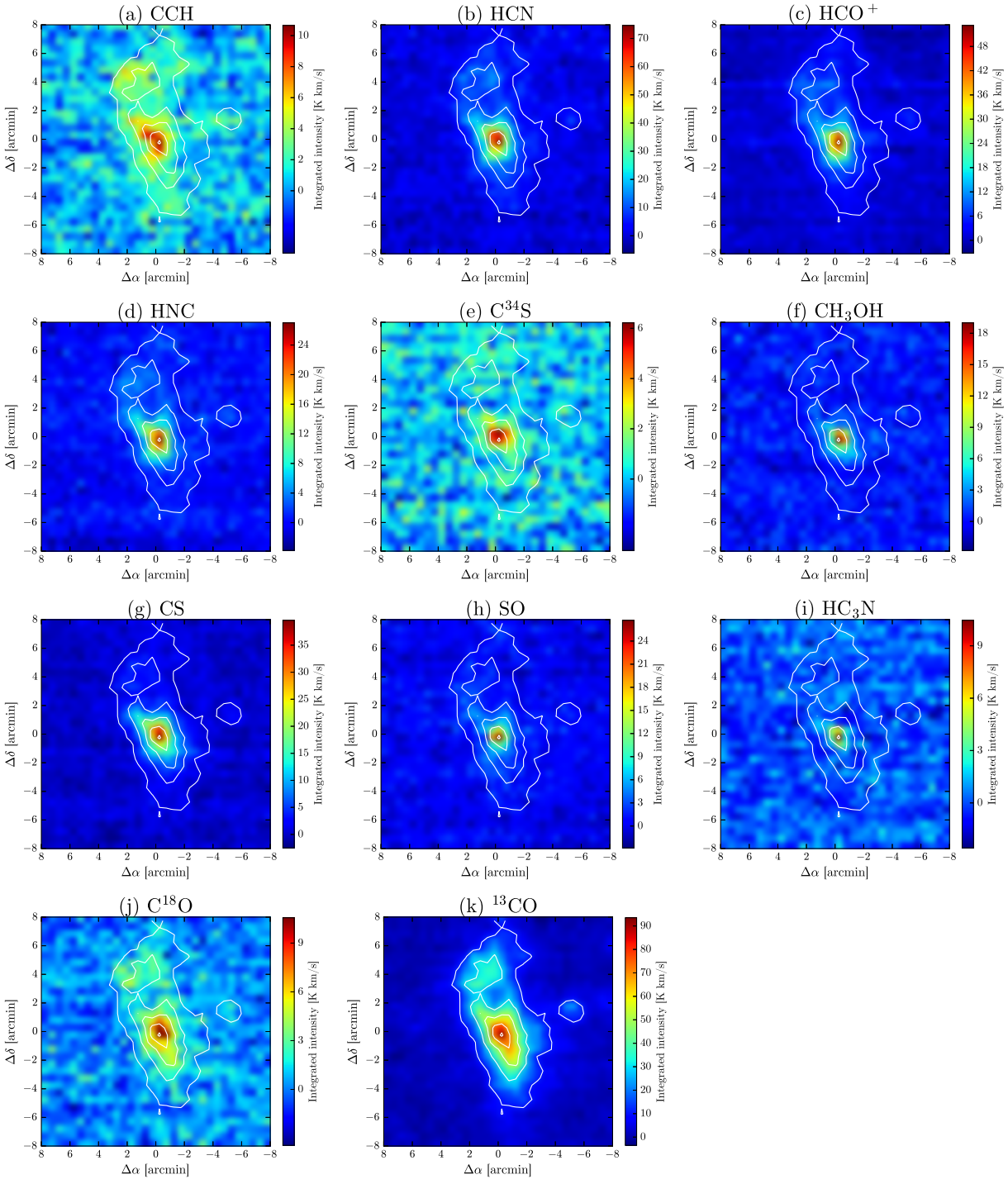

Figure 4.5 Integrated intensity maps of the bright emission lines. The coordinates ($\Delta\alpha$, $\Delta\delta$) are the offset from W3(OH). The images are convolved to the 30″ resolution. The velocity range of integration is from -57 to -37 km s^{-1} except for HCN. For HCN, the velocity range is from -67 to -27 km s^{-1} to cover all the hyperfine components. White contours indicate the ^{13}CO integrated intensity. The coutour levels are from 10 to 90 K km s^{-1}, with the interval of 20 K km s^{-1}.

Roughly speaking, all the diagrams show positive correlation. However, the dependence of the integrated intensity on the ^{13}CO column density is different from molecule to molecule, as inferred from the variation of the molecular distributions. As shown in Figures 4.6f and 4.6i, the integrated intensities of CH_3OH and HC_3N seem to have an appearance threshold at the ^{13}CO integrated intensity of about 40 K km s^{-1} and 60 K km s^{-1}, respectively. The integrated intensities of C^{34}S and SO gradually increase as increasing ^{13}CO integrated intensity, and then steeply increase for the ^{13}CO integrated intensity higher than 60 K km s^{-1} (Figures 4.6e and 4.6h). These behaviors are consistent with the fact that the above four molecular species, CH_3OH, HC_3N, C^{34}S, and SO, are mainly concentrated around the hot core (Figure 4.5).

The integrated intensities of HCN, HCO^+, HNC, and CS increases as increasing ^{13}CO integrated intensity more steeply than those of C^{34}S and SO for the ^{13}CO integrated intensity below 40 K km s^{-1} (Figures 4.6b, 4.6c, 4.6d, and 4.6g). However, their dependence on the ^{13}CO integrated intensity is not linear, but seems to have a knee point at the ^{13}CO integrated intensity about $40-60$ K km s^{-1}, above which the dependence becomes steeper. Similarity of these four species in their dependence on the ^{13}CO integrated intensity indicate their similar spatial distribution, as shown in Figure 4.5.

On the other hand, the integrated intensities of C^{18}O and CCH increase almost linearly as increasing ^{13}CO integrated intensity (Figures 4.6a and 4.6j). The linear correlation between C^{18}O and ^{13}CO means that the ^{13}CO line is not optically very thick. In fact, the ^{13}CO/C^{18}O ratio is approximately 10, which is consistent with the ^{13}C/^{18}O ratio. Hence, it is confirmed that the rapid increase of the integrated intensities of various molecules for the ^{13}CO integrated intensity higher than $40-60$ K km s^{-1} does not mean the saturation of the ^{13}CO line. CCH also shows a linear correlation with ^{13}CO, although the signal-to-noise ratio is not very good. This result suggests that CCH is widely distributed over the molecular cloud as ^{13}CO.

In order to confirm the above results, similar correlation diagrams are prepared against the HCO^+ integrated intensity instead of the ^{13}CO integrated intensity (Figure 4.7). The integrated intensities of HCN, HNC, and CS are linearly correlated well, where the correlation coefficient is higher than 0.8 (Figures 4.7b, 4.7c, and 4.7f). This result again verifies similar distributions of HCO^+, HCN, HNC, and CS. The integrated intensities of CH_3OH, SO, and HC_3N seem to have a knee point at the HCO^+ integrated intensity of $20-30$ K km s^{-1}, as seen as the appearance threshold in the correlation diagram with ^{13}CO (Figures 4.7e, 4.7g, and 4.7h). A similar trend is marginally seen for C^{34}S (Figure 4.7d) in spite of the poor signal-to-noise ratio. On the other hand, the CCH and C^{18}O emissions appear even for the low HCO^+ integrated intensity (Figure 4.7a and 4.7i). Considering the typical error of 2 K km s^{-1}, the CCH and C^{18}O emissions at the low HCO^+ integrated intensity are significant.

Low integrated intensities of molecular lines in the low ^{13}CO integrated intensity area do not mean their small contribution to the large-scale spectrum. The emission from the extended gas with the low ^{13}CO integrated intensity is certainly faint, but the spatial area of such regions is much larger than that of the star-forming core. When we accumulate the contributions of the extended parts, the total contribution cannot be ignored in the averaged spectrum. In the following section, we examine the contribution of the extended gas component as well as star-forming cores by classifying the observed area into 5 sub-regions according to the ^{13}CO integrated intensity.

4.5.2 5 Sub-Regions and Their Characteristics

What does the spectrum averaged over the molecular cloud represent? To address this question, we classified the mapped area into 5 sub-regions according to the ^{13}CO integrated intensity $I(^{13}\mathrm{CO})$. A criterion for the classification is summarized in Table 4.2. This criterion is just arbitrary, but is set every 20 K km s^{-1}, considering the highest $I(^{13}\mathrm{CO})$ of 93.5 K km s^{-1}. As a result, the sub-regions (A−E) are shown in Figure 4.8. The sub-region A is just located around the center, while sub-regions B, C, and D surround it in this order, extending along north-south direction. The sub-region E is the other remaining part.

Then, we prepared a spatially averaged spectrum of each sub-region. They are shown in Figure 4.9. The average integrated intensities of each sub-region are summarized in Table 4.3. We see the spectral lines of CCH, HCN, HCO$^+$, HNC, CS, SO, C^{18}O, and ^{13}CO in the spectra of all the sub-regions, but with different relative intensities. In the sub-region E, HNC, SO, and C^{18}O are quite faint, and the spectrum is rather similar to the spectrum averaged over the whole area. On the other hand, molecular species seen in the 'hot core' spectrum, such as H_2CS, CH_3CCH, and OCS, are also detected in the spectrum of the sub-region A. The lines of these species become fainter in the sub-regions B and C in this order, and finally fade out in the sub-region D.

We closely compared the relative intensity ratio of the lines of the key molecular species: CCH, HCN, HCO$^+$, HNC, C^{34}S, CH_3OH, CS, SO, HC_3N, C^{18}O, and ^{13}CO, and investigated their variation among 5 sub-regions. For this comparison, we use the HCO$^+$ line, which is the second brightest after the ^{13}CO line, as reference, because it traces moderately denser regions ($n_{H_2} \gtrsim 10^4$ cm^{-3}) than the ^{13}CO line, where the lines of the above molecules can be excited sub-thermally. As seen in Figure 4.9, the intensity ratios of almost all the species relative to HCO$^+$ become low from the sub-region A to the sub-region E in this order. The only exception is CCH. The CCH/HCO$^+$ ratio becomes higher in the sub-region E. Note that the CS/HCO$^+$ and C^{18}O/HCO$^+$ ratios are highest at the sub-region B. This is puzzling, but may be caused by the effect of optically thickness and/or the chemical effect

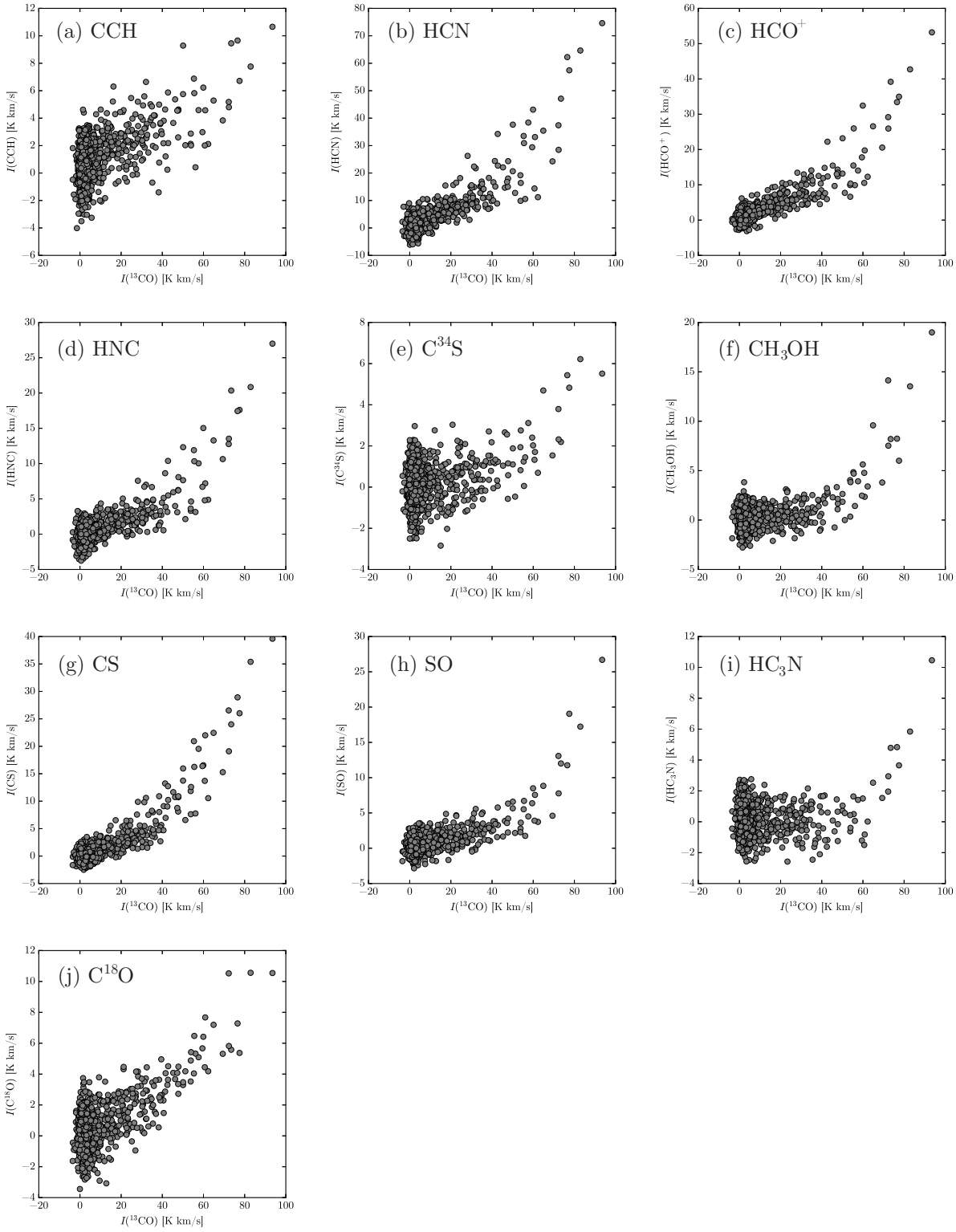

Figure 4.6 Correlation diagrams of integrated intensities of various molecules against that of ^{13}CO. The velocity range of integration is from -57 to -37 km s^{-1} except for HCN. For HCN, the velocity range is from -67 to -27 km s^{-1} to cover all the hyperfine components. Typical error of each point is ± 2 K km s^{-1} (3σ).

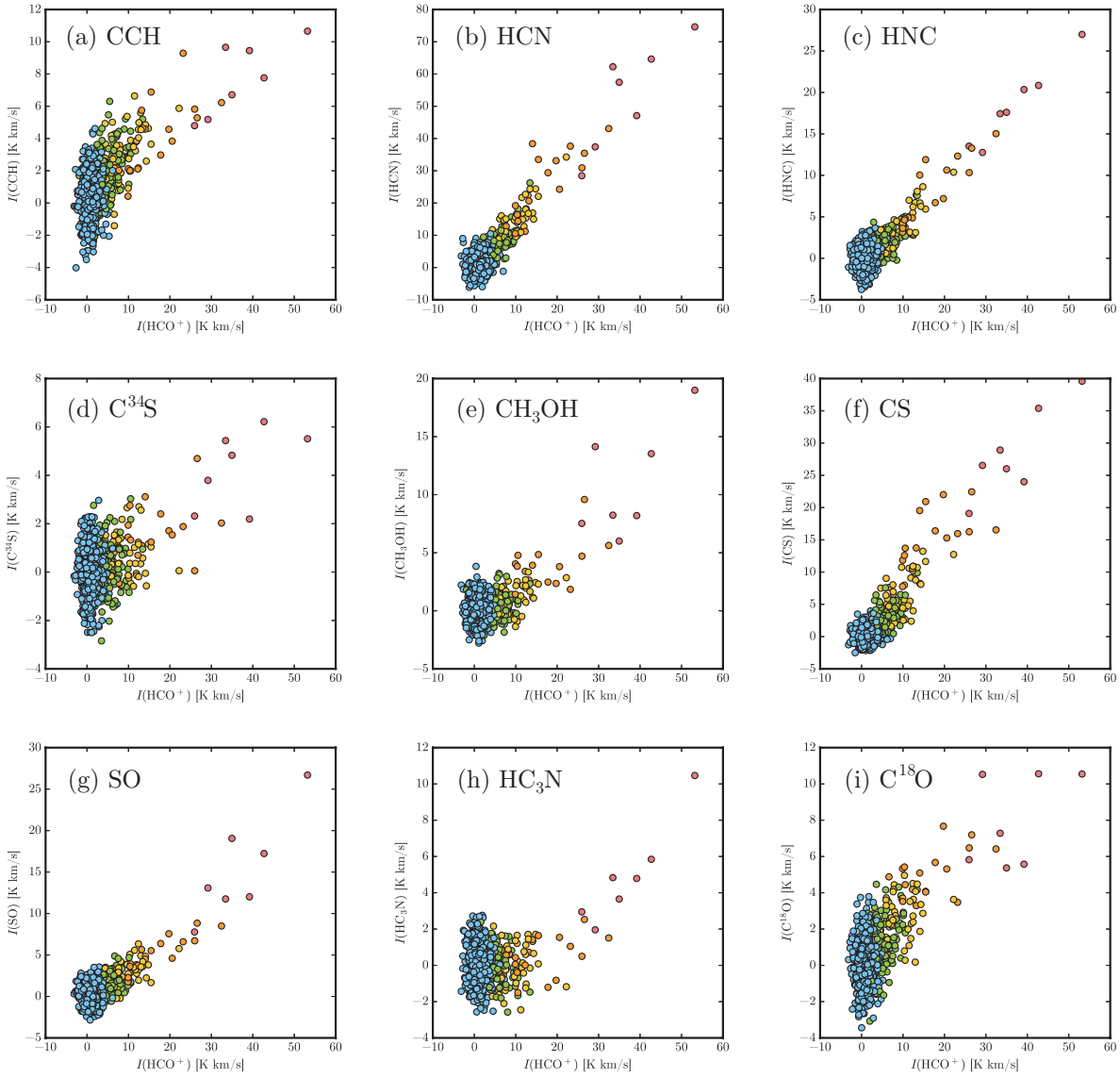

Figure 4.7 Correlation diagrams of integrated intensities of various molecules against that of HCO^+. The colors correspond to the sub-regions classified by the integrated intensity of ^{13}CO. The velocity range of integration is from -57 to -37 km s^{-1} except for HCN. For HCN, the velocity range is from -67 to -27 km s^{-1} to cover all the hyperfine components. Typical error of each point is ± 2 K km s^{-1} (3σ).

such as photodissociation nearby the star-forming core.

The relatively high CCH/HCO^+ ratio in the outer regions is obviously related to the widespread distribution of CCH. As mentioned in Chapter 3, CCH is considered to be abundant in a photon dominated region (PDR), because PDR is rich in C^+ from which CCH is efficiently produced in the gas phase. PDRs are extended in cloud peripheries where the visual extinction is low, and hence, CCH can be relatively abundant in the outer part of the cloud.

In Figure 4.9, we found some differences in the intensities of HCN, HCO^+, HNC, and CS, among the 5 sub-regions, although they look similar in Figures 4.5 and 4.6. The intensities of these 4 species similarly behave in the sub-regions A−D. HCN, HNC, and CS lines become fainter relative to the HCO^+ line from the sub-region A to the sub-region D. In the sub-region E, the intensity of the HNC line is just faint, while the HCN, HCO^+, and CS lines are still seen. The excitation effect does not seem responsible for the faintness of HNC in the sub-region E. The critical density, n_{crit}, of HCN (1.0×10^6 cm^{-3} at 10 K) is actually higher than that of HNC (2.8×10^5 cm^{-3} at 10 K), as shown in Table 4.4. HNC seems to be more deficient than HCN in the sub-region E, probably because of the formation and destruction processes. It is worth noting that HNC is less stable than HCN, and hence, HNC is known to be isomerized into HCN under a high temperature condition (> 24 K; Hirota et al., 1998). This is related to the lower HNC/HCN ratio in the low-metallicity dwarf galaxies than in dense molecular clouds in the Solar-neighborhood (Section 3.5.2). The detections of CCH, HCN, HCO^+, and CS in the sub-region E indicate that the contribution of the extended gas is not small in the averaged spectrum.

For further examination of the contribution of the extended gas, we prepared Figure 4.10, which reveals a fraction of the flux of each sub-region relative to the total flux of the spectrum averaged over the whole area. This fractional flux is defined as:

$$\text{Fractional Flux} = \frac{\sum_{i \in \mathrm{R}} I_i(\mathrm{X})}{\sum_{i \in \mathrm{All}} I_i(\mathrm{X})} \times 100\%, \tag{4.1}$$

where I_i(X) stands for the integrated intensity of a given molecule for the i-th $30'' \times 30''$ area and R represents the sub-regions A, B, C, D, and E. "All" means the all observed area. Likewise, the fractional area is defined as a number of the grids belong to a given sub-region divided by the total number of the grids.

In Figure 4.10, we confirm that the contribution of the sub-region A is small for all the molecular species. In particular, the flux of CCH mostly comes from the outer sub-region D and E. It is surprising that more than 1/3 flux of CH_3OH, SO, and HC_3N come from the sub-region E, although the emissions of these species look concentrated around the hot core, as seen in the Figure 4.5. On the other hand,

Table 4.2. The criteria for the classification of sub-regions in W3(OH).

Sub-region	I(^{13}CO) (K km s^{-1})	number of data points	Area (arcmin^2)
A	> 70	7	1.75
B	$50 - 70$	17	4.25
C	$30 - 50$	49	12.25
D	$10 - 30$	132	33.00
E	< 10	819	204.75

the contribution of the sub-region E is less than 10 % for the total flux of HNC. This species is really deficient in the cloud peripheries.

For ^{13}CO and C^{18}O, 80 % and 76 % of the fluxes, respectively, come from sub-regions C, D, and E. This means that these sub-regions cover about 80 % of the total mass of the cloud. It should be noted that 3/4 of the total flux of the averaged spectrum comes from these sub-regions for most of the observed molecules.

HC_3N is a fundamental member of carbon-chain molecules, and is likely formed by gas-phase reactions starting from C^+ as in the case of like CCH. Considering that CCH is relatively abundant in the outer sub-regions, it is possible that HC_3N exists in PDRs. The low-level emissions of CH_3OH and SO extended in cloud peripheries are notable, because these species are often thought as good tracers of shocks associated with star formation. However, these molecules are also known to reside in cold dark clouds such as TMC-1 and L1544 (e.g., Takakuwa et al., 2003; Bizzocchi et al., 2014), although their emissions are not as bright as those in star forming regions. Hence, accumulation of such weak emissions over a large area would make a significant contribution to the spectrum averaged over the whole area of W3(OH). This result gives an important implication for interpretation of the emissions of these molecules observed in external galaxies.

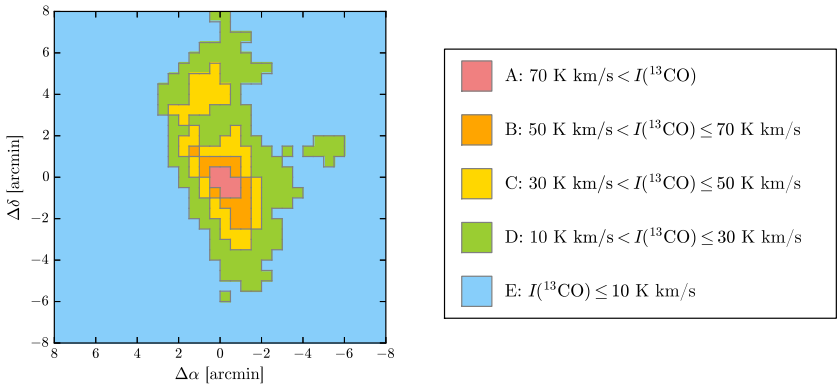

Figure 4.8 Map of the 5 sub-regions in W3(OH) classified by the ^{13}CO integrated intensity.

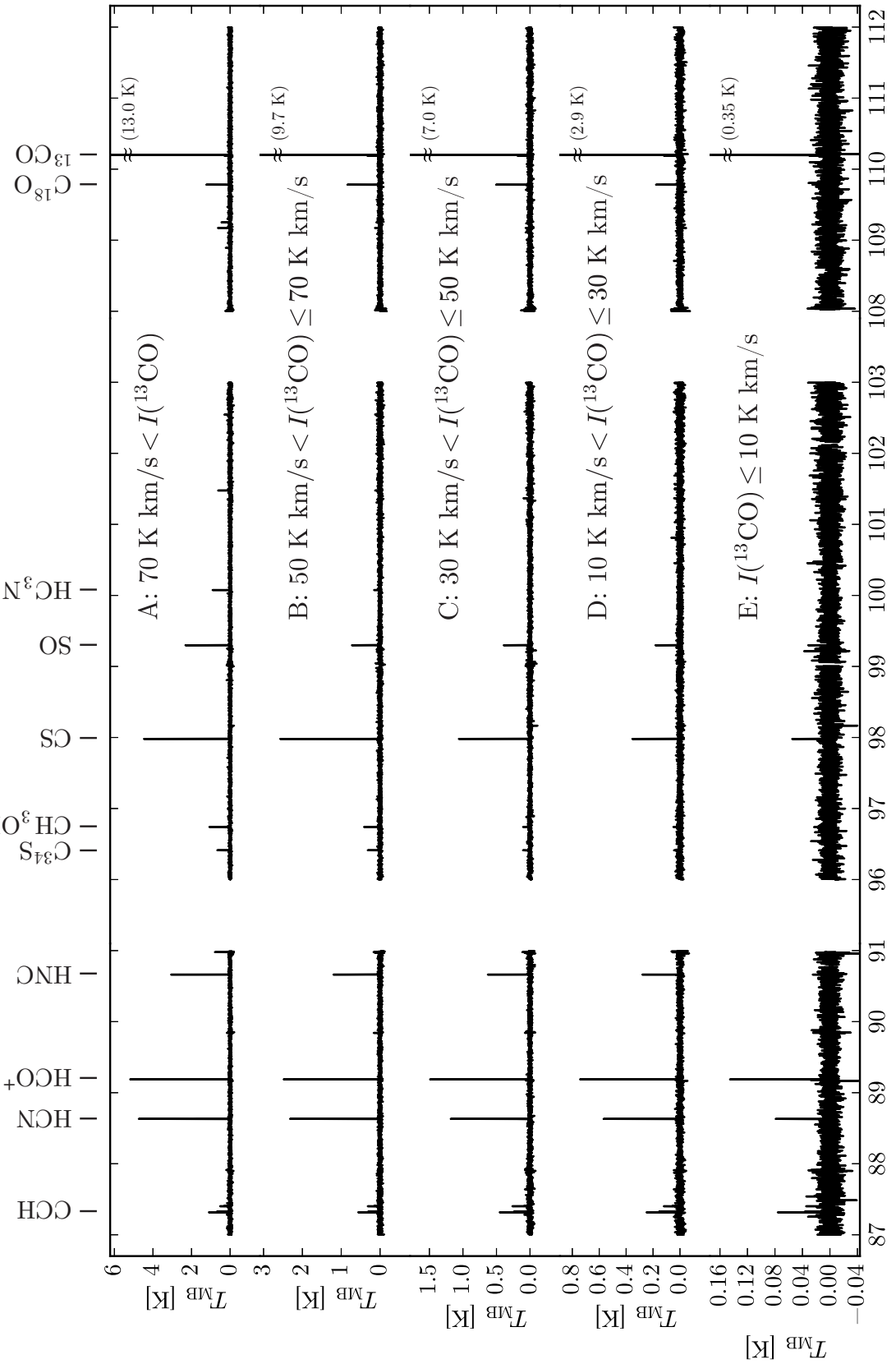

Figure 4.9 Spectra averaged for sub-regions A, B, C, D, and E in W3(OH).

4.5.3 Comparison with Other Sources

Giant Molecular Cloud W51

As an independent work, Watanabe et al. (2016) presented the mapping spectral line survey toward the Galactic molecular cloud W51. Star-formation activities of W51 is much higher than that of W3(OH). The size of W51 is larger than W3(OH), and hence, the mapped area of W51, 65 pc × 79 pc, is larger than that for W3(OH) (9.0 pc × 9.0 pc). The mapped area and the sub-regions classified by the ^{13}CO integrated intensity of W51 is shown in Figure 4.11. Figure 4.12 shows the spectra averaged for each sub-region, while Figure 4.13 shows fractional fluxes of each species and fractional area for 5 sub-regions in W51. In spite of the large difference in the star-forming activity, the cloud size, and the location in the Milky Way, we found similarity of the large-scale spectrum averaged over the large area (Figure 4.2 *lower* and Figure 4.12f) and the distributions of key molecular species between W3(OH) and W51.

In the spatially averaged spectrum of W51 (Figure 4.12f), the lines of *c*-C_3H_2, CCH, HCN, HCO^+, HNC, N_2H^+, CH_3OH, CS, SO, $C^{18}O$, ^{13}CO, and CN are detected. All molecular species are also identified in the spatially averaged spectrum of W3(OH) (Figure 4.2 *lower*) except for *c*-C_3H_2, N_2H^+ and CN, which were not covered in the present frequency settings. Furthermore, the spectral intensity pattern of W51 is similar to that of W3(OH) as a whole. Figure 4.14 shows a correlation diagram of integrated intensity ratios of CCH, HCN, HNC, $C^{34}S$, CH_3OH, CS, SO, $C^{18}O$, and ^{13}CO relative to HCO^+ between W3(OH) and W51. Indeed, the correlation coefficient is 0.96 for the 10 species: CCH, HCN, HCO^+, HNC, $C^{34}S$, CH_3OH, CS, SO, $C^{18}O$, ^{13}CO. Even if ^{13}CO is excluded, it is as high as 0.85.

The similarity of the large-scale spectra of W51 and W3(OH) is further confirmed, when we look at the spectra of sub-regions and fractional fluxes. The characteristics discussed in Section 4.5.1 and 4.5.2 are also the case of W51. CCH is relatively bright in the outer region of the cloud, while the other molecular species become faint relative to HCO^+ there.

The minor difference is seen in the sub-region spectra of HCN and $C^{18}O$. In the case of W51, their intensity ratios relative to HCO^+ are highest in the spectrum of the sub-region C, while, in W3(OH), their intensity ratios decrease toward the outer region. The possible reason is the effect of optical thickness, arbitrariness of classification of the sub-region, and/or photodissociation nearby the star-forming core. In spite of such a small difference, we stress that the chemical composition characteristic to the local star-forming cores is mostly smeared out in the molecular-cloud-scale chemical composition. Therefore, molecular-cloud-scale chemical compositions are essentially the same for the both sources.

Table 4.3. Average integrated intensities of molecular lines in each sub-region and the whole observed area.

Molecule	Frequency [GHz]	Transition	A (K km s^{-1})	B (K km s^{-1})	C (K km s^{-1})	D (K km s^{-1})	E (K km s^{-1})	9.0 pc × 9.0 pc averaged (K km s^{-1})
CCH	87.316898	$N = 1 - 0$						
		$J = 5/2 - 3/2$						
		$F = 2 - 1$	7.7 ± 0.3	4.05 ± 0.17	3.11 ± 0.10	2.06 ± 0.06	0.52 ± 0.02	0.95 ± 0.02
HCN	88.631602	$J = 1 - 0$	53.1 ± 0.3	24.7 ± 0.2	13.63 ± 0.13	6.57 ± 0.08	1.11 ± 0.03	3.16 ± 0.03
HCO^+	89.188525	$J = 1 - 0$	36.9 ± 0.3	16.25 ± 0.15	9.37 ± 0.09	4.81 ± 0.05	0.98 ± 0.02	2.373 ± 0.019
HNC	90.663568	$J = 1 - 0$	18.5 ± 0.2	7.74 ± 0.14	3.81 ± 0.08	1.67 ± 0.05	0.08 ± 0.02	0.712 ± 0.018
$C^{34}S$	96.412950	$J_F = 2_0 - 1_0$	4.33 ± 0.18	1.66 ± 0.12	0.72 ± 0.07	0.26 ± 0.04	0.027 ± 0.018	0.148 ± 0.016
CH_3OH	96.741375	$J_k = 2_0 - 1_0$, A^+	10.9 ± 0.2	3.51 ± 0.14	1.08 ± 0.08	0.45 ± 0.05	0.22 ± 0.02	0.422 ± 0.018
CS	97.980953	$J = 2 - 1$	28.51 ± 0.19	14.69 ± 0.13	6.10 ± 0.08	2.49 ± 0.05	0.415 ± 0.019	1.383 ± 0.017
SO	99.299870	$N_J = 2_3 - 1_2$	15.37 ± 0.18	5.01 ± 0.11	2.71 ± 0.07	1.34 ± 0.04	0.326 ± 0.017	0.751 ± 0.015
HC_3N	100.076392	$J = 11 - 10$	4.93 ± 0.16	0.44 ± 0.10	0.01 ± 0.06	0.09 ± 0.04	0.104 ± 0.015	0.136 ± 0.014
$C^{18}O$	109.782173	$J = 1 - 0$	8.0 ± 0.2	5.09 ± 0.13	2.62 ± 0.08	1.26 ± 0.05	0.190 ± 0.019	0.578 ± 0.017
^{13}CO	110.201354	$J = 1 - 0$	78.4 ± 0.2	57.36 ± 0.14	36.80 ± 0.08	18.19 ± 0.05	2.68 ± 0.02	7.740 ± 0.019

Note. — The velocity interval of integration is from -57 to -37 km s^{-1} except for HCN.

For HCN, the velocity interval is from -67 to -27 km s^{-1} to cover all the hyperfine components.

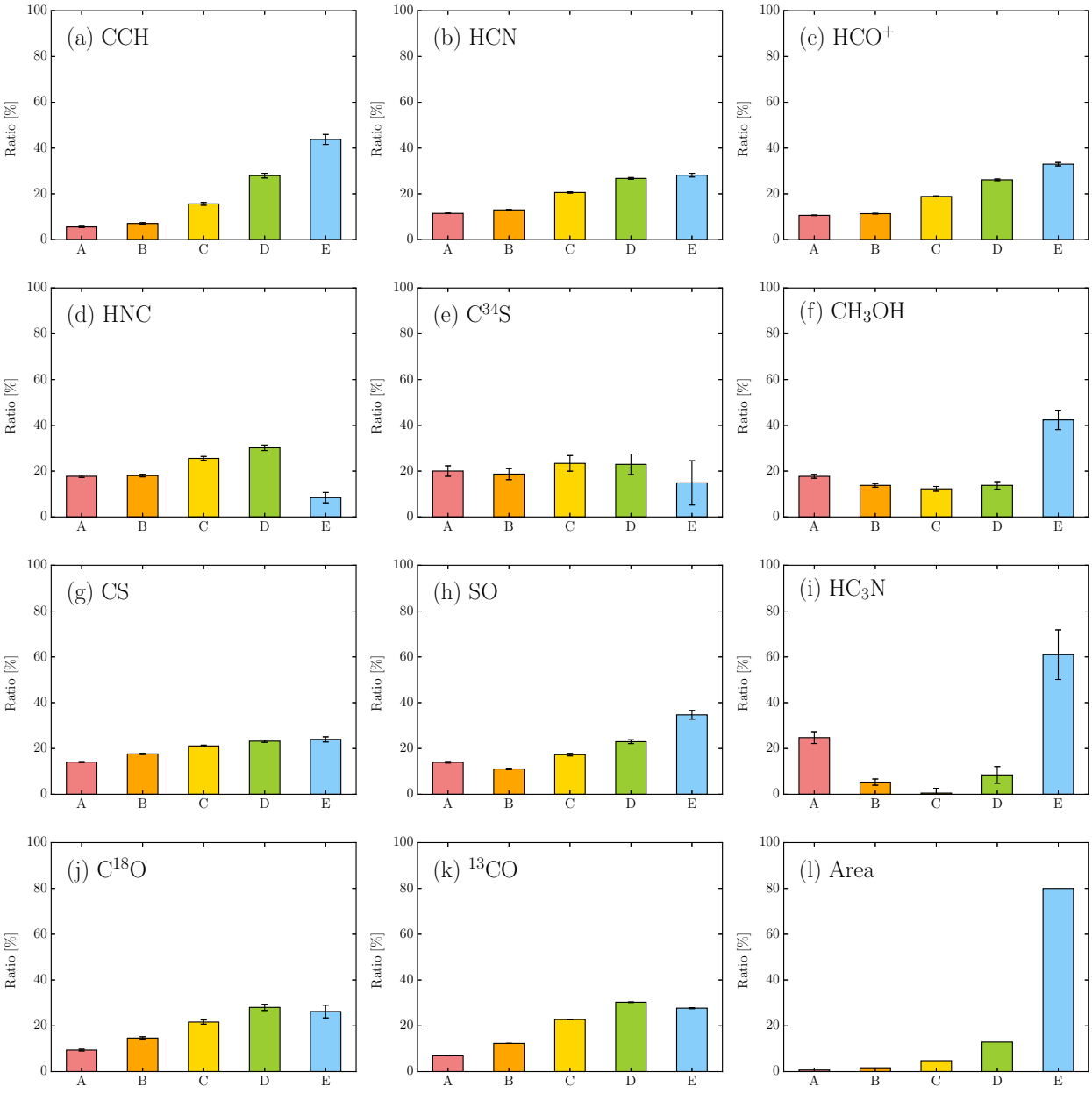

Figure 4.10 (a)-(k) Fractional fluxes of each species and (l) fractional area for 5 sub-regions in W3(OH). Black lines indicate errors (1σ). Sub-regions are classified by ^{13}CO integrated intensity: A: $>$ 70 K km s^{-1}, B: 50 $-$ 70 K km s^{-1}, C: 30 $-$ 50 K km s^{-1}, D: 10 $-$ 30 K km s^{-1}, E: $<$ 10 K km s^{-1}.

Table 4.4. The critical density and upper state energy of key molecular species.

Molecule	Frequency (GHz)	Transition	E_u (K)	n_{crit} at 10 K (cm^{-3})	n_{crit} at 100 K (cm^{-3})
CCH	87.316898	$N = 1 - 0$, $J = 5/2 - 3/2$, $F = 2 - 1$	4.2	1.21×10^5	1.94×10^5
HCN	88.631602	$J = 1 - 0$	4.3	1.01×10^6	2.66×10^6
HCO^+	89.188525	$J = 1 - 0$	4.3	1.64×10^5	2.36×10^5
HNC	90.663568	$J = 1 - 0$	4.4	2.77×10^5	4.12×10^5
CH_3OH	96.741375	$J_k = 2_0 - 1_0$, A^+	7.0	3.10×10^4	3.83×10^4
CS	97.980953	$J = 2 - 1$	7.1	3.32×10^5	3.84×10^5
SO	99.299870	$N_J = 2_3 - 1_2$	9.2	···	2.95×10^5
HC_3N	100.076392	$J = 11 - 10$	28.8	8.83×10^5	···
$C^{18}O$	109.782173	$J = 1 - 0$	5.3	1.90×10^3	1.80×10^3
^{13}CO	110.201354	$J = 1 - 0$	5.3	1.91×10^3	1.80×10^3

Note. — The critical density n_{crit} is derived by A_{ij}/C_{ij}, where A_{ij} is an Einstein A-coefficient and C_{ij} is a collisional rate coefficient. These are adopted from the LAMDA database (van der Tak et al., 2007) with C_{ij}: CCH: Spielfiedel et al. (2012); HCN and HNC: Dumouchel et al. (2010); HCO^+: Flower (1999); CH_3OH: Rabli & Flower (2010); CS and SO: Lique et al. (2006); HC_3N: Green & Chapman (1978); $C^{18}O$ and ^{13}CO: Yang et al. (2010). For $C^{34}S$, the rates are not available on the LAMDA.

Low-Metallicity Dwarf Galaxies

Figure 4.15 shows the correlation diagrams of integrated intensities of CCH, HCN, HNC, CS, SO, and ^{13}CO relative to HCO^+ between W3(OH) and the low-metallicity dwarf galaxies the LMC N44C and IC10. The correlation coefficients are 0.86 and 0.90 for the LMC and IC10, respectively. If ^{13}CO is excluded, they are 0.64 and 0.46 for the LMC and IC10, respectively. It is confirmed that the lower abundance of nitrogen-bearing species, HCN and HNC, is significant in the dwarf galaxies.

The Other Important Molecular Species: *c*-C_3H_2, N_2H^+, and CN

Although the frequency ranges of $87 - 91$, $96 - 103$, and $108 - 112$ GHz are covered in our spectral line survey, lines of some important molecular species in the 3 mm-band, *c*-C_3H_2 ($2_{12} - 1_{01}$, 85.338894 GHz), N_2H^+ ($J = 2 - 1$, 93.173392 GHz), and CN ($N = 1 - 0$, 113.123370 GHz and 113.144157 GHz) are not included in these frequency ranges. These three species are observed and detected in W51. We briefly remark on these species, based on the result of W51.

According to the result of W51, N_2H^+ behaves just like HNC in the spectra of each sub-region. Indeed, the fractional flux of N_2H^+ is quite similar to that of HNC. It seems that N_2H^+ does not exist abundantly in peripheries of molecular clouds. Although the intensity of *c*-C_3H_2 is relatively faint, it is notable that fractional flux of *c*-C_3H_2 is quite similar to that of CCH. Since *c*-C_3H_2 is formed by

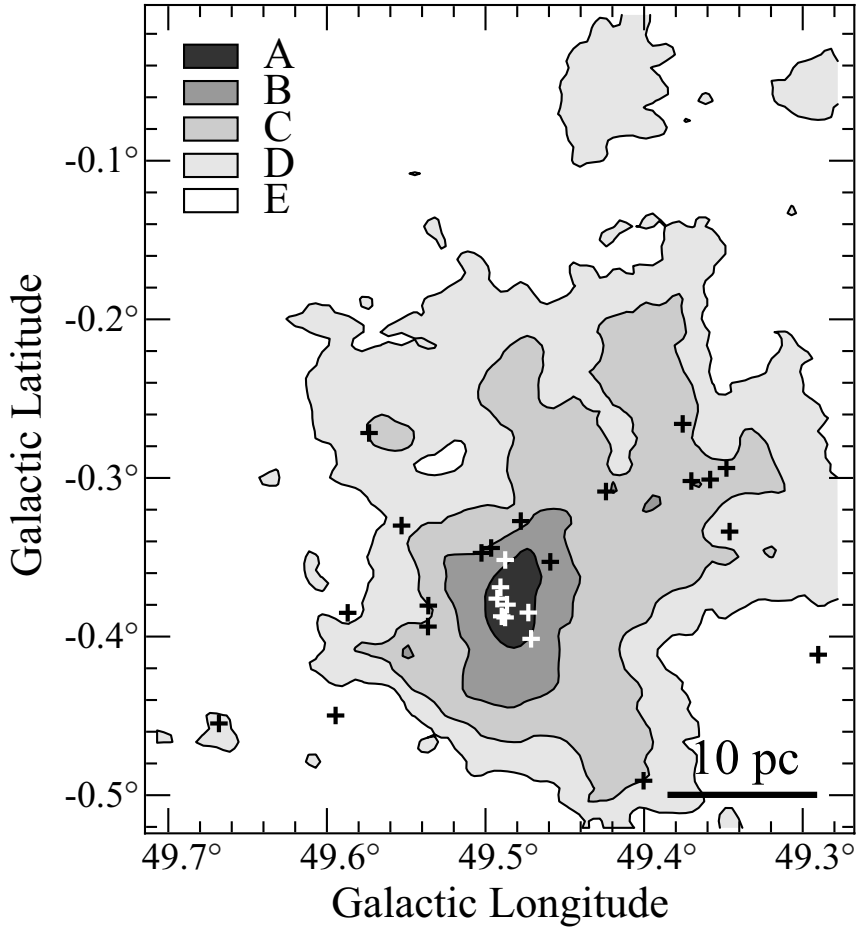

Figure 4.11 Map of W51 taken by Watanabe et al. (2016). The 5 sub-regions are classified by the ^{13}CO integrated intensity; A: $>$ 200 K km s^{-1}, B: 100 $-$ 200 K km s^{-1}, C: 50 $-$ 100 K km s^{-1},D: 25 $-$ 50 K km s^{-1}, E: $<$ 25 K km s^{-1}.

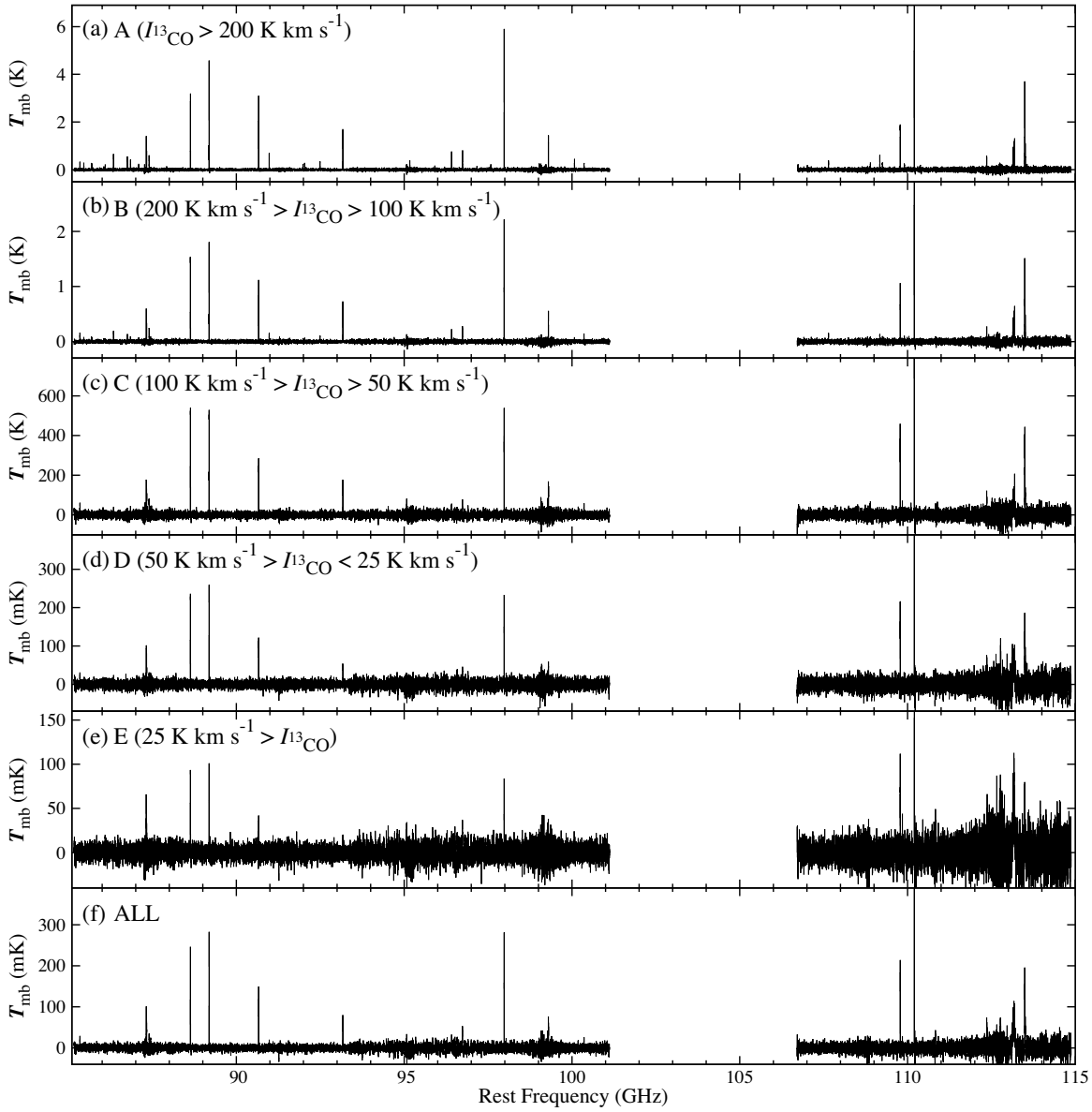

Figure 4.12 Spectra averaged for sub-regions A, B, C, D, and E in W51, taken from Watanabe et al. (2016).

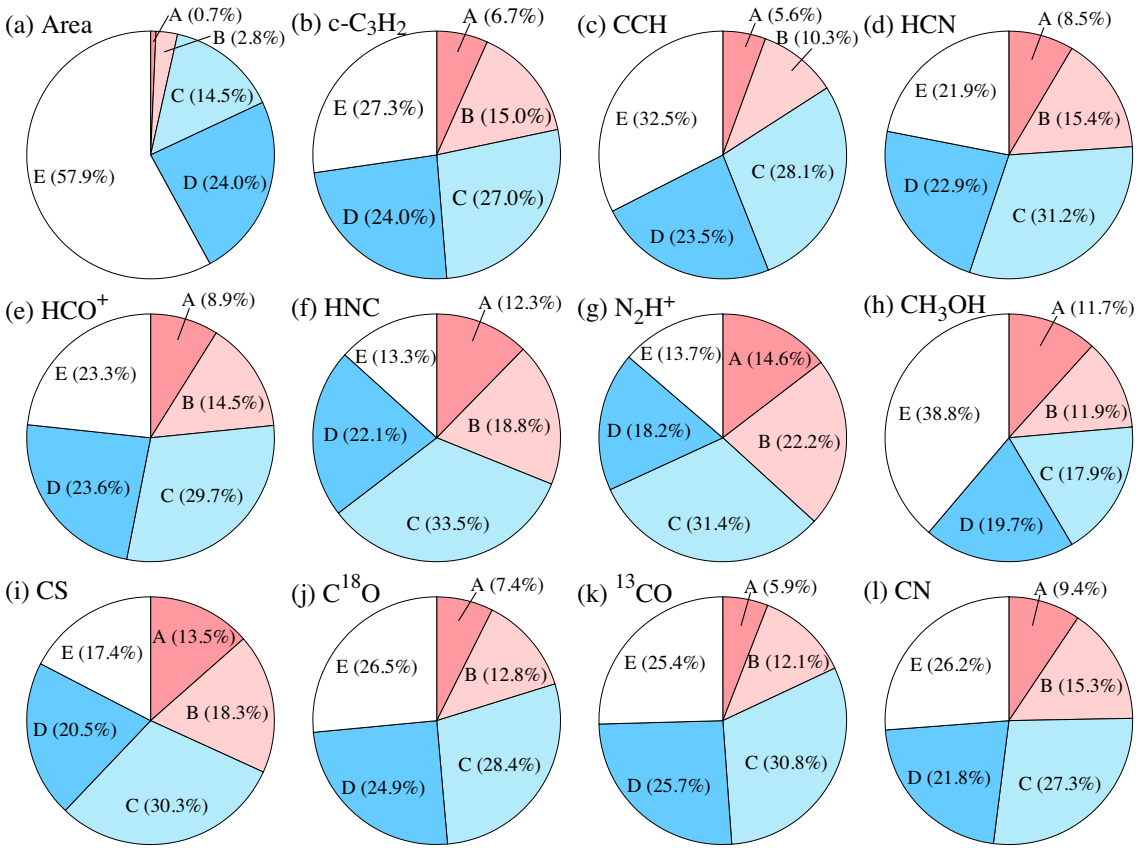

Figure 4.13 Fractional fluxes of each species and fractional area for 5 sub-regions in W51, taken from Watanabe et al. (2016).

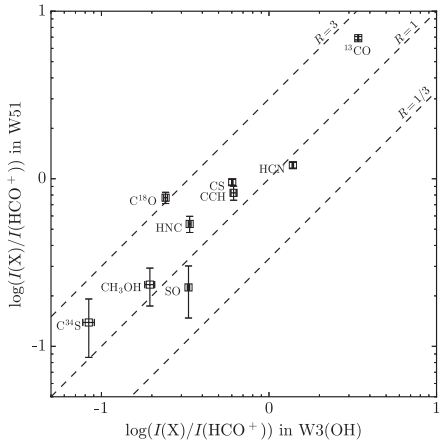

Figure 4.14 Correlation diagram of the integrated intensity ratios relative to that of HCO^+ between W3(OH) (averaged over the 9.0 pc × 9.0 pc area) and W51 (averaged over the 65 pc × 79 pc area). The data for W51 is taken from Watanabe et al. (2016). Dashed lines indicate the ratios (R) of 3, 1, 1/3.

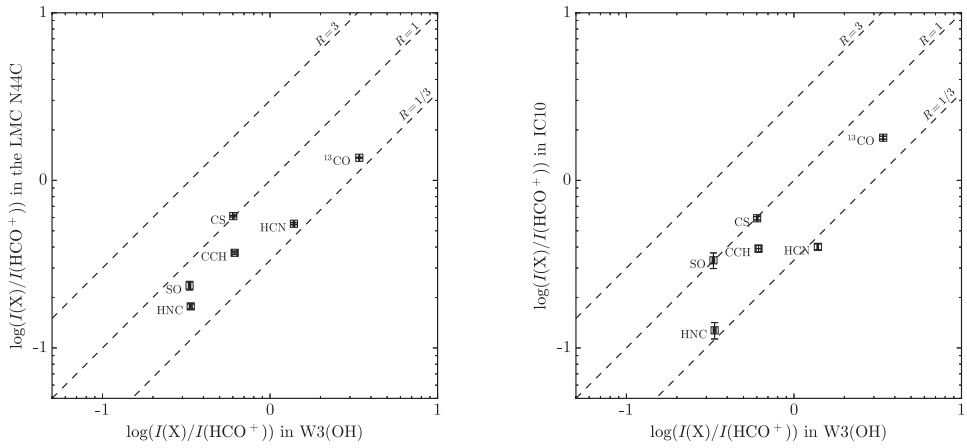

Figure 4.15 Similar to Figure 4.14, correlation diagrams of the integrated intensity ratios relative to that of HCO^+ between W3(OH) (averaged over the 9.0 pc × 9.0 pc area) and the LMC (*left*) and between W3(OH) and IC10 (*right*). Dashed lines indicate the ratios (R) of 3, 1, 1/3.

C^+ like CCH, its distribution is possibly similar to that of CCH. Furthermore, CN, which is much brighter than c-C_3H_2 and CCH, also behaves similarly to CCH. CN is efficiently formed in PDRs (e.g., Fuente et al., 1993), as in the case of CCH.

4.6 Summary

We have conducted the mapping spectral line survey toward the W3(OH) molecular cloud. We have found that the molecular-cloud-scale spectrum averaged over the all observed area is much different form the spectrum toward the hot core of W3(OH). We have evaluated the contributions of the flux of each molecule from the five sub-regions, and have found that the contribution from the less dense parts in the cloud peripheries is dominant in the molecular-cloud-scale spectrum. This result constitutes an important base for detailed understandings of chemical compositions of external galaxies.

Chapter 5

Meaning of Molecular-Cloud-Scale Chemical Composition

5.1 The Molecular-Cloud-Scale Spectrum

When we observe nearby external galaxies located at a few Mpc, a typical beam size of currently available single-dish telescopes ($20'' - 40''$) corresponds to a few 100 pc. Even for the nearest external galaxy (LMC), it corresponds to 10 pc. The size of a molecular cloud is generally $1 - 10$ pc, while that of a dense star-forming core is 0.1 pc. Hence, the spectra observed in extragalactic studies with single-dish telescopes reflect chemical composition averaged over (a) molecular cloud(s). This situation is also true for interferometric observations of external galaxies except for the LMC and the SMC.

In Section 3, we have presented the spectral line surveys toward the LMC, IC10, and NGC6822. The beam size of these spectral line surveys corresponds to the linear resolution of 10, 80, and 60 pc, respectively. Although their sizes are different, the spectral patterns are found to be similar to one another. It has been revealed that the spectral patterns in the 3 mm band are also similar among much more distant galaxies with Solar metallicity. Aladro et al. (2015) reported the spectral line survey observation in the 3 mm band toward 8 nearby active galaxies, including starburst galaxies (M83, M82, and NGC253), galaxies hosting an active galactic nuclei (M51, NGC1068, and NGC7469), and ultra-luminous infrared galaxies (Arp220 and Mrk231). The distance to these galaxies range from 3.5 Mpc to 170 Mpc. Aladro et al. (2015) discuss differences of molecular line ratios among the galaxies to extract physical characteristics of each galaxy. Such detailed studies of molecular line ratios are indeed interesting, as we may be able to see the effect of starburst, AGN, large-scale shocks, or intense interstellar radiation field from a viewpoint of chemical compositions. However, we have to notice that the strongly detected lines are almost similar among any kinds of galaxies. As discussed in Chapter

3, the spectra observed in external galaxies are those averaged over molecular clouds, and the effects of local star-formation activities are smeared out.

To obtain the molecular-cloud-scale spectrum of our Galaxy, we have conducted mapping line survey observations toward the Galactic molecular cloud W3(OH), as presented in Section 4. We have found that the spectrum averaged over a whole molecular cloud is dominated by the contribution from cloud peripheries rather than star-forming cores. By observing a whole molecular cloud within a single beam, the effect of local star formation activities is confirmed to be weakened or smeared out, and hence, molecular-cloud-scale observations offer us novel information on the chemical composition specific to the observed galaxy or that affected by galactic scale gas dynamics. Hence, it is of fundamental importance to establish the "standard" molecular-cloud-scale chemical composition toward a rather "quiescent" part of galaxies without significant effects of peculiar physical conditions (i.e., AGNs and starbursts), and to explore its meaning.

Then, can we constrain physical conditions responsible for the molecular-cloud-scale spectra? To some extent, we can suppose a part of them such as density and temperature from the observational data and under the analogy of well-studied Galactic sources. In this Chapter, we discuss the meaning of the molecular-cloud-scale chemical compositions in more detail with the aid of chemical model calculations.

5.2 Constraints on Physical Conditions of Molecular Clouds

5.2.1 Chemical Models and Intensity Calculations

We conducted model calculations with a chemical network, and derived the fractional abundances of 12 molecular species: C_3H_2, CCH, HNCO, HCN, HCO^+, HNC, N_2H^+, CH_3OH, CS, SO, CN, and CO, all of which are often detected in nearby active galaxies. This is a collaborative work with Dr. Nanase Harada of Academia Sinica Institute of Astronomy and Astrophysics (ASIAA). The model is based on the chemical network consisting of 1574 species and 122496 reactions (Harada et al., 2016). This is a gas-grain model, where gas-phase reactions and grain surface reactions are considered. So called "quasi time dependent" calculations are carried out, where a temporal variation of a chemical composition is calculated under the constant H_2 densities and the constant temperature. The Solar elemental abundances are assumed. As for the initial condition, the chemical composition of the diffuse cloud is employed: Hydrogen is in the molecular form (H_2), and all the heavy elements exist as atoms or ions depending on their ionization potential (N and O are neutral, while the others are ions). Far-ultraviolet radiation field (G_0; ratio relative to Habing's value; Habing, 1968) is assumed to

be 1. This model simulates the chemical evolution from the time when the UV radiation is shielded. Although the cloud will eventually collapse by self-gravity, its density and temperature are kept almost constant during the most of the time toward the collapse. This justifies the above simple assumption on the physical conditions.

The model calculations were conducted for a fairly extensive range of 6 parameters, H_2 density (n_{H_2}), gas temperature (T_{gas}), dust temperature (T_{dust}), visual extinction (A_v), X-ray/cosmic-ray ionization rate (ζ), abundance of sulfur atoms (S_{elem}), and evolutionary time (t), as listed in Table 5.1. Here, we assume that $T_{gas} = T_{dust}$. Since the H_2 density is moderately high and the UV radiation is not very strong, the gas and the dust would likely be well thermalized. These parameters are independent of one another. Among them, n_{H_2}, $T_{gas}(= T_{dust})$, and A_v are the most important parameters characterizing the physical conditions of molecular clouds. A high X-ray/cosmic-ray ionization rate is often suggested for diffuse clouds (McCall et al., 2002), and hence, we examined this possibility nu increasing it by a factor of 10 from the conventional value (10^{-17} s^{-1}). the sulfur abundance is also important not only for reproducing the abundances of sulfur-bearing molecules, but also for controlling the ionization degree of molecular clouds. The number of the models is 216 in total.

We prepared the spectral intensity pattern in the 3 mm band based on the fractional abundance calculated by the models. Assuming the H_2 column density of 10^{22} cm^{-3}, we first calculated the column densities of above molecular species. Then, we prepared the spectral intensity patterns of $85 - 116$ GHz from the column densities by using the non-LTE radiative transfer code RADEX (van der Tak et al., 2007). For simplicity, the line width is assumed to be 1 km s^{-1} for the all molecular species. Although the line width of 1 km s^{-1} seems to be somewhat narrow for external galaxies, we do not think that this would seriously affect the analysis, because we use integrated intensities for comparison with the observational data. We calculated 15 emission lines for 12 species listed in Table 5.2.

Here, we assumed the total H_2 column density of 10^{22} cm^{-2}, which corresponds to the cloud size of $0.1 - 1$ pc depending on the H_2 number density. We also repeated the calculations with the H_2 column density of 10^{21} cm^{-2}, and confirmed that the characteristic results in the following sections are not changed significantly.

5.2.2 Comparison with the Observed Spectral Pattern

To investigate the effect of each parameter listed in Table 5.1, we compared 216 line intensity patterns with the integrated intensities reported for the spiral arm position (P1) of M51 (Watanabe et al., 2014), which is shown in Figure 5.1. We used the data of P1 in M51 for comparison, because it is in the normal spiral arm and is not affected by AGN activity or starburst. Moreover, the metallicity of

Table 5.1. Parameters of the model calculations.

Parameters		Values
$n_{\rm H_2}$	H_2 density	3×10^3, 1×10^4, 3×10^4 cm^{-3}
$T_{\rm gas}$	Gas temperature	10, 20, 30 K
$T_{\rm dust}$	Dust temperature	10, 20, 30 K (assumed to be $T_{\rm gas}$=$T_{\rm dust}$)
G_0	Far-ultraviolet radiation field	1 (fixed; relative to Habing's value)
$A_{\rm v}$	Visual extinction	2, 4, 10 mag
ζ	X-ray/Cosmic-ray ionization rate	10^{-17}, 10^{-16} s^{-1}
$\rm S_{elem}$	Abundance of sulfur atoms	8×10^{-8}, 8×10^{-7}
t	Evolutionary time	10^5, 10^6 yr

Table 5.2. Molecular lines employed for comparison with the observational data.

Species	Transition	Frequency [GHz]
C_3H_2	$2_{12} - 1_{01}$	85.33889
CCH	$N = 1 - 0$, $J = 5/2 - 3/2$	87.31690
CCH	$N = 1 - 0$, $J = 3/2 - 3/2$	87.40199
HNCO	$4_{04} - 3_{03}$	87.92524
HCN	$1 - 0$	88.63160
HCO^+	$1 - 0$	89.18840
HNC	$1 - 0$	90.66357
N_2H^+	$1 - 0$	93.17370
CH_3OH	$2_0 - 1_0$, A^+	96.74137
CS	$2 - 1$	97.98095
SO	$N_J = 2_3 - 1_2$	99.29987
HNCO	$5_{05} - 4_{04}$	109.90576
CN	$N = 1 - 0$, $J = 1/2 - 1/2$	113.16867
CN	$N = 1 - 0$, $J = 3/2 - 1/2$	113.49492
CO	$1 - 0$	115.27120

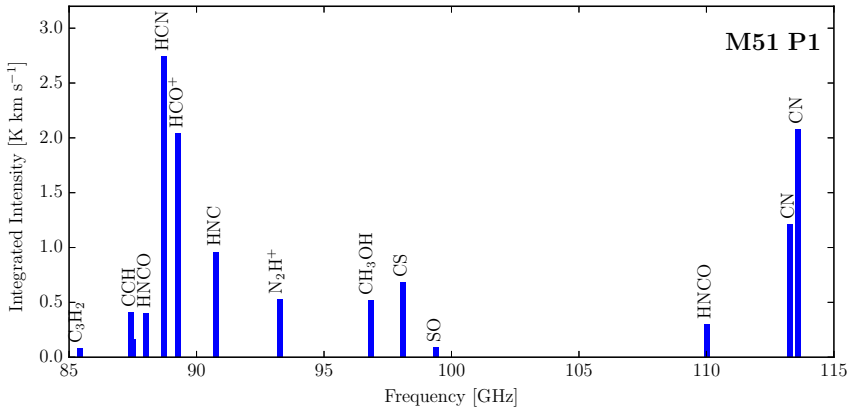

Figure 5.1 The intensity pattern of the spiral arm position (P1) of M51. Note that the vertical axis is the integrated intensity.

M51 is known to be similar to our Galaxy. We calculated the correlation coefficient r as:

$$r = \frac{\sum_i (I_i^{\rm cal.} - \overline{I^{\rm cal.}})(I_i^{\rm obs.} - \overline{I^{\rm obs.}})}{\sqrt{\sum_i (I_i^{\rm cal.} - \overline{I^{\rm cal.}})^2 \cdot \sum_i (I_i^{\rm obs.} - \overline{I^{\rm obs.}})^2}}, \tag{5.1}$$

where $I^{\rm cal.}$ and $I^{\rm obs.}$ denote the integrated intensity of model calculations and that observed toward M51, respectively, and i stands for each molecular line. $\overline{I}$ means the average of the integrated intensities of all molecular species. In the comparison of the spectral intensity pattern, we excluded the CO line, because the intensity of CO is much higher than those of the other species, and therefore, it would cause fake correlations. In addition to the correlation coefficients, we examined the intensity patterns by eyes.

We found that the calculated spectral intensity pattern reproduces the observed spectral intensity pattern of M51 fairly well, when the model parameters are $\zeta = 10^{-17}$ s^{-1}, $S_{\rm elem} = 8 \times 10^{-8}$, $t = 10^5$ yr. For a fair comparison, the correlation coefficients are shown by a color diagram shown in Figure 5.2. The red blocks, which mean correlation coefficients higher than 0.6, are found in various parts of the diagram. Among them, the correlation is better for the visual extinction of 4 mag and 10 mag than 2 mag. This means that molecular clouds need to be moderately shielded from the interstellar UV radiation. When the visual extinction is 2 mag, the interstellar UV radiation well penetrates molecular clouds. Then, CCH, which is efficiently produced in photodissociation regions, tend to be too abundant. As for the H_2 density, the correlations are slightly better for the 3×10^3 cm^{-3} and 1×10^4 cm^{-3} cases than for the H_2 density of 3×10^4 cm^{-3} case. In the 3×10^4 cm^{-3} case, HCO^+ tends to be overabundant. In contrast to the visual extinction and the H_2 density, the temperature does not affect the correlation very much, although the temperature of 30 K makes HCO^+ slightly

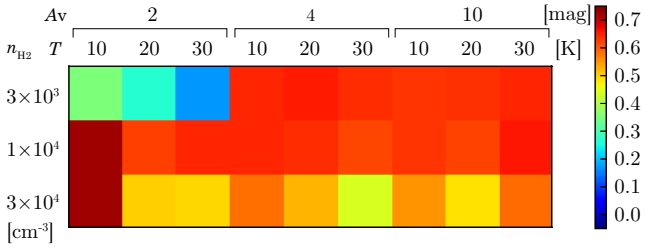

Figure 5.2 The color diagram of correlation coefficients with parameters $\zeta = 10^{-17}$ s^{-1}, $S_{elem} = 8 \times 10^{-8}$, $t = 10^5$ yr.

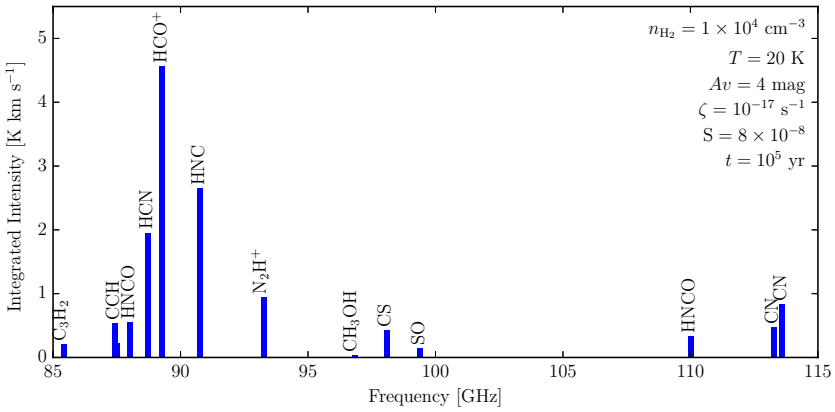

Figure 5.3 The intensity pattern, which shows one of the best correlations, with the parameters shown in the upper right.

overabundant. Figure 5.3 is the intensity pattern of $n_{H_2} = 1 \times 10^4$ cm^{-3}, $T = 20$ K, $A_v = 4$ mag, $\zeta = 10^{-17}$ s^{-1}, $S_{elem} = 8 \times 10^{-8}$, and $t = 10^5$ yr, which shows an example of the best correlations.

We evaluated the effect of X-ray/cosmic-ray ionization rate ζ on the spectrum. Figure 5.4 is the color diagram of $\zeta = 10^{-16}$ s^{-1}, $S_{elem} = 8 \times 10^{-8}$, and $t = 10^5$ yr. Note that the sulfur abundance S_{elem} and the evolutionary time t are taken to be the same as those for Figure 5.2. Under these conditions, the correlations are relatively good, when the H_2 density is 3×10^3 cm^{-3} and the visual extinction is 4 mag or 10 mag, as shown in Figure 5.4. However, Figure 5.2 generally shows better correlations.

In addition to the effect of the X-ray/cosmic-ray ionization rate ζ, we also studied the effect of the sulfur abundance S_{elem}. Figure 5.5 shows the case for $\zeta = 10^{-17}$ s^{-1}, $S_{elem} = 8 \times 10^{-7}$, $t = 10^5$ yr. The cosmic-ray ionization rate ζ and the evolutionary time t are taken to be the same as Figure 5.2. Although, relatively good correlations can be found for the H_2 density of $3 \times 10^3 - 1 \times 10^4$ cm^{-3} and the visual extinction of 4 mag or higher, they are not as good as the lower sulfur abundance (8×10^{-8}).

Finally, we investigated the effect of the evolutionary time t. This time corresponds to the time from the start of the chemical reactions, when the all the heavy atoms were in the atomic or ionic

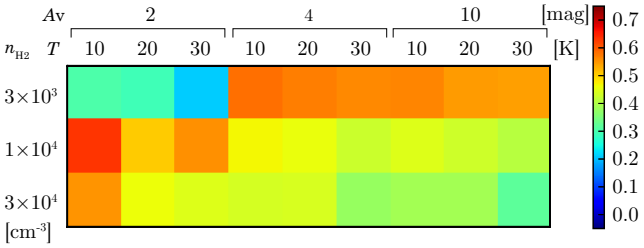

Figure 5.4 The color diagram of correlation coefficients with parameters $\zeta = 10^{-16}$ s^{-1}, $S_{elem} = 8 \times 10^{-8}$, $t = 10^5$ yr.

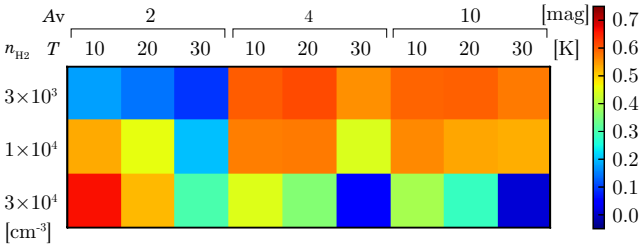

Figure 5.5 The color diagram of correlation coefficients with parameters $\zeta = 10^{-17}$ s^{-1}, $S_{elem} = 8 \times 10^{-7}$, $t = 10^5$ yr.

forms. This start time corresponds to the time when the UV radiation was shielded. Figure 5.6 shows the case of $t = 10^6$ yr, where the X-ray/cosmic-ray ionization rate ζ and the sulfur abundance S_{elem} are taken as the same as those for Figure 5.2. In this case, the correlations are notably worse than Figure 5.2. Almost all of the blocks show the correlation coefficients lower than 0.6. Hence, the evolutionary time t seems to be much more sensitive to the chemical composition than X-ray/cosmic-ray ionization rate ζ and the sulfur abundance S_{elem}. This suggests that the observed intensity patterns reflect the chemical composition of "chemically young" molecular clouds.

The most critical reason for the worse correlation at 10^6 yr than at 10^5 yr is the enhancement of N_2H^+ and SO. Both N_2H^+ and SO are so-called "late-type molecules", which take a longer time to

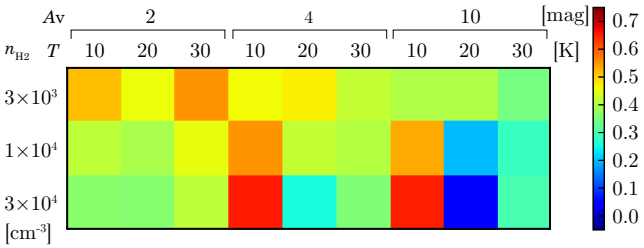

Figure 5.6 The color diagram of correlation coefficients with parameters $\zeta = 10^{-17}$ s^{-1}, $S_{elem} = 8 \times 10^{-8}$, $t = 10^6$ yr.

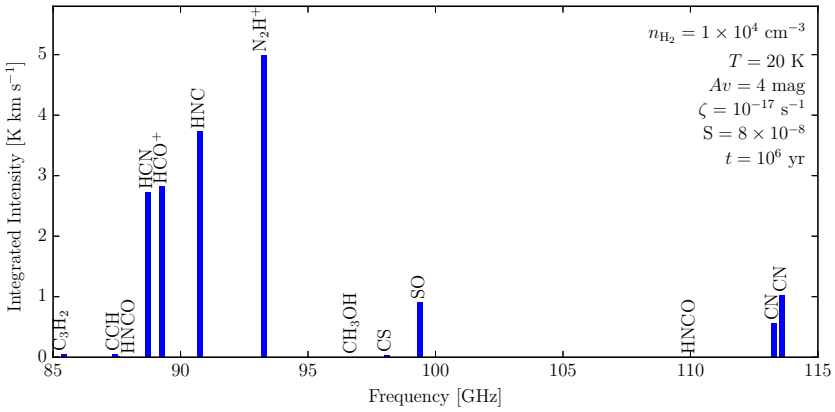

Figure 5.7 The intensity pattern when the time is set to be $t = 10^6$ yr. Obviously, the N_2H^+ intensity is high.

be formed in molecular clouds (e.g., Herbst & Leung, 1989). Figure 5.7 shows the spectral intensity pattern for the case of $n_{H_2} = 1 \times 10^4$ cm^{-3}, $T = 20$ K, $A_v = 4$ mag, $\zeta = 10^{-17}$ s^{-1}, $S_{elem} = 8 \times 10^{-8}$, $t = 10^6$ yr. Indeed, the intensity of N_2H^+ is considerably high, and that of SO is also relatively high.

Figure 5.8 shows the color diagram of all 216 parameter combinations. Above all, we can say that the good correlations are found in the upper left box with the parameters: $\zeta = 10^{-17}$ s^{-1}, $S_{elem} = 8 \times 10^{-8}$, and $t = 10^5$ yr. Even if we employ logarithms of integrated intensities for calculation of correlation coefficients, the trends are conserved as shown in Figure 5.9. In comparison of the intensities in the logarithmic scale, the bright HCO^+ emission is less wighted. Hence, the correlation looks good, even if the HCO^+ emission is too bright. This causes the "good" correlation for $A_v = 2$ mag and $S_{elem} = 8 \times 10^{-8}$, even though the HCO^+ emission is too intense. Hence, we prefer to use the correlation diagram prepare in the linear scale.

For this comparison, we employed the spectrum observed toward M51 P1. Since the spectral pattern in the 3 mm band is not significantly different among galaxies with a similar metallicity, the above result will not be changed for galaxies other than M51. Although the chemical models employed in this study contain assumptions (i.e., constant density, constant visual extinction, and constant temperature) for simplicity, they can reproduce the basic trend of the spectral intensity pattern. Remaining discrepancies are due to imperfection of the chemical models and due to the source-to-source variation of chemical compositions which reflects physical conditions of individual sources.

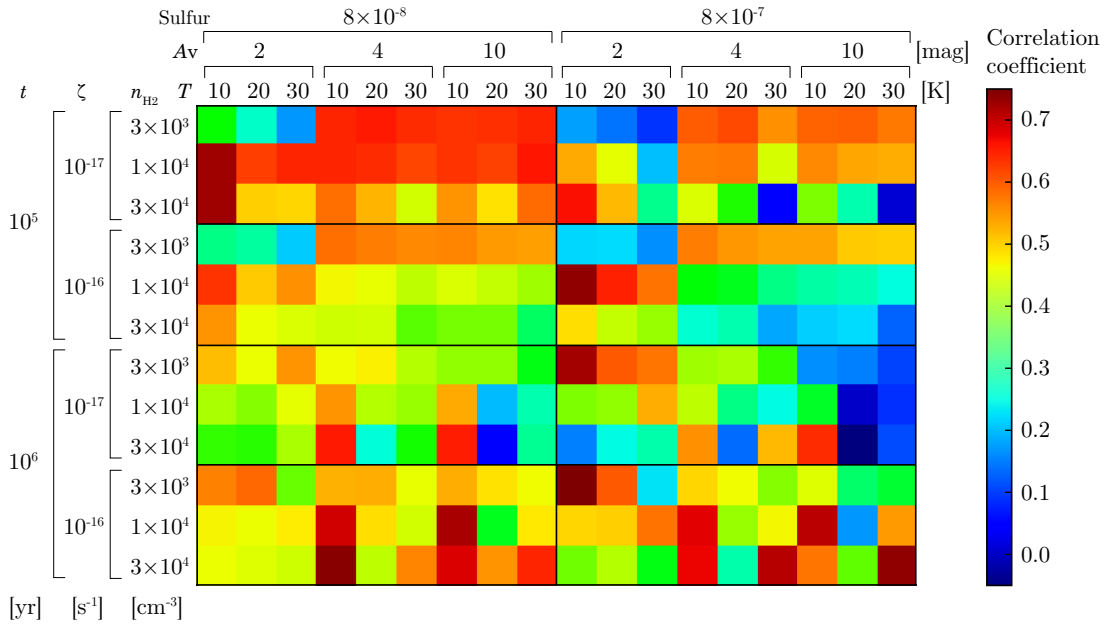

Figure 5.8 The color diagram of all 216 parameter combinations.

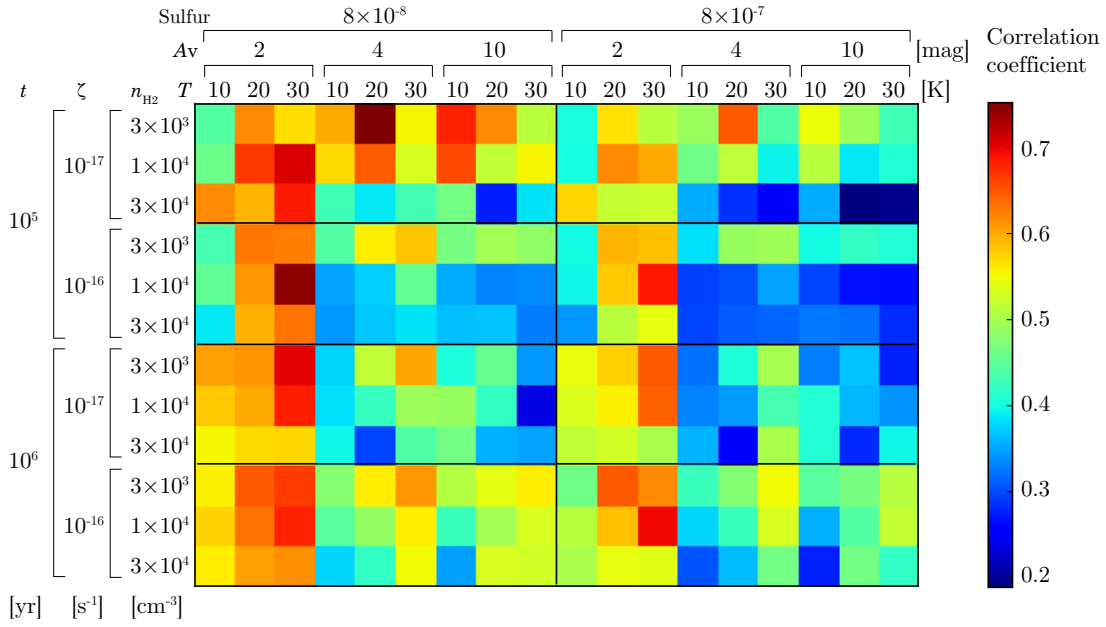

Figure 5.9 Similar to Figure 5.8, but for correlation coefficients of logarithms of integrated intensities.

5.3 Summary: Implication of Model Calculation

According to the above comparison of the chemical models and the observational result for M51 P1, we found the following results.

1: The best fit spectrum is obtained for the parameters of $n_{H_2} = 3 \times 10^3$ or 1×10^4 cm^{-2}, $T_{gas} = T_{dust} = 10$ or 20 K, $A_v = 4$ or 10 mag, $\zeta = 10^{-17}$ s^{-1}, $S_{elem} = 8 \times 10^{-8}$, and $t = 10^5$ yr.

2: The inferred evolutionary time of 10^5 yr means that molecular clouds in galaxies are chemically young on average. This is comparable to the free fall time of the cloud (3×10^5 yr for 10^4 cm^{-3}), and is shorter than the typical lifetime of molecular clouds ($10^6 - 10^7$ yr) inferred from association of evolved young stellar objects. Considering that the best visual extinction of 4 mag, some refreshment processes, such as turbulent mixing and clumpy internal structure, are needed for chemical refreshment (i.e., photodissociation of molecules), as shown in Figure 5.10. This could be possible on the basis of the following consideration. When we assume the effective sound speed (including the effect of the magnetic field) is 1 km/s, the sound crossing time for 1 pc cloud is 10^6 yr for the refreshment, when the gas is exposed to the interstellar UV radiation. However, this time can be shorter, if the cloud is clumpy or filamentary, as suggested by various observation (e.g., André et al., 2010). Considering such internal structures, the chemical youth of the cloud can be realized. Such chemical youth of molecular clouds is suggested from the relatively high C/CO ratio (e.g., Ikeda et al., 2002).

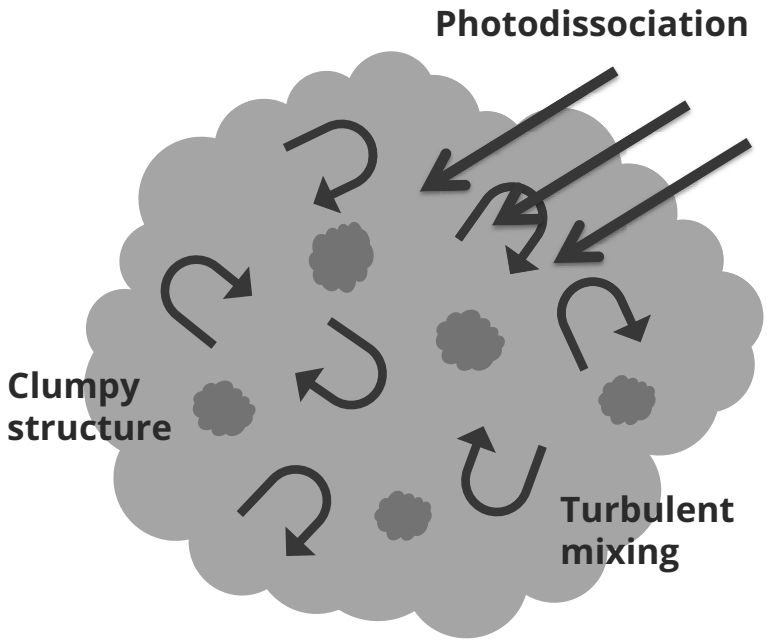

Figure 5.10 Schematic illustration of chemical refreshment of molecular clouds. By turbulent motion, clumps are exposed to the interstellar UV radiation every 10^5 yr, and then molecules are once destroyed by photodissociation. After this reset of the molecular composition, a new chemical evolution stars after shielding of the UV radiation.

Chapter 6

Conclusion

6.1 Summary of This Thesis

During the last decade, chemical diagnostics has been applied to nearby active galaxies, and chemical trends of each galaxy type have been discussed. On the other hand, such chemical trends of dwarf galaxies are left unrevealed. Because dwarf galaxies generally have lower metallicity than our Galaxy or other spiral galaxies, they can be regarded as a proxy of high-redshift galaxies, which also have lower metallicity. Metallicity will give a substantial impact on the abundance of dust grains, interstellar radiation field, and chemical composition of molecular clouds. To investigate the the effect of low metallicity on chemical composition of molecular clouds, we conducted chemical diagnostics of nearby dwarf galaxies in this thesis. We set the following questions to be addressed:

1. What is the characteristic chemical composition of molecular clouds in the metal-poor condition?
2. How does it differ from that in the metal-rich condition?
3. What physical and chemical processes are responsible for it?

With extensive observations with the world state-of-the-art radio telescopes, we successfully established the characteristic molecular composition in the low-metallicity condition for the first time, and revealed a new potential of chemical diagnostics for studies of the early universe.

6.1.1 Characteristic Chemical Composition of Low-metallicity Environments

To address the above questions, we conducted sensitive spectral-line survey observations in the 3 mm band toward the three nearby dwarf galaxies, the LMC, IC10, and NGC6822 with the Mopra 22 m telescope, the Nobeyama 45 m telescope, and the IRAM 30 m telescope, respectively. These galaxies have lower metallicity than our Galaxy by a factor of $1/3 - 1/2$, and exhibit lower N/O ratios by a

factor of $2-7$. This means that the nitrogen abundance is characteristically low among the second-raw element (C, N, and O). Based on the unbiased spectral-line survey observations, we found that the observed spectral intensity patterns are very similar among the three low-metallicity dwarf galaxies.

For the LMC, we observed seven molecular clouds, which have different star-formation activities; two are quiescent clouds without high-mass star formation, three are those associated with high-mass star formation, and two are active star-forming regions with the extended H II regions. Spectral lines of fundamental species such as CCH, HCN, HCO^+, HNC, CS, and SO were detected in all the sources as well as those of CO and ^{13}CO, while CH_3OH was not detected in any sources. The seven clouds are found to be all similar to one another in the spectral intensity pattern regardless of different star formation activities.

Following the observation toward the LMC, we extended the work to IC10 and NGC6822. As a result, we detected the lines of CCH, HCN, HCO^+, HNC, CS, SO, ^{13}CO, and CO for IC10, and CCH, HCN, HCO^+, CS, ^{13}CO, and CO for NGC6822. Although the lines are generally faint (and therefore the HNC and SO lines are not detected in NGC6822), the spectral intensity pattern of IC10 and NGC6822 is found to be strikingly similar to those observed the seven clouds in the LMC. It is noteworthy that CH_3OH was not detected both in IC10 and NGC6822, as in the case with the LMC. Hence, we have established the "general" spectral intensity pattern in low-metallicity dwarf galaxies.

To characterize the composition of molecular clouds in low-metallicity dwarf galaxies, we compared the spectra of the LMC, IC10 and NGC6822 with those of spiral galaxies with Solar metallicity (our Galaxy and M51). The characteristic chemical features of low-metallicity dwarf galaxies are summarized as follows:

Direct Impact of the Low Metallicity: Deficient Nitrogen-Bearing Molecules

We find the deficiency of nitrogen-bearing species in the low-metallicity dwarf galaxies. The HCN/HCO^+ and HNC/HCO^+ abundance ratios are indeed lower than those in M51 and our Galaxy. Other nitrogen-bearing species, HNCO and N_2H^+, are not detected in the low-metallicity galaxies, while they are detected in M51. The deficiency of the nitrogen-bearing species most likely reflects the lower N/O ratio by a factor of $2-7$ in the low-metallicity dwarf galaxies. The HCN/HCO^+ ratio is known to be enhanced in/around AGNs, which is interpreted as the effect of XDRs, cosmic-rays, and/or shock heatings. In this study, we observed molecular clouds without such an effect, and moreover, the HCN/HCO^+ ratio is lower than that of the Galactic translucent clouds. Hence, the low HCN/HCO^+ ratio represents the intrinsic effect of the elemental abundance.

Effect of the Intense UV Radiation Field: Abundant CCH and Deficient CH_3OH

CCH is enhanced in the low-metallicity dwarf galaxies. In contrast to the nitrogen-bearing molecules, this feature cannot be interpreted as the elemental abundance effect. Since the C/O ratio is even lower in the three observed galaxies, the enhancement of the CCH/HCO^+ ratio is striking. In low-metallicity galaxies, the abundance of dust grains is lower than that in the Solar neighborhood, and hence, the visual extinction for a given H_2 column density is lower. This effect extends PDRs in clouds peripheries. Since CCH is known to be produced efficiently in PDRs, the high CCH abundance revealed in these dwarf galaxies likely reflects the low-metallicity condition. Moreover, non-detection of CH_3OH can also be explained in this picture. CH_3OH is mainly produced on dust grains by hydrogenation of CO. Extension of PDRs in cloud peripheries would raise the temperature there, which decreases CH_3OH formation due to a fall of sticking probability of hydrogen atoms. Hence, CH_3OH would be less abundant in the low-metallicity condition.

Above all, characteristic molecular composition of the low-metallicity dwarf galaxies is revealed. Deficiency of nitrogen-bearing molecules indicates importance of the elemental abundances in interpretation of chemical compositions in external galaxies. The results for CCH and CH_3OH represent a crucial role of the UV radiation in low-metallicity galaxies. These results constitute a fundamental base of the chemical compositions of low-metallicity dwarf galaxies, which will be useful to understand molecular composition of other galaxies, especially those in the early universe.

6.1.2 Molecular-Cloud-Scale Chemical Composition of W3(OH)

In addition to the above work, we also investigated the molecular-cloud-scale chemical composition toward the Galactic molecular cloud for comparison with external galaxies. With the NRO 45 m telescope, we conducted a mapping spectral line survey toward W3(OH), which is one of the most active star forming regions in the Perseus arm. We observed the area of $16' \times 16'$, which corresponds to 9.0 pc $\times$ 9.0 pc. We prepared the spectrum averaged over the observed area, and identified 8 molecular species CCH, HCN, HCO^+, HNC, CS, SO, $C^{18}O$, and ^{13}CO. On the other hand, the spectrum of the W3(OH) hot core observed at a 0.17 pc resolution shows the lines of various molecules such as OCS, H_2CS CH_3CCH, and CH_3CN, in addition to the above species. In the spatially averaged spectrum, emission of the species concentrated just around the star-forming core such as CH_3OH and HC_3N is fainter than in the hot core spectrum, whereas emission of the species widely extended over the cloud such as CCH is relatively brighter. We classified the observed area into 5 sub-regions according to the integrated intensity of ^{13}CO, and evaluated the contribution to the averaged spectrum from each sub-region. The CCH, HCN, HCO^+, and CS lines can be seen even in the spectrum of the sub-region

with the lowest ^{13}CO integrated intensity range (< 10 K km s^{-1}). The contributions of the extended area is confirmed to be dominant in the spatially averaged spectrum.

6.1.3 Physical Parameters of an "Averaged" Molecular Cloud

To understand the meaning of the molecular-cloud-scale chemical compositions in more detail, we conducted chemical model calculations. The model calculations were carried out for a fairly extensive range of H_2 density (n_{H_2}), gas temperature (T_{gas}), dust temperature (T_{dust}), visual extinction (A_v), cosmic-ray ionization rate (ζ), abundance of sulfur atoms (S_{elem}), and time (t). We compared the result of the model calculations with the observational data toward the nearby spiral galaxy M51, where we focused on the integrated intensity pattern in the 3 mm band including 14 molecular lines of C_3H_2, CCH, HNCO, HCN, HCO^+, HNC, N_2H^+, CH_3OH, CS, SO, and CN. The observed spectrum is reproduced most reasonably by the parameters of $n_{H_2} < 1 \times 10^4$ cm^{-2}, $T_{gas} = T_{dust} = 10$ or 20 K, $A_v > 4$ mag, $\zeta = 10^{-17}$ s^{-1}, $S_{elem} = 8 \times 10^{-8}$, and $t = 10^5$ yr. The relatively early evolutionary time of 10^5 yr and the relatively low visual extinction of 4 mag suggest that molecular clouds in galaxies are chemically young on average due to some refreshment processes, such as turbulent mixing and clumpy internal structure.

6.2 Future Prospects

As described above, we successfully established the characteristic molecular composition of low-metallicity dwarf galaxies. These results of low-metallicity dwarf galaxies will be useful to study chemical compositions of first star-forming systems in the early universe, as well as those of nearby active galaxies. Hence, the next step that we should take is to conduct detailed chemical studies of high-redshift galaxies, which provide us a deep insight into young galaxies. The molecular emissions of high-redshift galaxies are generally faint and therefore have been difficult to be observed. Because of this reason, observations of high-redshift galaxies have mostly been limited to the CO lines, the brightest molecular lines apart from the fine structure lines of atoms and ions. However, it is worth attempting to conduct chemical studies toward high-redshift galaxies by taking advantage of high sensitivity of Atacama Large Millimeter and submillimeter Array (ALMA; Figure 6.1), in order to shed light on their peculiar physical conditions from the view point of chemistry. The knowledge on dwarf galaxies will be an important base to understand chemical compositions of high-redshift galaxies.

Figure 6.1 The Atacama Large Millimeter and submillimeter Array. (ALMA NAOJ online, accessed December 2016)

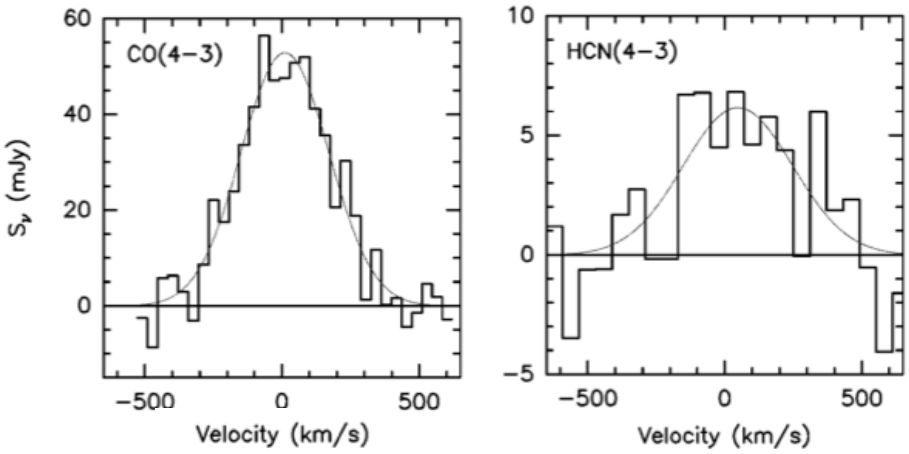

Figure 6.2 The CO ($J = 4 - 3$) and HCN ($J = 4 - 3$) lines in the Cloverleaf observed by Barvainis et al. (1997).

6.2.1 Chemical Diagnostics toward High-Redshift Galaxies

As the initial step to study molecular composition of high-redshift galaxies, an unbiased spectral line survey should be conducted to understand the molecular composition without any preconception. For the spectral line survey, galaxies hosting quasar such as the Cloverleaf ($z = 2.56$) and APM08279+5255 ($z = 3.91$) is considered to be the best target. Both the Cloverleaf and APM08279+5255 have been known to have exceptionally bright CO intensity, partly because of the amplification by gravitational lensing. In addition, they are among a few galaxies in which the HCO^+ and HCN lines are detected (Figure 6.2). This spectral line survey, if realized, will provide us with chemical characteristics of distant galaxies, and will open a new avenue to chemical diagnostics of distant galaxies.

6.2.2 Building a Bridge between Nucleosynthesis History and Molecular Composition

Currently, the elemental abundances in external galaxies are mainly studied by using optical lines. On the other hand, we have demonstrated in this study that the molecular composition well reflects the elemental abundances. This can be used to trace the nucleosynthesis history of the nuclear regions deeply embedded in dusty molecular gas. The results will help us to understand chemical evolution of galaxies.

To investigate the nucleosynthesis history, that is, the star formation history of the galaxy, nitrogen-bearing molecular species are of special importance. In the Local Universe, the abundance of "secondary" nuclei such as N and ^{13}C are used as diagnostics of the nucleosynthesis evolution and pristine gas inflows and outflows. While primary nuclei such as ^{12}C and O are quickly produced by He burning in shorter-lived massive stars, N and ^{13}C are mainly synthesized in longer-lived low- or intermediate-mass stars. In the studies on low-metallicity galaxies, the effect of the low elemental abundance of nitrogen is clearly seen as the low abundances of N-bearing molecules (HCN, HNC, and N_2H^+). Hence, the abundance of nitrogen-bearing molecules should be particularly focused on to trace nucleosynthesis history of high-redshift galaxies.

For example, the Cloverleaf is again a good target. It is located at $z = 2.56$, which corresponds to the age of the universe of 2.5 Gyr. Although it seems too young to harbor large amounts of synthesized nuclei, in particular secondary nuclei, detections of the CO, HCO^+ and HCN lines suggest rapid metal enrichment due to starbursts. Further observations of other molecular species are necessary to investigate the nature of the molecular composition and the nucleosynthesis history in the Cloverleaf. In actual studies, not only the elemental abundances but also the physical condition such as temperature, density, and the existence of galactic-scale shocks would also affect the molecular abundances. Multi-line analyses of multiple molecular species are thus needed to disentangle these possibilities. The results will eventually allow us to establish chemical characteristics in this galaxy and their relation to the nucleosynthesis history.

Bibliography

Aguirre, J. E., Bezaire, J. J., Cheng, E. S., et al. 2003, *The Astrophysical Journal*, 596, 273

Aikawa, Y., Furuya, K., Nomura, H., & Qi, C. 2015, *The Astrophysical Journal*, 807, 120

Aikawa, Y., Wakelam, V., Garrod, R. T., & Herbst, E. 2008, *The Astrophysical Journal*, 674, 993

Aladro, R., Martín, S., Martín-Pintado, J., et al. 2011, *Astronomy & Astrophysics*, 535, A84

Aladro, R., Viti, S., Bayet, E., et al. 2013, *Astronomy & Astrophysics*, 549, A39

Aladro, R., Martín, S., Riquelme, D., et al. 2015, *Astronomy & Astrophysics*, 579, A101

ALMA NAOJ online. accessed December 2016, Atacama Large Millimeter/submillimeter Array, http://alma.mtk.nao.ac.jp/j/multimedia/picture/antenna/1202236546.html, ,

André, P., Men'shchikov, A., Bontemps, S., et al. 2010, *Astronomy & Astrophysics*, 518, L102

Bachiller, R., Martin-Pintado, J., Tafalla, M., Cernicharo, J., & Lazareff, B. 1990, *Astronomy & Astrophysics*, 231, 174

Bachiller, R., & Pérez Gutiérrez, M. 1997, *The Astrophysical Journal Letters*, 487, L93

Barbá, R. H., Rubio, M., Roth, M. R., & García, J. 2003, *The Astronomical Journal*, 125, 1940

Barvainis, R., Maloney, P., Antonucci, R., & Alloin, D. 1997, The Astrophysical Journal, 484, 695

Becker, R., & Freudling, W. 1991, *Astronomy & Astrophysics*, 251, 454

Bica, E., Claria, J., & Dottori, H. 1992, *The Astronomical Journal*, 103, 1859

Bizzocchi, L., Caselli, P., Spezzano, S., & Leonardo, E. 2014, *Astronomy & Astrophysics*, 569, A27

Bolatto, A. D., Jackson, J. M., Wilson, C. D., & Moriarty-Schieven, G. 2000, *The Astrophysical Journal*, 532, 909

Bresolin, F., Garnett, D. R., & Kennicutt, Jr., R. C. 2004, *The Astrophysical Journal*, 615, 228

Caselli, P., & Ceccarelli, C. 2012, *The Astronomy & Astrophysics Review*, 20, 56

Caselli, P., van der Tak, F. F. S., Ceccarelli, C., & Bacmann, A. 2003, *Astronomy & Astrophysics*, 403, L37

Caselli, P., Walmsley, C. M., Tafalla, M., Dore, L., & Myers, P. C. 1999, *The Astrophysical Journal Letters*, 523, L165

Caselli, P., Walmsley, C. M., Zucconi, A., et al. 2002, *The Astrophysical Journal*, 565, 344

Cazaux, S., Tielens, A., Ceccarelli, C., et al. 2003, *The Astrophysical Journal Letters*, 593, L51

Chin, Y.-N., Henkel, C., Whiteoak, J. B., et al. 1997, *Astronomy & Astrophysics*, 317, 548

Dettmar, R.-J., & Heithausen, A. 1989, *The Astrophysical Journal Letters*, 344, L61

Dufour, R., Shields, G., & Talbot Jr, R. 1982, *The Astrophysical Journal*, 252, 461

Dumouchel, F., Faure, A., & Lique, F. 2010, *Monthly Notices of the Royal Astronomical Society*, 406, 2488

Ellingsen, S. P., Breen, S. L., Caswell, J. L., Quinn, L. J., & Fuller, G. A. 2010, *Monthly Notices of the Royal Astronomical Society*, 404, 779

Elmegreen, B. G., Rubio, M., Hunter, D. A., et al. 2013, *Nature*, 495, 487

Engelbracht, C. W., Gordon, K. D., Bendo, G. J., et al. 2004, *The Astrophysical Journal Supplement Series*, 154, 248

Esteban, C., García-Rojas, J., Carigi, L., et al. 2014, *Monthly Notices of the Royal Astronomical Society*, 443, 624

Flower, D. 1999, *Monthly Notices of the Royal Astronomical Society*, 305, 651

Fuente, A., García-Burillo, S., Gerin, M., et al. 2005, *The Astrophysical Journal Letters*, 619, L155

Fuente, A., Martin-Pintado, J., Cernicharo, J., & Bachiller, R. 1993, *Astronomy & Astrophysics*, 276, 473

Fukui, Y., & Kawamura, A. 2010, *Annu. Rev. Astron. Astrophys.*, 48, 547

Garnett, D. R. 1990, *The Astrophysical Journal*, 363, 142

Garnett, D. R., Edmunds, M. G., Henry, R. B. C., Pagel, B. E. J., & Skillman, E. D. 2004, *The Astronomical Journal*, 128, 2772

Gieren, W., Pietrzyński, G., Szewczyk, O., et al. 2008, *The Astrophysical Journal*, 683, 611

Gil de Paz, A., Madore, B. F., & Pevunova, O. 2003, *The Astrophysical Journal Supplement Series*, 147, 29

Ginard, D., Fuente, A., García-Burillo, S., et al. 2015, *Astronomy & Astrophysics*, 578, A49

Graedel, T., Langer, W., & Frerking, M. 1982, *The Astrophysical Journal Supplement Series*, 48, 321

Gratier, P., Braine, J., Rodriguez-Fernandez, N., et al. 2010, *Astronomy & Astrophysics*, 512, A68

Green, S., & Chapman, S. 1978, *The Astrophysical Journal Supplement Series*, 37, 169

Gruendl, R. A., & Chu, Y.-H. 2009, *The Astrophysical Journal Supplement Series*, 184, 172

Habing, H. J. 1968, *Bulletin of the Astronomical Institutes of the Netherlands*, 19, 421

Harada, N., Nishimura, Y., Watanabe, Y., et al. 2016, in prep.

Hartoog, O. E., Sana, H., de Koter, A., & Kaper, L. 2012, *Monthly Notices of the Royal Astronomical Society*, 422, 367

Heikkilä, A., Johansson, L., & Olofsson, H. 1999, *Astronomy & Astrophysics*, 344, 817

Henize, K. G. 1956, *The Astrophysical Journal Supplement Series*, 2, 315

Herbst, E., & Leung, C. M. 1989, *The Astrophysical Journal Supplement Series*, 69, 271

Herbst, E., & Van Dishoeck, E. F. 2009, *Annu. Rev. Astro. Astrophys.*, 47, 427

Hirota, T., Ikeda, M., & Yamamoto, S. 2001, *The Astrophysical Journal*, 547, 814

Hirota, T., Yamamoto, S., Mikami, H., & Ohishi, M. 1998, *The Astrophysical Journal*, 503, 717

Hodge, P., Lee, M. G., & Kennicutt, Jr., R. C. 1988, *Publications of the Astronomical Society of the Pacific*, 100, 917

Hodge, P. W. 1963, *The Astronomical Journal*, 68, 691

Homma, D., Chiba, M., Okamoto, S., et al. 2016, *The Astrophysical Journal*, 832, 21

Hunter, D. A. 2001, *The Astrophysical Journal*, 559, 225

Ikeda, M., Oka, T., Tatematsu, K., Sekimoto, Y., & Yamamoto, S. 2002, *The Astrophysical Journal Supplement Series*, 139, 467

IRAM online. accessed December 2016, Institut de Radioastronomie Millimétrique, http://www.iram-institute.org, ,

Israel, F. P., Baas, F., Rudy, R. J., Skillman, E. D., & Woodward, C. E. 2003a, *Astronomy & Astrophysics*, 397, 87

Israel, F. P., Tacconi, L. J., & Baas, F. 1995, *Astronomy & Astrophysics*, 295, 599

Israel, F. P., de Graauw, T., Johansson, L. E. B., et al. 2003b, *Astronomy & Astrophysics*, 401, 99

Israel, F. P., Johansson, L. E. B., Rubio, M., et al. 2003c, *Astronomy & Astrophysics*, 406, 817

Jackson, D. C., Cannon, J. M., Skillman, E. D., et al. 2006, *The Astrophysical Journal*, 646, 192

Johansson, L. E. B., Olofsson, H., Hjalmarson, A., Gredel, R., & Black, J. H. 1994, *Astronomy & Astrophysics*, 291, 89

Kato, D., Ita, Y., Onaka, T., et al. 2012, *The Astronomical Journal*, 144, 179

Kim, S.-J., Kim, H.-D., Lee, Y., et al. 2006, *The Astrophysical Journal Supplement Series*, 162, 161

Kohno, K., Matsushita, S., Vila-Vilaró, B., et al. 2001, in Astronomical Society of the Pacific Conference Series, Vol. 249, The Central Kiloparsec of Starbursts and AGN: The La Palma Connection, ed. J. H. Knapen, J. E. Beckman, I. Shlosman, & T. J. Mahoney, 672

Lada, C. J., Elmegreen, B. G., Cong, H.-I., & Thaddeus, P. 1978, *The Astrophysical Journal Letters*, 226, L39

Lebouteiller, V., Sloan, G., Groenewegen, M., et al. 2012, *Astronomy & Astrophysics*, 546, A94

Lebouteiller, V., Cormier, D., Madden, S. C., et al. 2012, *Astronomy & Astrophysics*, 548, A91

Lee, H., Skillman, E. D., & Venn, K. A. 2006, *The Astrophysical Journal*, 642, 813

Lehner, N., Wakker, B., & Savage, B. 2004, *The Astrophysical Journal*, 615, 767

Lepp, S., & Dalgarno, A. 1996, *Astronomy & Astrophysics*, 306, L21

Lequeux, J., Peimbert, M., Rayo, J., Serrano, A., & Torres-Peimbert, S. 1979, *Astronomy & Astrophysics*, 80, 155

Leroy, A., Bolatto, A., Walter, F., & Blitz, L. 2006, *The Astrophysical Journal*, 643, 825

Leung, C. M., Herbst, E., & Huebner, W. 1984, *The Astrophysical Journal Supplement Series*, 56, 231

Lique, F., Spielfiedel, A., & Cernicharo, J. 2006, *Astronomy & Astrophysics*, 451, 1125

Liszt, H., & Lucas, R. 2001, *Astronomy & Astrophysics*, 370, 576

Lucas, R., & Liszt, H. 2000, *Astronomy & Astrophysics*, 358, 1069

Lucke, P., & Hodge, P. 1970, *The Astronomical Journal*, 75, 171

Madden, S., Poglitsch, A., Geis, N., Stacey, G., & Townes, C. 1997, *The Astrophysical Journal*, 483, 200

Magrini, L., & Gonçalves, D. R. 2009, *Monthly Notices of the Royal Astronomical Society*, 398, 280

Marleau, F. R., Noriega-Crespo, A., & Misselt, K. A. 2010, *The Astrophysical Journal*, 713, 992

Martín, S., Mauersberger, R., Martín-Pintado, J., Henkel, C., & García-Burillo, S. 2006, *The Astrophysical Journal Supplement Series*, 164, 450

Martín, S., Mauersberger, R., Martín-Pintado, J., Henkel, C., & García-Burillo, S. 2006, *The Astrophysical Journal Supplement Series*, 164, 450

Martín, S., Verdes-Montenegro, L., Aladro, R., et al. 2014, *Astronomy & Astrophysics*, 563, L6

Martín, S., Krips, M., Martín-Pintado, J., et al. 2011, *Astronomy & Astrophysics*, 527, A36

Massey, P., & Holmes, S. 2002, *The Astrophysical Journal Letters*, 580, L35

Mateo, M. L. 1998, *Annu. Rev. Astro. Astrophys.*, 36, 435

McCall, B. J., Hinkle, K. H., Geballe, T. R., et al. 2002, *The Astrophysical Journal*, 567, 391

McConnachie, A. W., Irwin, M. J., Ferguson, A. M. N., et al. 2005, *Monthly Notices of the Royal Astronomical Society*, 356, 979

Meijerink, R., Spaans, M., & Israel, F. P. 2007, *Astronomy & Astrophysics*, 461, 793

Meixner, M., Gordon, K. D., Indebetouw, R., et al. 2006, The Astronomical Journal, 132, 2268

Mikami, H., Umemoto, T., Yamamoto, S., & Saito, S. 1992, *The Astrophysical Journal Letters*, 392, L87

Millar, T. J., & Herbst, E. 1990, *Monthly Notices of the Royal Astronomical Society*, 242, 92

Mizuno, Y., Kawamura, A., Onishi, T., et al. 2010, *Publications of the Astronomical Society of Japan*, 62, 51

Mopra Telescope online. accessed December 2016, The Mopra Telescope, http://www.narrabri.atnf.csiro.au/mopra/, ,

Morton, D. 1974, *The Astrophysical Journal*, 193, L35

Müller, H. S., Schlöder, F., Stutzki, J., & Winnewisser, G. 2005, Journal of Molecular Structure, 742, 215

Müller, H. S. P., Thorwirth, S., Roth, D. A., & Winnewisser, G. 2001, *Astronomy & Astrophysics*, 370, L49

Muller, S., Beelen, A., Guélin, M., et al. 2011, *Astronomy & Astrophysics*, 535, A103

Nishimura, Y., Watanabe, Y., Sakai, N., & Yamamoto, S. 2016, in prep.

NRO NAOJ online. accessed December 2016, National Astronomical Observatory of Japan NOBEYAMA, http://www.nro.nao.ac.jp/gallery/45m.html, ,

Onodera, S., Kuno, N., Tosaki, T., et al. 2012, *Publications of the Astronomical Society of Japan*, 64, 133

Ott, J., Henkel, C., Staveley-Smith, L., & Weiß, A. 2010, *The Astrophysical Journal*, 710, 105

Parise, B., Castets, A., Herbst, E., et al. 2004, *Astronomy & Astrophysics*, 416, 159

Paron, S., Ortega, M., Cunningham, M., et al. 2014, *Astronomy & Astrophysics*, 572, A56

Petitpas, G. R., & Wilson, C. D. 1998, *The Astrophysical Journal*, 496, 226

Pety, J., Teyssier, D., Fossé, D., et al. 2005, *Astronomy & Astrophysics*, 435, 885

Pietrzyński, G., Graczyk, D., Gieren, W., et al. 2013, *Nature*, 495, 76

Rabli, D., & Flower, D. 2010, *Monthly Notices of the Royal Astronomical Society*, 406, 95

Richer, M. G., & McCall, M. L. 1995, *The Astrophysical Journal*, 445, 642

Rivera-Ingraham, A., Martin, P. G., Polychroni, D., et al. 2013, *The Astrophysical Journal*, 766, 85

Ruffle, D. P., & Herbst, E. 2000, *Monthly Notices of the Royal Astronomical Society*, 319, 837

Sakai, N., & Yamamoto, S. 2013, *Chemical reviews*, 113, 8981

Sakai, T., Oka, T., & Yamamoto, S. 2006, *The Astrophysical Journal*, 649, 268

Sakon, I., Onaka, T., Kaneda, H., et al. 2006, *The Astrophysical Journal*, 651, 174

Seale, J. P., Looney, L. W., Chu, Y.-H., et al. 2009, *The Astrophysical Journal*, 699, 150

Shi, Y., Wang, J., Zhang, Z.-Y., et al. 2015, *The Astrophysical Journal Letters*, 804, L11

Shimonishi, T., Dartois, E., Onaka, T., & Boulanger, F. 2016, *Astronomy & Astrophysics*, 585, A107

Shimonishi, T., Nishimura, Y., Watanabe, Y., et al. 2016, in prep.

Shimonishi, T., Onaka, T., Kato, D., et al. 2010, *Astronomy & Astrophysics*, 514, 12

—. 2013, *The Astronomical Journal*, 145, 32

Spielfiedel, A., Feautrier, N., Najar, F., et al. 2012, *Monthly Notices of the Royal Astronomical Society*, 421, 1891

Suzuki, H., Yamamoto, S., Ohishi, M., et al. 1992, *The Astrophysical Journal*, 392, 551

Takakuwa, S., Kamazaki, T., Saito, M., & Hirano, N. 2003, *The Astrophysical Journal*, 584, 818

Turner, B. 1994, *The Astrophysical Journal*, 420, 661

—. 1995a, *The Astrophysical Journal*, 455, 556

—. 1995b, *The Astrophysical Journal*, 449, 635

—. 1996, *The Astrophysical Journal*, 461, 246

—. 1998, *The Astrophysical Journal*, 501, 731

Turner, B., Herbst, E., & Terzieva, R. 2000, *The Astrophysical Journal Supplement Series*, 126, 427

Turner, B., Pirogov, L., & Minh, Y. 1997, *The Astrophysical Journal*, 483, 235

Turner, B., Terzieva, R., & Herbst, E. 1999, *The Astrophysical Journal*, 518, 699

van den Bergh, S., Cohen, J. G., Hogg, D. W., & Blandford, R. 2000, *The Astronomical Journal*, 120, 2190

van der Marel, R. P., & Cioni, M.-R. L. 2001, *The Astronomical Journal*, 122, 1807

van der Tak, F., Black, J. H., Schöier, F., Jansen, D., & van Dishoeck, E. F. 2007, *Astronomy & Astrophysics*, 468, 627

van Dishoeck, E. F., & Black, J. H. 1988, *The Astrophysical Journal*, 334, 771

Van Steenberg, M. E., & Shull, J. M. 1988, *The Astrophysical Journal*, 330, 942

Vincenzo, F., Belfiore, F., Maiolino, R., Matteucci, F., & Ventura, P. 2016, *Monthly Notices of the Royal Astronomical Society*, 458, 3466

Wakelam, V., Ceccarelli, C., Castets, A., et al. 2005, *Astronomy & Astrophysics*, 437, 149

Wakelam, V., Hersant, F., & Herpin, F. 2011, *Astronomy & Astrophysics*, 529, 112

Wallström, S. H. J., Muller, S., & Guélin, M. 2016, *Astronomy & Astrophysics*, 595, A96

Wang, M., Chin, Y.-N., Henkel, C., Whiteoak, J. B., & Cunningham, M. 2009, *The Astrophysical Journal*, 690, 580

Watanabe, N., & Kouchi, A. 2002, *The Astrophysical Journal Letters*, 571, L173

Watanabe, N., Shiraki, T., & Kouchi, A. 2003, *The Astrophysical Journal Letters*, 588, L121

Watanabe, Y., Nishimura, Y., Harada, N., & Yamamoto, S. 2016, submitted for publication in *The Astrophysical Journal*

Watanabe, Y., Sakai, N., Sorai, K., & Yamamoto, S. 2014, *The Astrophysical Journal*, 788, 4

Watanabe, Y., Sakai, N., López-Sepulcre, A., et al. 2015, *The Astrophysical Journal*, 809, 162

Westerlund, B. E. 1997, The Magellanic Clouds No. 29 (*Cambridge University Press*)

Whitney, B. A., Sewilo, M., Indebetouw, R., et al. 2008, *The Astronomical Journal*, 136, 18

Wiklind, T., & Combes, F. 1996, *Nature*, 379, 139

Wong, T., Hughes, A., Ott, J., et al. 2011, *The Astrophysical Journal Supplement Series*, 197, 16

Wynn-Williams, C. G., Becklin, E. E., & Neugebauer, G. 1972, *Monthly Notices of the Royal Astronomical Society*, 160, 1

Xu, Y., Reid, M., Zheng, X., & Menten, K. 2006, *Science*, 311, 54

Yang, B., Stancil, P., Balakrishnan, N., & Forrey, R. 2010, *The Astrophysical Journal*, 718, 1062

Young, L. M. 2001, *The Astronomical Journal*, 122, 1747

Young, L. M., & Lo, K. Y. 1997, *The Astrophysical Journal*, 476, 127

Acknowledgements

Special thanks are due to my thesis supervisor Professor Satoshi Yamamoto for his invaluable support during my PhD course. I would like to thank Dr. Takashi Shimonishi, Prof. Yuri Aikawa, Dr. Akiko Kawamura, and Dr. Nanase Harada for fruitful discussion on whole of this study, Dr. Christian Henkel, Dr. Thushara Pillai, and Dr. Jens Kauffmann for and kind support during my stay in Max-Planck-Institut für Radioastronomie, Bonn, and Prof. Toru Yamada for discussing on my future research plan.

I am grateful to the members of Yamamoto group: Dr. Yoshimasa Watanabe, Dr. Nami Sakai, Ms. Yoko Oya, Mr. Yuji Ebisawa, Mr. Kento Yoshida, Mr. Muneaki Imai, Mr. Yutaro Chiba, Mr. Osamu Oguchi, and Ms. Miki Ueda.

Finally, I would also like to express my gratitude to the member of my dissertation committee: Prof. Aya Bamba, Prof. Naoki Yoshida Prof. Takao Nakagawa Prof. Masami Ouchi and Prof. Tetsuo Hasegawa.

This study is financially supported by the Advance Leading Graduate Course for Photon Science (ALPS) and JSPS fellowship (268280).